

**Kazan Federal University  
Zavoisky Physical-Technical Institute  
Institute of Perspective Research  
Tatarstan Academy of Sciences  
Russian Foundation for Basic Research  
Russian Science Foundation  
Bruker Ltd (Moscow)**

# **ACTUAL PROBLEMS OF MAGNETIC RESONANCE AND ITS APPLICATION**

**XX International  
Youth Scientific School**



**Program  
Lecture Notes  
Proceedings**

**Kazan  
24 - 29 September 2018**

Kazan Federal University  
Zavoisky Physical-Technical Institute  
Institute of Perspective Research  
Tatarstan Academy of Sciences  
Russian Foundation for Basic Research  
Russian Science Foundation

# **ACTUAL PROBLEMS OF MAGNETIC RESONANCE AND ITS APPLICATION**

**XX International Youth Scientific School**

## **Program Lecture Notes Proceedings**

**Kazan  
24 – 29 September 2018**



**KAZAN  
2018**

UDC 537  
LBC 22.334  
A19

### Administration of the School

Professor **M.S. Tagirov** (KFU, Kazan) — rector  
Professor **V.A. Zhikharev** (KSTU, Kazan) — vice-rector  
Professor **V.K. Voronkova** (KFTI RAS, Kazan) — scientific secretary  
**A.V. Bogaychuk** (KFU, Kazan) — secretary

### Program committee

Chairman  
Professor **V.A. Atsarkin** (IREE, Moscow)

### Committee members

Professor **A.V. Aganov** (KFU, Kazan)  
Professor **I.A. Garifullin** (KFTI RAS, Kazan)  
Academician of RAS **K.M. Salikhov** (KFTI RAS, Kazan)  
Professor **V.D. Skirda** (KFU, Kazan)  
Professor **L.R. Tagirov** (KFU, Kazan)

### Organizing committee

M.S. Tagirov, V.A. Zhikharev, I.P. Volodina, I.G. Motygullin, A.V. Klochkov,  
E.M. Alakshin, I.V. Romanova, M.P. Rodionova, E.I. Kondratyeva, T.R. Safin,  
V.V. Kuzmin, S.A. Volodin, Yu. Kochneva, A.V. Egorov, A.L. Starikov

**A19** **Actual problems of magnetic resonance and its application:** program, lecture notes, proceedings of the XX International Youth Scientific School (Kazan, 24 – 29 September 2018) / edited by M.S. Tagirov, V.A. Zhikharev. – Kazan: Kazan University Press, 2018. – 124 p.

**ISBN 978-5-00130-036-6**

This collection contains the reports of young scientists submitted to the XX International Youth Scientific School “Actual problems of magnetic resonance and its application”, organized by the Kazan Federal University and the Zavoisky Physical-Technical Institute.

XX International Youth Scientific School was performed with financial support of Russian Foundation for Basic Research under the grant # 18-42-161003

The cover design was developed by D.A. Tayurskii.

**UDC 537**  
**LBC 22.334**

**ISBN 978-5-00130-036-6**

© **Kazan University Press, 2018**

# PROGRAM

## Program

### Monday, September 24

10:00 – 12:30 **Registration**

*Third physical hall (Hall of E.K. Zavoisky) - auditorium 247, main building of KFU.*

16:10 – 16:30 **Opening Ceremony of School-2018**

16:30 – 17:10 **Lecture.** Uwe Eichhoff – “The human brain: development and aging explored by MRI”

*Cafe, Institute of Physics.*

17:10 **Welcome Party**

### Tuesday, September 25

**Lectures** *Auditorium 254, main building of KFU.*

9:00 – 10:00 V. Klochkov – “Investigation of the spatial structure of different drugs, proteins & oligopeptides, and their complexes with models of cell membrane in solution by modern NMR spectroscopy”

10:00 – 11:00 B. Khairutdinov – “NMR Spectroscopy to Study the Structure, Dynamics and Molecular Interactions of Biopolymers”

11:00 – 11:30 **Coffee break**

11:30 – 12:30 K. Usachev – “NMR spectroscopy applications in structural studies of Staphylococcus aureus ribosome hibernation mediated by intermolecular interactions of HPF”

12:30 – 13:30 M. Gafurov – “Electron paramagnetic resonance of atherosclerotic plaques and synthetic calcium phosphates to follow pathological calcification processes”

**Oral Session** *Auditorium 254, main building of KFU.*

14:30 – 14:50 Yu. Berestneva - “Experimental vs GIAO calculated NMR spectra for [1,2]diazepino[4,5-b]indole derivatives”

14:50 – 15:10 M. Goldberg - “Synthesis and sintering of the synthetic hydroxyapatite doped with aluminum”

15:10 – 15:30 A. Fedotov - “Investigation of synthetic octacalciumphosphate content and structure with electron paramagnetic resonance”

15:30 – 15:50 R. Novikov – “Application of  $^{71}\text{Ga}$  and  $^{127}\text{I}$  NMR spectroscopy for the mechanistic studies of Ga(III)-mediated reactions of D–A cyclopropanes with pyrazolines”

15:50 – 16:10 K. Makushin – “Analysis and interpretation of ENDOR spectra of  $\text{LiYF}_4$  crystal activated with rare-earth ions”

16:10 – 16:30 D. Shurtakova – “Spin-lattice relaxation of  $\text{NO}_3^{2-}$  complex in synthetic hydroxyapatite. Calculation of the relaxation rate using the phonon spectrum”

## PROGRAM

16:30 – 17:00 **Coffee break**

17:00 – 17:20 E. Razina - “EPR of calixarenes doped by rare-earth metals ions”

17:20 – 17:40 D. Melnikova - “Towards an alpha-casein translational mobility by NMR”

17:40 – 18:00 D. Ivanov - “Resinous-asphaltene aggregates by NMR analysis”

18:00 – 18:20 A. Sorokina - “ESR and electrophysical properties of oil fractions”

18:20 – 18:40 A. Voitash - “ $^1\text{H}$  NMR spectroscopy investigation of thermally expanded graphite sorption capacity”

### **Wednesday, September 26**

**Lectures** *Auditorium 254, main building of KFU.*

9:00 – 10:00 F. Dzheparov – “Random walks in disordered lattice, CTRW, memory and dipole transport”

10:00 – 11:00 E. Fel'dman – “Applications of magnetic resonance methods for development of quantum technologies”

11:00 – 11:30 **Coffee break**

11:30 – 12:30 Sh. Latypov – “Modern high-resolution NMR methods for structural analysis: Interplay of experiment and DFT calculations of NMR parameters”

**Oral Session** *Auditorium 254, main building of KFU.*

12:30 – 12:50 G. Bochkin - “Decay of multiple quantum NMR coherences in quasi-one-dimensional chains in calcium fluorapatite”

12:50 – 13:10 I. Lazarev - “Contributions of different parts of dipole-dipole interactions to relaxation of multiple quantum NMR coherences in a single crystal of calcium fluorapatite”

13:10 – 13:30 S. Vasil'ev - “The influence of the dipolar coupling strength on the spin dynamics of quasi-one-dimensional spin chains in fluorapatite”

14:30 – 15:00 A. Germov - “NMR study of electron-doped cubic manganites  $\text{Sr}_{1-x}\text{La}_x\text{MnO}_3$ ”

15:00 – 15:20 A. Sergeev - “Scalar 3D-gradiometer and its advantages over a scalar magnetometer”

15:20 – 15:40 V. Ushakov - “Stand for the analysis of the amplitude-time characteristics of the nuclear precession signal”

15:40 – 16:00 R. Likierov – “Investigation of  $\text{YVO}_4$  monocrystals doped by  $^{143}\text{Nd}^{3+}$  and  $^{145}\text{Nd}^{3+}$  rare earth ions by EPR and crystal-field parameters calculations”

16:00 – 16:20 K. Vasin – “Elastic interactions of spherical particles in anisotropic cubic media”

16:20 – 17:00 **Coffee break**

## PROGRAM

17:00 – 17:20 D. Nuzhina - “Experimental investigation of magnetostriction in  $\text{LiRF}_4$  (R=Yb, Tm) in the strong magnetic fields”

17:20 – 17:40 S. Gotovko - “Multiferroicity of  $\text{CuCrO}_2$  tested by ESR”

17:40 – 18:00 I. Rodygina - “Antiferromagnetic resonance in quasy-2D antiferromagnet  $\text{Ba}_2\text{MnGe}_2\text{O}_7$ ”

### **Thursday, September 27**

**Lectures**      *Auditorium 254, main building of KFU.*

9:00 – 10:00 Yu. Talanov – “Magnetic resonance in topological insulators”

10:00 – 11:00 E. Vavilova – “Introduction to solid-state NMR studies of lithium ion dynamics in potential battery materials”

11:00 – 11:30 **Coffee break**

11:30 – 12:30 S. Orlinskii – “Investigation of nature of self organization of nanosystems by magnetic resonance”

12:30 – 13:30 R. Eremina – “Investigations of hexagonal manganites by ESR methods”

### **Friday, September 28**

**Lectures**      *Auditorium 254, main building of KFU.*

9:00 – 10:00 B. Rameev – “Applications of NMR & NQR techniques for detection of energetic and dangerous materials”

10:00 – 11:00 S. Vasiliev – “Dynamic nuclear polarization in silicon at ultra-low temperatures”

11:00 – 11:30 **Coffee break**

11:30 – 12:30 Yu. Bunkov – “Magnons Bose-Einstein Condensation and Spin Superfluidity”

12:30 – 13:30 E. Alakshin – “The study of  $\text{ReF}_3$  Nanoparticles by NMR”

14:30 – 15:30 V. Dmitriev - “NMR in new superfluid phases of  $^3\text{He}$ ”

15:30 – 16:30 K. Safiullin - “Peculiar properties of gas diffusion in porous media”

16:30 – 17:00 **Coffee break**

**Oral Session**      *Auditorium 254, main building of KFU.*

17:00 – 17:20 P. Zlishcheva - “Synthesis and NMR cryoporometry of  $\text{LaF}_3$  nanosized samples”

17:20 – 17:40 I. Nekrasov - “High-field  $T_2$  MRI contrast agent based on  $\text{TbF}_3$  and  $\text{DyF}_3$  nanoparticles”

17:40 – 18:00 A. Farhutdinov - “Conventional magnon BEC in YIG films”

18:00 – 18:20 A. Stanislavovas - “Self-diffusion of gaseous  $^3\text{He}$  in oriented aerogels”

18:20 – 18:40 G. Dolgorukov - “Atomic-scale probing of paramagnetic centers in nanodiamonds by  $^3\text{He}$  NMR”

18:40                **Awards ceremony. Closing of the School**

## **The human brain: development and aging explored by MRI.**

Uwe Eichhoff

Bruker BioSpin GmbH (retired)

e-mail: [barbara.uwe@t-online.de](mailto:barbara.uwe@t-online.de)

Continuous hardware development and new advanced MRI methods play an important role in exploring finest anatomical details as well as organization of the human brain and contribute to the understanding of mental processes. The formation and development of the brain in early childhood can be followed as well as the decline of cognitive abilities in age.

The whole entity of MRI contrast mechanisms like spin density, T<sub>1</sub>, T<sub>2</sub>, T<sub>2</sub>\*, magnetic susceptibility, structural anisotropy allow segmentation of brain images into the particular brain anatomical substructures. Based on this segmentation Diffusion Tensor Imaging (DTI), MR tractography and resting state functional MRI (rs-fMRI) allow to elucidate structural (DTI) and functional connectivities (fMRI) between the various brain areas and complement anatomical findings.

These methods visualize functional connectivities through in the Blood Oxygen Level Dependent (BOLD MRI signal). Even in complete rest the brain is active and oxygen is extracted from blood and fresh blood is supplied. The detection of the small signal changes needs highest sensitivity and the MRI scans must be repeated as fast as possible. Statistical evaluation and cross-correlation of the signals in all voxels show synchrony of signal level fluctuations even in remote brain areas. This allows to establish functional networks in the brain.

The most important networks are the Default Mode Network (DMN), the Salience Network (SN) and the Central Executive Network (CEN). Anatomical locations within the brain sharing two or three of these networks determine our relation to external stimuli, our emotional reaction and activities. Applications to autism beginning in early childhood and decline of cognitive abilities in age, such as mild cognitive impairment, Alzheimer disease will be discussed.

Deep Brain Stimulation (DBS) has become now a well accepted therapy in Parkinson disease. Its application in Alzheimer and depression is still controversial Functional MRI allows to visualize the areas of stimulation and to find the optimal location for the stimulation electrodes.

## **Investigation of the spatial structure of different drugs, proteins & oligopeptides, and their complexes with models of cell membrane in solution by modern NMR spectroscopy**

V.V. Klochkov

NMR Laboratory, Institute of Physics, Kazan Federal University, 420008, 18 Kremlevskaya St., Kazan, Russian Federation

### **Aims of study. Results**

The goal of the investigation is to study conformational features and dynamics of different pharmaceutical objects such as cholesterol-lowering drugs (statins), vitamin B6, cyclosporins. Another aim of this work is investigation of the mechanisms of interaction between these compounds and cell membranes using model membranes by NMR spectroscopy methods.

BioNMR group of NMR laboratory is investigating the role of various peptides and proteins in cellular processes and disease. Our goal is to understand the function of peptides and their mechanism of cellular toxicity in terms of structure. We used high-resolution magnetic resonance (NMR) spectroscopy to determine structures of biological macromolecules such as amyloid  $\beta$ -peptides, antimicrobial peptides protegrins (PG), of the N-terminal fragments of the HIV enhancer prostatic acid phosphatase peptide (PAP), of the N-terminal domain of telomerase, insulins and integrate our structural understanding into further functional studies.

### **Experimental**

All NMR experiments were performed on a Bruker Avance III HD 700 and Bruker Avance II 500 MHz NMR spectrometers equipped with 5 mm probes and using standard Bruker TopSpin software. Assignments of  $^1\text{H}$  and  $^{13}\text{C}$  NMR signals of compounds were achieved from signal multiplicities, integral values and characteristic chemical shifts from the through-bond correlations in 2D COSY spectra, through-space correlations in 2D NOESY spectra as well as from  $^1\text{H}$ - $^{13}\text{C}$  heteronuclear correlations in 2D HSQC and HMBC spectra.

The spatial structure of different drugs and proteins in solution and in a complex with dodecylphosphocholine (DPC) and sodium dodecyl sulfate (SDS) micelles was investigated by  $^1\text{H}$  nuclear magnetic resonance spectroscopy and two-dimensional (2D) NMR spectroscopy (total correlation spectroscopy and nuclear Overhauser effect spectroscopy (NOESY)). Analysis of the interproton distances obtained from the 2D NOESY NMR spectra was used to reveal the spatial structure of different drugs and proteins. Complex formation was confirmed by the analysis of  $^1\text{H}$  chemical shifts in the NMR spectra of the drugs and the proteins and by the analysis of the signs and values of NOEs in a solution with micelles.

## **NMR Spectroscopy to Study the Structure, Dynamics and Molecular Interactions of Biopolymers**

B.I. Khairutdinov<sup>1,2</sup>, E.A. Ermakova<sup>1</sup>

<sup>1</sup>Kazan Institute of Biochemistry and Biophysics, FRC Kazan Scientific Center of RAS,  
420111, Lobachevsky str. 2/31, Kazan, Russia

<sup>2</sup>Kazan Federal University, 420008, Kremlyovskaya str. 18, Kazan, Russia

e-mail: khairutdinov@kibb.knc.ru

The modern high resolution NMR spectroscopy undergoes rapid development for the last quarter of the century. In particular the pulse sequences which allow obtaining three dimensional NMR spectra for  $^1\text{H}$ ,  $^{13}\text{C}$  and  $^{15}\text{N}$  nuclei have been developed. This technology dramatically increased assignment possibilities for the strongly overlapped spectra of proteins. Along with the achieved success in the field of expression and purification of recombinant proteins enriched with isotopes  $^{13}\text{C}$  and  $^{15}\text{N}$ , the interpretation of three-dimensional structure of proteins became possible. Indisputable advantage of NMR spectroscopy is the sensitivity of the method to chemical exchange processes that allows studying intramolecular mobility of proteins and their interaction with various ligands.

The possibilities of NMR spectroscopy for studying the structure, intramolecular mobility and intermolecular interaction of proteins and DNA fragments will be considered in the lecture. The main approaches for assignment of NMR spectra of proteins and obtaining three-dimensional structural model will be discussed. There will also be considered the use of the Lipari-Szabo formalism for calculating the values of order parameters, local correlation times and chemical exchange constants on the basis of the measured values of the relaxation times  $T_1$ ,  $T_2$  and the heteronuclear Overhauser effect on  $^{15}\text{N}$ - $^1\text{H}$  nuclei. Some examples of application of computer simulation methods together with experimental NMR spectroscopy data for constructing three-dimensional models of biopolymer complexes with ligands will be shown.

This work was partially supported by the Russian Foundation for Basic Research (grant 17-03-00858a, 12-04-01286a, 18-44-160013p\_a.)

## Electron paramagnetic resonance of atherosclerotic plaques and synthetic calcium phosphates to follow pathological calcification processes

M. Gafurov,<sup>1</sup> B. Gabbasov,<sup>1</sup> G. Mamin,<sup>1</sup> I. Ignat'ev,<sup>2,3</sup> Y. Chelyshev,<sup>1,3</sup>  
S. Orlinskii,<sup>1</sup> N. Petrakova,<sup>4</sup> A. Fedotov,<sup>4</sup> V. S. Komlev<sup>4</sup>

<sup>1</sup>Kazan Federal University, Kremlevskaya 18, 420008, Kazan, Russia

<sup>2</sup>Interregional Clinical and Diagnostic Centre, Karbysheva 12A, 420101, Kazan, Russia

<sup>3</sup>Kazan State Medical University, Butlerova 49, 420012, Kazan, Russia

<sup>4</sup>A.A. Baikov Institute of Metallurgy and Materials Science, Russian Academy of Sciences,  
Leninsky pr. 49, 119334, Moscow, Russia

e-mail: marat.gafurov@kpfu.ru

Atherosclerosis (AS) is a chronic progressive inflammatory process in arterial vessels, initiated by the damage of endothelial cells with the involvement of monocytes, macrophages and dendritic cells being under conditions of oxidative stress. AS is a cause of thrombosis of arteries, leading to acute cardiovascular complications. Generally, the thrombosis is usually preceded by a fibrous cap rupture of AS plaques (ASP) and, to a lesser extent, a superficial erosion of endothelium. Understanding the physical and chemical factors that are connected with the ASP calcification and stability is a matter of controversy and extensive investigations [1, 2].

We have studied plaque tissues of aorta walls from male patients with AS gathered postmortem or during carotid endarterectomy operations. The micromorphology and chemical content were defined by scanning electron microscopy (SEM, Merlin), electron dispersive spectrometer (EDS, AZtec), X-ray diffraction (XRD, D8-Advance). Pulsed EPR and ENDOR are done at 94 GHz, T = 6-300 K (Bruker E-680) for native and radiation-induced paramagnetic centres. The results are compared with those obtained for “pure” and cation-substituted synthetic calcium phosphates – hydroxyapatite (HA), tricalcium phosphate (TCP), octacalcium phosphate (OCP).

From the SEM/EDS/XRD the presence of only HA in the calcified (Ca/P > 1.0) and other CaP (probably TCP and OCP) in samples with Ca/P < 0.6 was found. By XRD in some samples nanosized HA deposits (< 50 nm) were detected. Mn<sup>2+</sup> and radiation-induced CO<sub>2</sub><sup>-</sup> radicals were detected and identified by EPR. Their EPR spectral and relaxation characteristics depends on the calcification degree, location (cap, shoulders or core of ASP), ASP stability. Correlation (p < 0.05) between the relaxation characteristics of Mn<sup>2+</sup> ions and ASP stability was found [3-5]. The results show that due to the small sample volume (500 nL, 0.5 mm cross section) and high spectral resolution pulsed high-field EPR can be used as a tool to study different parts of ASP to follow the presence of paramagnetic centers and calcification processes.

### Acknowledgements

Authors are thankful to V. Putlyaev, E. Klimashina, A. Zanochnik, Y. Osin, A. Kiiamov, I. Fadeeva for sample preparation and characterization. A financial support of RFBR grant # 18-29-11086 is gratefully acknowledged.

## LECTURE NOTES

### References

- [1] L.G. Gilinskaya et al., *J. Struct. Chem.*, **2003**, *44*, 813-820.
- [2] I.M. Ignat'ev et al., *Angiology and vascular surgery*, **2017**, *23*, 13-20.
- [3] V.A. Abdul'yanov et al., *JETP Lett.*, **2008**, *88*, 69-73.
- [4] Y. Chelyshev et al., *BioMed Res. Int.*, **2016**, *2016*, 3706280(1-11).
- [5] B. Gabbasov et al., *J. Magn. Magn. Mater.*, **2018**,  
<https://doi.org/10.1016/j.jmmm.2018.02.039>.

## **NMR spectroscopy applications in structural studies of *Staphylococcus aureus* ribosome hibernation mediated by intermolecular interactions of HPF**

K.S. Usachev<sup>1</sup>, A.G. Bikmullin<sup>1</sup>, A.A. Golubev<sup>1</sup>, N.S. Garaeva<sup>1</sup>, L.I. Nurullina<sup>1</sup>, I.Sh. Khusainov<sup>1,2</sup>, N. Trachtmann<sup>1,3</sup>, Sh.Z. Validov<sup>1</sup>, V.V. Klochkov<sup>1</sup>, A.V. Aganov<sup>1</sup>, B. Kieffer<sup>2</sup>, M.M. Yusupov<sup>1,2</sup>

<sup>1</sup> Kazan Federal University, 420008, Kremlevskaya st.18, Kazan, Russia.

<sup>2</sup> Institut de Génétique et de Biologie Moléculaire et Cellulaire, Université de Strasbourg, 67400, 1 Rue Laurent Fries, Illkirch-Graffenstaden, France.

<sup>3</sup> Institute of microbiology University of Stuttgart, 70569, Allmandring 31, Stuttgart, Germany.

e-mail: k.usachev@kpfu.ru

Last decades significant progress has been made on structural studies of the mechanism of protein synthesis in the cell. Crystal structure of the ribosome and several ribosome functional complexes modeling different steps of protein synthesis has been determined at atomic resolution. These studies created a background for three-dimensional modeling of biochemical reactions of protein synthesis. Current knowledge of ribosome structure and other molecular compounds of translation apparatus allow to study cellular regulations of these processes with involvement small molecules such as metabolites. It is become important to make extension of basic knowledge and to study pathogenic organisms and to find specific differences of organization of protein synthesis systems of pathogenic.

*Staphylococcus aureus* is one of the major human pathogens, which causes numerous community associated and hospital-acquired infections. Over the past decade, the changing pattern of resistance in *S. aureus* has underscored the need for new antimicrobial agents. One of the main target of antibiotic in bacteria is the ribosome - the ribonucleoprotein particle that performs protein synthesis in the cell. More than 40% of clinically useful antibiotics target the ribosome apparatus. Ribosome catalyzes sequential polymerization of amino acids into proteins according to the genetic code specified by a messenger RNA (mRNA) template. During the translational cycle (initiation, elongation, termination and recycling) the ribosome interacts with several protein factors. Thus, the ribosome is both an enzyme and a molecular motor. The protein synthesis machinery is essential to all living cells, and it is one of the major targets for clinical treatment of bacterial infections.

Bacteria and especially pathogenic species often cope with stress and nutrients limitations, and their survival strongly depends on the ability to preserve energy. One of the most beneficial mechanism to save energy for bacterium is deactivation of its own translation machinery, namely hibernation of ribosomes. When bacteria enter a stationary phase or cease to grow due to nutrient starvation or other stress, their protein synthesis slows down by converting ribosomes into translationally inactive 100S dimers or 70S monomers. This process occurs in the presence of ribosomal binding proteins such as RMF, YfiA, HPF and SRA, which are expressed throughout the stationary phase. *Staphylococcus aureus* hibernation-promoting factor (SaHPF) is a 22,2 kDa stationary-phase protein that binds to the ribosome and turns it to the inactive form favoring survival under stress. Sequence analysis has shown that this protein is combination of two homolog proteins obtained in *E.coli* - ribosome hibernation promoting factor HPF (11 000 Da) and ribosome modulation factor RMF (6,500 Da). The N-terminal part of SaHPF shares high sequence homology with proteins HPF and YfiA from *E. coli*, suggesting its similar binding site on the ribosome. In contrast, C-terminal part shares little homology with RMF protein suggesting a different

## LECTURE NOTES

ribosome binding site and mode of action [1]. Recent studies demonstrated that truncation of last 42-90 amino acids of SaHPF protein prevents the formation of 100S and reduces the ability of the protein to bind 70S ribosomes [2]. Our recent cryo-EM studies at near-atomic resolution (3.7 Å) of the *S. aureus* 100S ribosomes revealed that the SaHPF N-terminal domain (NTD) binds to the ribosome similarly to HPF and YfiA of *E. coli*, however its CTD protrudes outside of the ribosome where it forms a dimer with SaHPF (CTD) from the second ribosome, thus dimerizing two 70S particles [3-5]. The structures of full dimers of hibernating ribosomes solved at 9–11 Å revealed the direct involvement of the SaHPF-CTD in dimerization. In order to elucidate the structure, dynamics and function of SaHPF we produced a recombinant expression, synthesis and purification protocols of <sup>13</sup>C, <sup>15</sup>N-labeled SaHPF protein for structural studies by high-resolution NMR spectroscopy. Structural analysis of the SaHPF by NMR spectroscopy showed that NTD contains two α-helices and four β-strands (β1-α1-β2-β3-β4-α2 topology), and CTD exist as a homodimer with a β1-α-β2-β3-β4 topology. Two molecules within the dimer interact through the hydrophobic interface between β2-β3-β4 strands of β-sheets, which are formed by β1 from the first chain and β2-β3-β4 from the second chain. The interface is stabilized by several pairwise interactions: Thr171 – Thr187, Ile173 – Val162, Phe160 – Tyr175, Phe160 – Phe160 (Figure 1) [5].

Obtained SaHPF-NTD structure by NMR spectroscopy was used for further analysis of its binding with *S. aureus* 70S ribosome by HET-SOFAST NMR experiments and for competition experiments with tigecycline which bind to the A site and interfere with SaHPF NTD position. By HET-SOFAST NMR experiments we determined several protein regions which are close to the ribosome RNAs. Its β sheet interacts with 16S rRNA on the head (stacking interactions between Glu5/His7 and A975, and between Arg66 and G976), while conserved positively charged residues belonging to the α helices (Lys27, Arg30, Lys84, Arg90, Arg95) stabilize the interaction with 16S rRNA from the body. Competition

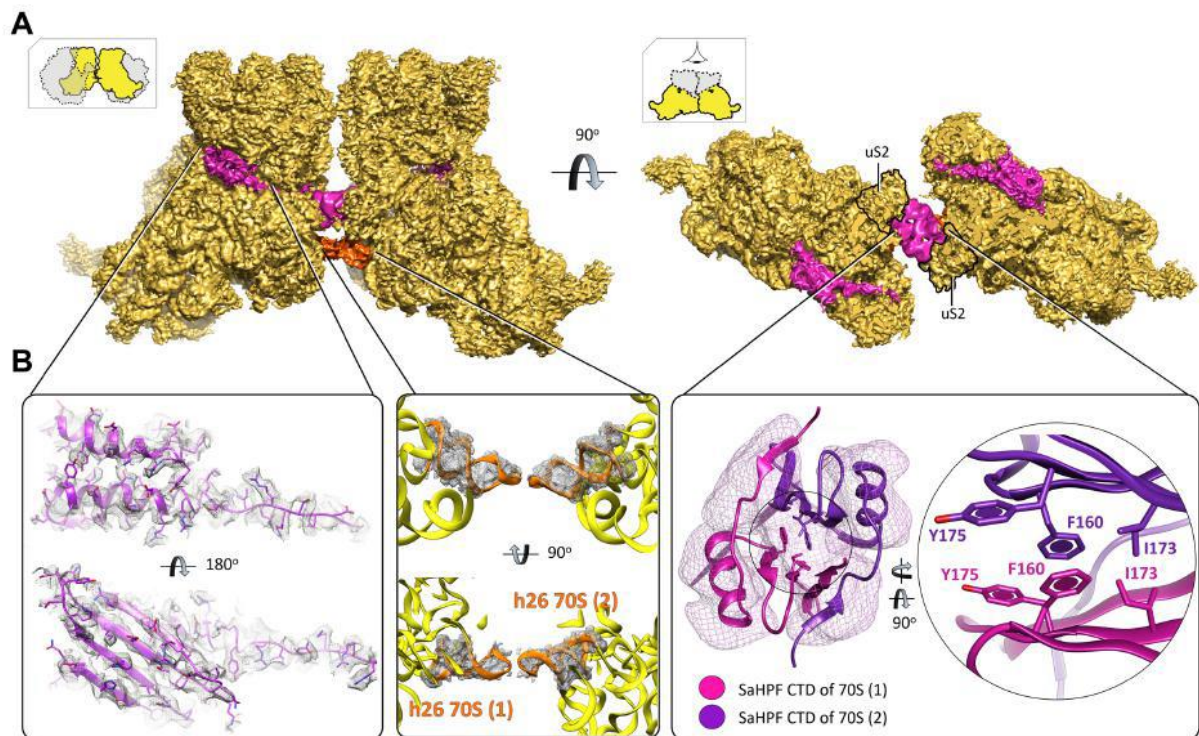


**Figure 1.** Cryo-electron microscopy structure at 3.7 Å resolution of 100S ribosome from *S. aureus* in the presence of SaHPF. Ribosome dimerization occurs via interaction of the C-terminal domain of SaHPF, and via interactions involving h26 (Figure adapted from[5]).

## LECTURE NOTES

experiments of SaHPF with antibiotics shown that tigecycline didn't supersede the SaHPF from ribosome site but changes the mode of spin diffusion pattern of the several residues from  $\beta$ -sheet interface, indicating that it colocalise with SaHPF. The obtained structural data about the interface of SaHPF (CTD) dimer may be further used as the target for development of compounds to prevent ribosome dimerization in *S. aureus*.

This work was supported by the Russian Science Foundation (grant 16-14-10014).

### References

- [1] Ayupov, R. K. & Akberova, N. I. (2016). Analysis of the Structure of SaHPF Staphylococcus aureus Protein. *Uchenye Zapiski Kazanskogo Universiteta-Seriya Estestvennye Nauki* 158, 327-337
- [2] Basu, A. & Yap, M. N. F. (2016). Ribosome hibernation factor promotes Staphylococcal survival and differentially represses translation. *Nucleic Acids Research* 44, 4881-4893.
- [3] Yoshida, H. & Wada, A. (2014). The 100S ribosome: ribosomal hibernation induced by stress. *Wiley Interdiscip Rev RNA* 5, 723-32.
- [4] Ueta, M., Ohniwa, R. L., Yoshida, H., Maki, Y., Wada, C. & Wada, A. (2008). Role of HPF (hibernation promoting factor) in translational activity in Escherichia coli. *Journal of Biochemistry* 143, 425-433.
- [5] Khusainov, I., Vicens, Q., Ayupov, R., Usachev, K., Myasnikov, A., Simonetti, A., Validov, S., Kieffer, B., Yusupova, G., Yusupov, M. & Hashem, Y. (2017). Structures and dynamics of hibernating ribosomes from Staphylococcus aureus mediated by intermolecular interactions of HPF. *EMBO Journal* 36, 2073-2087.

## **Random walks in disordered lattice, CTRW, memory and dipole transport**

F.S. Dzheparov

National Research Center “Kurchatov Institute” - ITEP, Moscow 117258, Russia

e-mail: dzheparov@itep.ru

Application of CTRW (continuous time random walks) to dipole hopping transport is reviewed [1]. Conditions of applicability of basic kinetic equations to spin systems are indicated. Correct versions of derivation of the CTRW-equations are presented. Existence of different forms of memory kernels is demonstrated. Correction of Scher-Lax memory kernel within geometrical memory approach is fulfilled in accordance with leading terms of concentration expansion. Approximate solution for autocorrelation function is considered. Modern state of numerical simulation and experimental measurements of autocorrelation function in nuclear polarization delocalization are described. It is shown, that application of the CTRW was more successful in description of dipole transport than for hopping conductivity.

### **References**

[1] F.S.Dzheparov. Magn. Reson. Solids 19, 17201 (2017)

## Applications of magnetic resonance methods for development of quantum technologies

E.B. Fel'dman

Theoretical Department, Institute of Problems of Chemical Physics of RAS, 142432,  
Chernogolovka, Russia

e-mail: [efeldman@icp.ac.ru](mailto:efeldman@icp.ac.ru)

Reasons for using methods of nuclear magnetic resonance (NMR) in problems of quantum informatics are discussed. Special attention is paid to solid state NMR for quantum information processing [1]. Quantum entanglement and quantum discord as measures of quantum correlations are considered in detail [2]. One-dimensional systems of spins connected by the XY-Hamiltonian (chains and rings) are studied. In particular, we worked out a method of exact diagonalization of the XY-Hamiltonian in alternating open spin chains. That method is used for an investigation of quantum correlations in dimer systems. In the simplest multi-pulse experiment, multi-pulse spin locking, methods of calculation of quantum discord are developed both for low and high temperatures [3]. A condition of the emergence of quantum correlations in the multi-pulse spin locking is obtained for two-spin systems. Quantum correlations are investigated in multiple quantum (MQ) NMR [4] for two-spin systems. A theory of dipolar relaxation of MQ NMR coherences is developed for one-dimensional systems [5]. The theoretical predictions agree with the obtained experimental data. It is shown that the relaxation of the MQ NMR coherence of the second order can be considered as a model of decoherence in many-qubit coherent clusters [6]. The dependence of the decoherence rate on the number of spins is also obtained.

The work is supported by Russian Foundation of Basic Research (Grant №16-03-00056).

### References

- [1] E.B.Fel'dman, A.N.Pyrkov, A.I.Zenchuk. Solid state multiple-quantum NMR in quantum information processing: exactly solvable models. *Phil.Trans.R.Soc.A370*, 4690-4712 (2012)
- [2] S.M.Aldoshin, E.B.Fel'dman, M.A.Yurishchev. Quantum entanglement and quantum discord in magnetoactive materials. *Low Temp. Phys.* 40, 3 (2014)
- [3] S.A.Gerasev, A.V.Fedorova, E.B.Fel'dman, E.I.Kuznetsova. Theoretical investigations of quantum correlations in NMR-multi-pulse spin-locking experiments. *Quantum Information Processing* 17, 72 (2018)
- [4] J.Baum, M.Munowitz, A.N.Garroway, and A. Pines. Multiple-quantum dynamics in solid state NMR. *J. Chem. Phys.* 83, 2015–2025 (1985).
- [5] G.A. Bochkin, E.B. Fel'dman, S.G.Vasil'ev, V.I. Volkov. Dipolar relaxation of multiple quantum NMR coherences in one-dimensional systems. *Chem. Phys. Lett.* 680, 56–60 (2017).
- [6] G.A. Bochkin, E.B. Fel'dman, S.G. Vasil'ev, V.I. Volkov. Dipolar relaxation of multiple quantum coherences as a model of decoherence of many-qubit coherent clusters. *Appl.Magn.Reson.* 49 (2018) 25–34.

## **Modern high-resolution NMR methods for structural analysis: Interplay of experiment and DFT calculations of NMR parameters**

Sh.K. Latypov

Arbuzov Institute of Organic and Physical Chemistry, FRC Kazan Scientific Center of RAS,  
Kazan, Tatarsan, Russian Federation

e-mail: [lsk@iopc.ru](mailto:lsk@iopc.ru)

The rational design of new compounds and materials requires a reliable information on chemical, conformational and supramolecular structure, particularly in solutions. In this respect, high-resolution NMR spectroscopy is one of the most powerful method. However, NMR also has its limitations - absolute sensitivity is low compared to other spectral methods, as well as the indistinguishability of symmetric fragments in NMR spectra. Another disadvantage of the method is also its time scale – many processes are fast under normal conditions. These problems are particularly relevant in the study of metal complexes which are effective catalysts for various important reactions, including some biochemical processes.

This report will explore methods and techniques to overcome some of the limitations of this method. The use of non-empirical calculations of NMR parameters will also be considered. The effectiveness of combined use of NMR experiments and DFT calculations will be demonstrated on the examples of conformational analysis of a number of new ligands and metal complexes based on them.

This work was financially supported by the RFBR (grant No. 18-43-160003).

**Magnetic resonance in topological insulators**

Yu. I. Talanov

Zavoisky Physical-Technical Institute, 420029 Sibirsky Tract 10/7, Kazan, Russian Federation

e-mail: [talanov@kfti.knc.ru](mailto:talanov@kfti.knc.ru)

Topological insulators (TI) are a new class of quantum materials, which are characterized by a full insulating gap in the bulk and gapless surface states with Dirac-like dispersion [1-3]. In the surface state, the current direction and the spin polarization is tightly connected via strong spin-orbit coupling (right- and left-moving electrons carry up and down spins, respectively). This gives a new opportunity for generation and control of spin currents with low energy dissipation. The topological insulators have been theoretically predicted at first [4] and then experimentally observed in many systems, such as HgTe quantum wells, BiSb alloys, Bi<sub>2</sub>Te<sub>3</sub> and Bi<sub>2</sub>Se<sub>3</sub> crystals.

The nontrivial topological properties of these materials is protected by time-reversal symmetry (TRS). The breaking of this symmetry under the action of a magnetic field gives rise to different topological states. One can realize the effect of breaking TRS by the doping of TI with magnetic ions. While at the low doping level TI remain stable to such perturbations, at higher doping the ferromagnetic ordering takes place [5] and the TRS is broken due to appearance of the spontaneous magnetization. The magnetic ordering of the embedded ions is driven by indirect Ruderman-Kittel-Kasuya-Yosida (RKKY) coupling via the charge carriers [6,7]. At the same time, the doped magnetic ions play a role of the local spin probes, which may be used as a sensitive tool for monitoring the magnetic and electronic properties of a system. This possibility is realized in some works reviewed in the present report. They are focused on the studies of the local properties of the materials based on Bi<sub>2</sub>Se<sub>3</sub> and Bi<sub>2</sub>Te<sub>3</sub> with magnetic ions doping.

The strength of the RKKY coupling is very sensitive to the peculiarities of the band structure in the vicinity of a Fermi level. As a consequence, the widely known topological insulators Bi<sub>2</sub>Se<sub>3</sub> and Bi<sub>2</sub>Te<sub>3</sub> mentioned above reveal quite different magnetic properties at doping by magnetic ions, in particular, by manganese. While for the first one the features of ferromagnetic ordering manifest themselves only for strong doping (more than 12.5% of Bi is substituted by Mn) and at temperatures below 2K, the later becomes ferromagnetic already at 1% of Mn with the Curie temperature reaching the value of 12K for 2.5%. It was shown that such difference is due to the nonmagnetic energy gap in the vicinity of the Dirac point for Bi<sub>2</sub>Se<sub>3</sub>, which hinders the magnetic correlation in this compound [8]. These peculiarities manifest themselves in the magnetic resonance spectra with different behavior of the Mn<sup>2+</sup> in Bi<sub>2</sub>Se<sub>3</sub> in comparison with Bi<sub>2</sub>Te<sub>3</sub>. The ESR of manganese doped Bi<sub>2</sub>Se<sub>3</sub> was studied in details in Ref. [9]. In this work in addition to the observation of fine structure the parameters of the spin-hamiltonian have been obtained, such as *g*-factor (1.91) and the zero-field splitting of the Kramers doublet ( $D=0.28 \text{ cm}^{-1}$ ). On the other hand, no evidences of magnetic correlations were found in this compound, whereas the strong influence of the indirect coupling of the manganese ions on the magnetic properties of Mn doped Bi<sub>2</sub>Te<sub>3</sub> have been obtained via the ESR study of Ref.[10,11]. For this compound the indirect exchange results in magnetic ordering and eliminates the possible fine structure of the ESR spectrum of doped Mn<sup>2+</sup> ions. Thus, even at modest doping the data reveal the specific critical behaviour confirming the ferromagnetic ordering of Mn spins which induces the loss of the TRS symmetry. On the contrary, if the comparable amount of local moments get formed due to the

intrinsic anti-site substitutional defects [12] the analysis of experimental data evidences in favour of spin-glass state with zero average magnetization [13]. Therefore, in the absence of external field the TRS is not violated. One of the main reasons of this difference is that the mean distance between the doped magnetic moments may be much smaller than the typical scale connected with the nonmagnetic impurities thus making the magnetic ordering more favourable. For the case of intrinsic magnetic moments induced by the structural defects, the mean distance between the magnetic moments is comparable with the characteristic disorder scale thus stimulating the spin-glass state. Nevertheless, there exist possibilities to generate ferromagnetism without introducing any magnetic dopants. They are connected with the experimental fabrication of magnetically nanostructured hierarchical architectures of  $\text{Bi}_2\text{Te}_3$  [12] base on the large amount of the specially introduced nonmagnetic defects.

### References

- [1] M. Z. Hasan, C. L. Kane, Rev. Mod. Phys. 82, 3045 (2010).
- [2] J. E. Moore, Nature 464, 194 (2010).
- [3] X.-L. Qi, S.-C. Zhang, Rev. Mod. Phys. 83, 1057 (2011).
- [4] C. L. Kane, E. J. Mele, Phys. Rev. Lett. 95, 226801 (2005).
- [5] Y.S. Hor, P. Roushan, et al., Phys. Rev. B 81, 195203 (2010).
- [6] Qin Liu et al., Phys. Rev. Lett. 102, 156603 (2009).
- [7] D. A. Abanin, D. A. Pesin, Phys. Rev. Lett. 106, 136802 (2010).
- [8] J. Sanchez-Barriga, A. Varykhalov, G. Springholz, et al., Nat. Commun. 7, 10559 (2016).
- [9] A. Wolos, A. Drabinska, M. Kaminska, arXiv:1412.2012.
- [10] S. Zimmermann, F. Steckel, C. Hess, et al., Phys. Rev. B 94, 125205 (2016).
- [11] V. Sakhin, E. Kukovitskii, N. Garif'yanov, et al., J. Supercond. Nov. Magn. 30, 63 (2017).
- [12] Guanjun Xiao, Chunye Zhu, Yanming Ma, et al., Angew. Chem. Int. Ed. 53, 729 (2014).
- [13] V. Sakhin, E. Kukovitskii, N. Garif'yanov, et al., JMMM 459, 2018, 290 (2018).

**Introduction to solid-state NMR studies of lithium ion dynamics in potential battery materials.**

E.L. Vavilova<sup>1</sup>

<sup>1</sup>ZPTI-Subdivision of FIC “Kazan Scientific Center of RAS”, 420029, Sibirskii Trakt 10/7, Kazan, Russia.

e-mail: [jenia.vavilova@gmail.com](mailto:jenia.vavilova@gmail.com)

Materials that are promising for using in solid-state lithium-ion batteries have high self-diffusion of Li<sup>+</sup> ions. The study of the dynamics of Li ions by nuclear magnetic resonance (NMR) method helps to search for potential electrode and electrolyte materials. Solid-state NMR is widely used to study the local structure and dynamics in many of these new materials, singly and in combination with other methods such as diffraction, electron microscopy, conductometry and others. In this lecture we briefly consider the phenomenon of diffusion and ion mobility in solids and the basic NMR methods used to probe them. Examples of the application of solid-state NMR methods for studying different classes of cathode materials will be demonstrated.

## Investigations of hexagonal manganites by ESR methods

I. Yatsyk<sup>1,2</sup>, T. P. Gavrilova<sup>1,2</sup>, R. M. Eremina<sup>1,2</sup>, V. V. Parfenov<sup>2</sup>

<sup>1</sup>E. K. Zavoisky Physical-Technical Institute RAS, 420029 Kazan, Russia

<sup>2</sup>Kazan (Volga region) Federal University, 420008 Kazan, Russia

e-mail: REremina@yandex.ru

Multiferroic rare earth manganites  $\text{RMnO}_3$  have attracted a great attention due to their manifestations of significant couplings between the magnetic and electric order parameters.  $\text{RMnO}_3$  compounds have two kinds of multiferroic structures: hexagonal and orthorhombic depending on the rare earth  $\text{R}^{3+}$  ionic size and coordination number from 1.36 Å (La, NC = 12) to 0.98 Å (Lu, NC = 8) [1]. The orthorhombic structure with a  $Pnma$  space group ( $Pbnm$  in another, more convenient crystallographic setting) forms the stable crystal structure of  $\text{RMnO}_3$  perovskite oxides with R from La to Dy, which belongs to materials exhibiting colossal magnetic resistance at hole doping (R = La - Eu) and to the ferroelectrics induced by magnetic ordering (R = Dy - Gd). Furthermore, another family of compounds with smaller ionic size (with R from Ho to Lu) forms the stable hexagonal structure with  $P6_3cm$  space group at room and lower temperatures and exhibits multiferroic properties as well. [2, 3]. The coexistence of ferroic orders in  $\text{RMnO}_3$  with hexagonal or orthorhombic structure yields complex physics in the strong interactions among charge, orbital, lattice, and spin degrees of freedom. They also have fascinating physical properties which might lead to promising applications. For example, the hexagonal manganite  $\text{YbMnO}_3$  exhibits a ferroelectric (FE) transition well above room temperature ( $>900$  K), while the antiferromagnetic (AFM) ordering takes place at much lower temperature (Neel temperature  $T_N \sim 80$  K). Really, manganites have the very rich (H-T) phase diagram. A. Midya et al. have systematically investigated the magnetic properties in  $\text{RMnO}_3$  (R = Dy, Tb, Ho, and Yb) single crystals [4]. The detailed analysis of magnetization data showed that the magnetic interaction within the rare-earth sublattice in multiferroics  $\text{RMnO}_3$  is highly anisotropic (except R = Yb). Above a critical value of applied field ( $H_c$ ),  $\text{RMnO}_3$  undergo a first-order antiferromagnetic (AFM) to ferromagnetic (FM) transition below the ordering temperature ( $T_N^R$ ) of  $\text{R}^{3+}$  moment and a second-order FM to paramagnetic (PM) transition above  $T_N^R$ . Both H and T dependence of M shows that the system is highly anisotropic in the FM as well as PM states. Similar to other multiferroic manganites, the magnetic properties of rare-earth sublattice in  $\text{YbMnO}_3$  are sensitive to the direction of applied field with respect to crystallographic axis. Magnetization M is slightly larger along the c axis as compared to basal plane and two field-induced transitions are clearly visible, unlike  $\text{HoMnO}_3$ ; however, M along a axis increases smoothly with H similar to that in  $\text{HoMnO}_3$  crystal. This behavior is quite different from other multiferroic manganites where M along two axes is significantly different. This suggests that  $\text{YbMnO}_3$  is magnetically less anisotropic and the AFM interaction along both the axes is strong. Indeed, from the magnetization measurements in the paramagnetic state, A. Midya et al observed that  $\theta_{cw}$  is large and negative along both the crystallographic axes and their values are 195 and 225 K within the basal plane and along c axis, respectively [4]. The parameters of isotropic exchange and Dzyaloshinsky-Moria interactions have been obtained in h- $\text{YMnO}_3$ : J=2.3 meV [5], J=3 meV [6], J=2.7 meV, D=0.33meV,  $\theta_{cw}=930\text{K}$  [7] and for h- $\text{HoMnO}_3$ : J=2.44meV, D=0.38 meV,  $\theta_{cw}=875\text{K}$  [8].

In this work we study the physical properties of h- $\text{YMnO}_3$ , h- $\text{HoMnO}_3$  monocrystals and h- $\text{YbMnO}_3$  ceramic samples by electron spin resonance (ESR) methods. The X-ray fluorescence analyses (XFA) were carried out on X-ray fluorescence spectrometer Bruker S2 Ranger at room temperature in Kazan Federal University. Electron spin resonance (ESR)

# LECTURE NOTES

**Table 1.** The fluoresced X-ray data.

YMnO <sub>3</sub>				HoMnO <sub>3</sub>				
No	1	2	3		1	2		
Mn	44.47	42.12	41.75	<42.78>	Mn	51.02	51.05	<51.035>
Y	55.53	57.88	58.25	<57.22>	Ho	48.98	48.95	<48.965>

measurements were carried out on a Bruker EMX/plus and Bruker ELEXSYS E680 spectrometers in the temperature range of 90 - 320K at the frequencies 9.4GHz.

The monocrystal samples holmium manganite HoMnO<sub>3</sub> were synthesized in Kirensky Institute of Physics (Krasnoyarsk, Russia), and the monocrystal samples yttrium manganite YMnO<sub>3</sub> were synthesized in Laboratory, Department of Physics, Oxford University by Dharmalingam Prabhakaran. The YbMnO<sub>3</sub> ceramics were obtained according to the standard ceramic technology with preliminary solid-phase synthesis in Kazan Federal University.

X-ray Fluorescence (XRF) and Particle-Induced X-ray Emission (PIXE) are the two well-established nondestructive analytical techniques of X-ray emission spectroscopy. These techniques are powerful tools for rapid multielement nondestructive analyses and enable simultaneous detection of many elements in a solid or liquid with high-detection sensitivities, even in those cases where only small sample amounts are available. The fluoresced X-rays from the sample are collected and displayed with either energy dispersive or wavelength dispersive detector systems. The elements are identified by the wavelengths (qualitative) of the emitted X-rays while the concentrations of the elements present in the sample are determined by the intensity of those X-rays (quantitative). (XRF). The XFA data for of h-

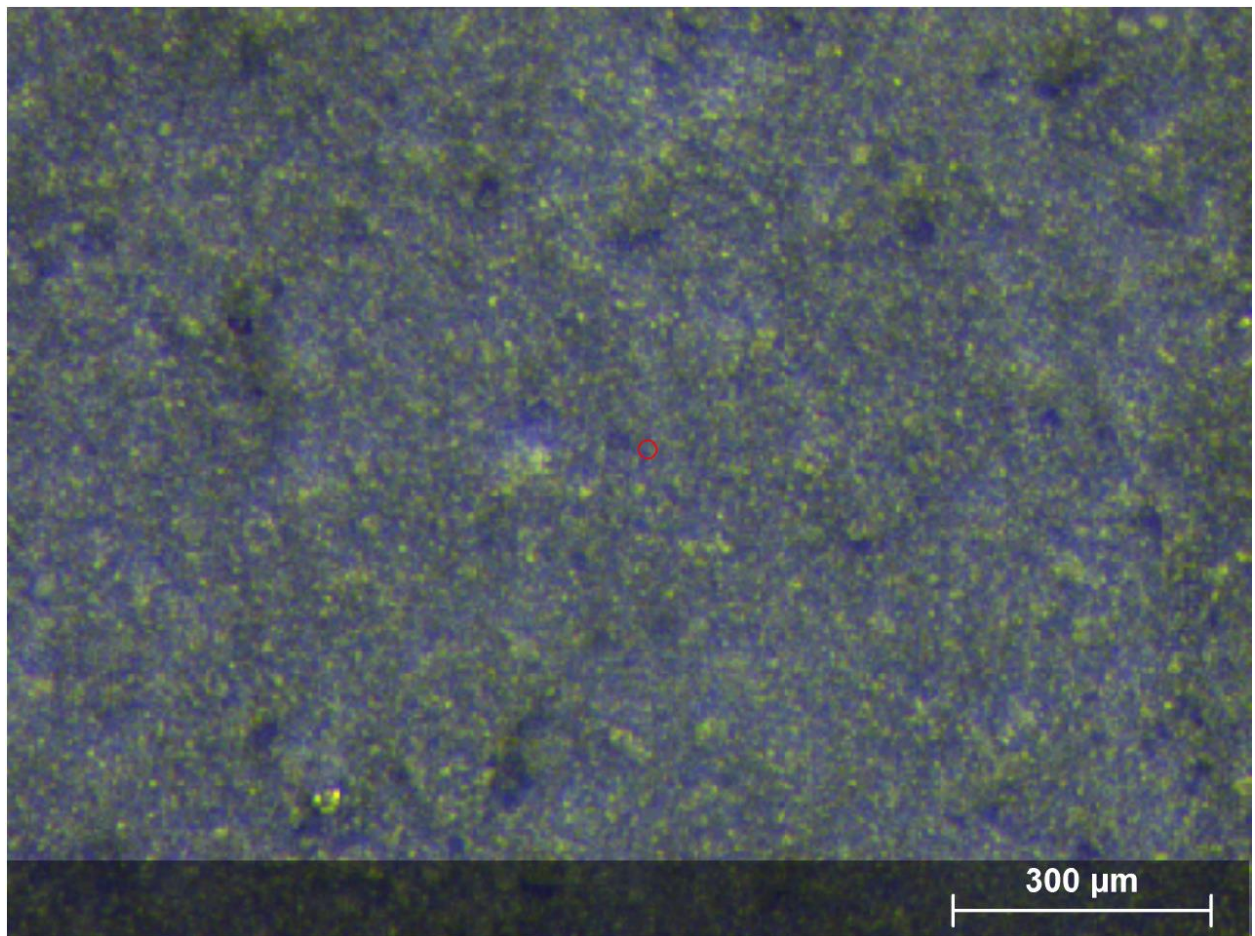


**Figure 1.** XRF image of YbMnO<sub>3</sub> at room temperatures.

YMnO<sub>3</sub> and h-HoMnO<sub>3</sub> are presented in Table. 1.

The corresponding analysis for h-YbMnO<sub>3</sub> shows that the atomic ratio of ytterbium to manganese ions is  $N_{Yb}/N_{Mn} \approx 44.48/55.02 \approx 0.81$  for bright region in Fig. 1.

The dark areas correspond to the regions with the stoichiometric ratio of ions  $N_{Yb}/N_{Mn} \approx 49.19/49.90 \approx 0.99$ . The XFA image of h-YMnO<sub>3</sub> is presented in Fig. 2b, where bright areas (yellow areas) correspond to the regions with a deficit of ytterbium. As can be seen from the analysis, a deficit of ytterbium ions is observed in h-YbMnO<sub>3</sub>, an excess of yttrium ions is detected in h-YMnO<sub>3</sub>  $N_Y/N_{Mn} \approx 57.22/42.78 \approx 1/0.75$ , and for Ho-manganite, the ratio between manganese and holmium ions is practically the same. The unequal relationship between ions of rare earth and manganese leads to a different behavior of the ESR spectra.

In all temperature range the ESR spectrum of YbMnO<sub>3</sub> ytterbium manganite can be described of one exchange-narrowed resonance line, which is well fitted (Fig. 2 a) by the following line shape [9]:

$$\frac{dP}{dH} = \frac{d}{DH} \left( \frac{\Delta H + \alpha(H - H_0)}{\Delta H^2 + (H - H_0)^2} + \frac{\Delta H - \alpha(H + H_0)}{\Delta H^2 + (H + H_0)^2} \right) \quad (1)$$

Eq. 1 corresponds to the asymmetric Lorentzian line, which includes both absorption and dispersion, where denotes the dispersion-to-absorption (D/A) ratio. Since the line width  $H$  in these samples is on the same order of magnitude as the resonance field  $H_0$ , the circular components of the exciting linearly polarized microwave field were taken into account and therefore the Eq. 1 also includes the resonance at reversed magnetic field  $H_0$ .

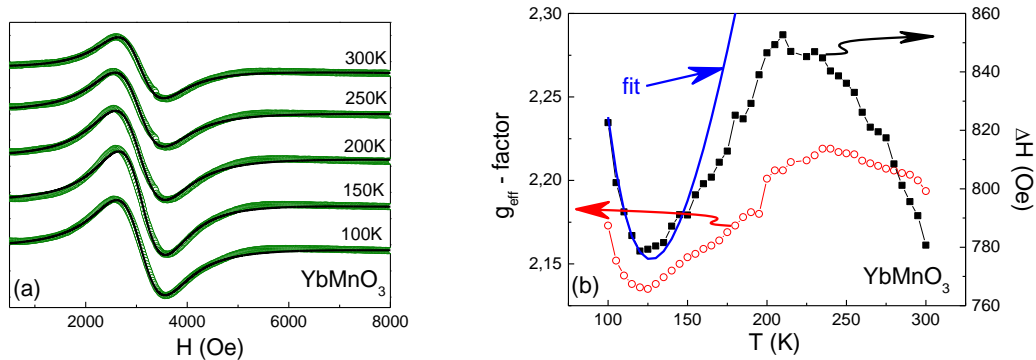


**Figure 2.** (a) ESR spectra of YbMnO<sub>3</sub> at different temperatures. Symbols - experimental data, solid line - fitting by the Eq. (3). (b) Temperature dependence of the parameters of ESR spectra: g-factor and line width, solid line – fitting by the Eq. (4).

In the total temperature range the g-factor of the ESR line in YbMnO<sub>3</sub> is above 2.1 and the ESR line width is about 800 Oe (Fig. 10 b), that is 2.3 times less that for example in other manganites La<sub>0.95</sub>Sr<sub>0.05</sub>MnO<sub>3</sub> or in GdMnO<sub>3</sub>, where the linewidth of the ESR signal at room temperature is several thousand Oersted, and the effective g-factor is less than 2 [10, 11]. It should be noted that in hexagonal manganites, the Dzyaloshinsky-Moria interaction can lead to a significant increase in the ESR linewidth, for example, in HoMnO<sub>3</sub> ESR linewidth are equal 16 kOe, which is 20 times higher than for YbMnO<sub>3</sub>. Most probability, the line from ferromagnetically correlated nanoregions is well detected in the ESR spectrum for h-YbMnO<sub>3</sub> compound in respect to HoMnO<sub>3</sub>. Early the ESR signal from ferromagnetically correlated nanoregions was observed for h-YbMnO<sub>3</sub> with the occupancy of all ytterbium positions at 88%. In our sample the occupancy of Yb (2a) position is 91 % and the position Yb (4b) is full completely filled, so the characteristics of the ferromagnetically correlated nanoregions

together with ESR parameters should be slightly different in comparison with [12], where the strong temperature dependence of the ESR parameters for ferromagnetic clusters was observed.

The value of g-factor in YbMnO<sub>3</sub> is higher than the usual value for Mn<sup>3+</sup> ions  $g = 1.99$ , that can be explained by an additional signal with  $H_{res} < 3300$  Oe, which is attributed to the ferromagnetically correlated clusters, formed by mixed-valence manganese ions near vacant Yb<sup>3+</sup> positions (that was observed in our previous work [12]). The electrical neutrality in this region with the deficit of ytterbium Yb<sup>3+</sup> ions is compiled in the case Yb<sup>3+</sup>Mn<sup>3+</sup><sub>x</sub>Mn<sup>4+</sup><sub>1-x</sub>O<sub>3</sub><sup>2-</sup>, i.e., the concentration of Mn<sup>4+</sup> ions is more than 0. Indeed, charge disbalance near the empty Yb<sup>3+</sup> position initiates a mixed-valence states formation between neighboring Mn ions. Further, the exchange interaction between Mn<sup>3+</sup> and Mn<sup>4+</sup>, so-called double exchange through oxygen anions, leads to the formation of ferromagnetically correlated nanoregion.

The authors [13-15] obtained expressions for inhomogeneous contributions to the width of the line of an ensemble of superparamagnetic particles with uniaxial anisotropy:

$$\Delta H = \Delta H(1) + \Delta H(2)$$

$$\Delta H(1) = \frac{2\alpha}{\sqrt{3}} H_0 \frac{(\xi_0 - L_1)}{\xi_0 L_1}; \quad \Delta H(2) = 3\sigma H_0 \frac{\xi_0 - 3L_1}{\xi_0^2 L_1}, \quad (2)$$

where

$\xi_0 = \frac{\mu H_0}{k_B T}$ ,  $L_1 = \coth \xi_0 - \frac{1}{\xi_0}$  - the Langevin function,  $\alpha$  - is the attenuation parameter in

the Landau-Lifshitz equation,  $\sigma = \frac{W_A}{k_B T}$ ,  $W_A$  - is the anisotropy energy of a superparamagnetic particle.

$$H_{res} = H_0 \left( 1 - 2\sigma \frac{(\xi_0 - 3L_1)^2}{\xi_0^3 L_1} \right),$$

The parameters of nanoclusters were obtained from complex analysis of the temperature dependences of position and linewidth:  $T^* = 37.5$  K;  $\mu = 200 \mu_B$ ;  $2W_A/\mu = 136$  Oe;  $H_0 = 3120$  Oe;  $\alpha = 0.025$ . As can be seen, the value of the magnetic moment in the ferromagnetically correlated regions of the ceramic YbMnO<sub>3</sub> is about  $\mu = 200 \mu_B$ , that is closed to the same value for lanthanum-strontium manganites [15]. Taking into account that the magnetic moment of the Mn<sup>3+</sup> ion in perovskites is about  $3.5 \mu_B$ , ferromagnetically correlated regions contains about 60 of the manganese ions. If we consider that the grating period is about  $7 \text{ \AA}$ , whereas the size of ferromagnetically correlated regions is about 2-3 nm.

It is found that two lines are observed in the ESR spectrum of the HoMnO<sub>3</sub> crystal. One is from ferromagnetic clusters, the second is from an exchange-related spin system. It is found that one ESR line is observed in the ESR spectrum of the YMnO<sub>3</sub> crystal. One is from an exchange-related spin system of Mn ions.

A single very broad exchange-narrowed Lorentz-shaped absorption line at a microwave frequency of 9 GHz was observed in HoMnO<sub>3</sub> and YMnO<sub>3</sub>. The line is narrowed in the center and linewidth is reduced. The phenomenon is therefore known as "exchange narrowing". The narrowing process resembles that found in nuclear resonance in a liquid. Through exchange

## LECTURE NOTES

interaction with other neighbours, any given neighboring dipole is changing its orientation at a rate of order  $J/\hbar$ .

In the case of sufficiently strong exchange interaction the ESR linewidth can be analyzed in terms of the high-temperature approach ( $k_B T \gg J$ ).

$$\Delta H = \frac{\hbar M_2}{g \mu_B \omega_{ex}}, \quad (3)$$

where  $M_2$  is the second moment of line. Second moment can be expressed in terms of the microscopic parameters of the Hamiltonian of the spin system as:

$$M_2 = \frac{\langle [H_{an}, S^+][S^-, H_{an}] \rangle}{\hbar^2 \langle S^+ S^- \rangle}. \quad (4)$$

Here  $g$ - denotes the  $g$  value,  $\hbar$  the Planck constant, and  $\mu_B$  the Bohr magneton. The second moment  $M_2$  and the exchange frequency  $\omega_{ex}$  can be expressed via microscopic Hamiltonian parameters  $H_{int}$ . The second moment shows an orientation dependence with respect to the external magnetic field, which is characteristic for the anisotropic interaction responsible for the line broadening.

The effective spin Hamiltonian has view:

$$H = JS_i S_j + D[S_i \times S_j] \quad (5)$$

where  $JS_i S_j$  is the isotropic Heisenberg exchange between neighboring spins  $S_i$  and  $S_j$ .  $D$  - antisymmetric anisotropic exchange interaction (Dzyaloshinskii-Moriya) parameter in the coordinate system with the  $z$ -axis parallel to the applied magnetic field, the interaction of spins with an external magnetic field. The transformation between the crystallographic system  $(a, b, c)$  and the coordinate system  $(x, y, z)$  is determined by expressions:

$$\begin{aligned} D_x &= D_a \cos \beta \cos \alpha + D_b \cos \beta \sin \alpha - D_c \sin \beta, \\ D_y &= D_a \cos \alpha - D_b \sin \alpha, \\ D_z &= D_a \sin \beta \cos \alpha + D_b \sin \beta \sin \alpha + D_c \cos \beta, \end{aligned} \quad (6)$$

where  $\cos \alpha$  and  $\cos \beta$  are determined by the expressions (13) in [16]. The second and fourth moments are expressed as for spins in chain:

$$\begin{aligned} M_2 &= \frac{2N}{3} [D_x^2 + D_y^2 + 2D_z^2], \\ M_4 &= \frac{4N(2N-1)J^2}{3} [D_x^2 + D_y^2 + 2D_z^2], \end{aligned} \quad (7)$$

where  $N = S(S + 1)$ . Using these ratios we fitted the angular dependencies of ESR linewidth in  $\text{HoMnO}_3$  and  $\text{YMnO}_3$  (see Fig. 3-4). As can be seen from the figure 4, using the literature data  $D=3.76\text{K}$ ,  $J=26.2\text{K}$  for  $\text{HoMnO}_3$ , it was possible to satisfactorily describe the angular dependences of the linewidth. For angular dependencies of the ESR linewidth in  $\text{YMnO}_3$  single crystal, we used different values of the exchange integral since the contents of the yttrium are much higher and in reality the image has a composition  $\text{YMn}_{0.75}\text{O}_3$ , then the valence of manganese is  $4+$ . In this case, for best description of ESR linewidth in  $\text{YMnO}_3$  we

## LECTURE NOTES

used the ratio  $S(S+1)D^2/J=0.96(K)$ , but it is not equal the value from theory estimation  $S(S+1)D^2/J=3.24(K)$ .

In conclusion, we have been investigated three hexagonal  $YbMnO_3$ ,  $HoMnO_3$  and  $YMnO_3$  with a different ratio between ions of rare earth and manganese by ESR method. It was found that in ytterbium manganite, ytterbium-deficient regions are observed where ferromagnetic nanostructures are formed. As a result, the complex temperature dependence of the linewidth is observed, if the temperature is increased, the linewidth is decreased, passes through a minimum, and then is grown. It is found that two lines are observed in the ESR spectrum of the  $HoMnO_3$  crystal. One is from ferromagnetic clusters, the second is from an exchange-related spin system.

It is found that one line is observed in the ESR spectrum of the  $YMnO_3$  crystal. One is from an exchange-related spin system. From the analysis of the angular dependence of the width of the EPR line, a relationship between the parameters of the Dzyaloshinsky-Moriya interaction and isotropic Heisenberg exchange is determined in  $YMnO_3$ :  $S(S+1)D^2/J=0.96(K)$ .

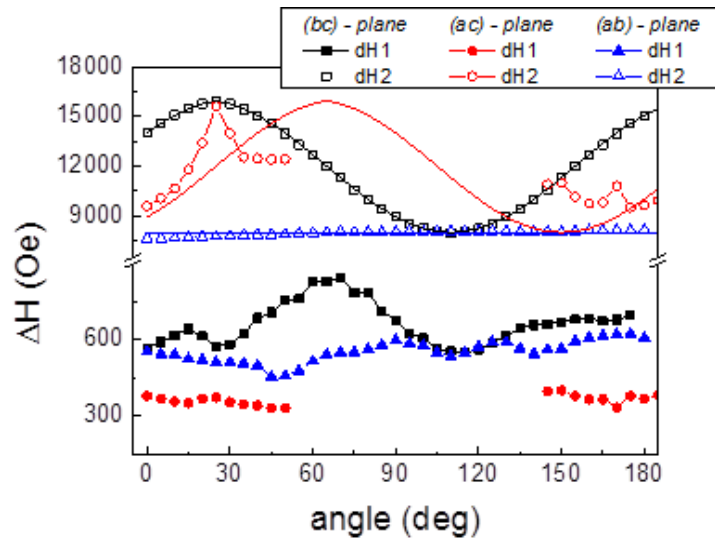


**Figure 3.** Angular dependencies of ESR linewidth at 300K in  $HoMnO_3$ .

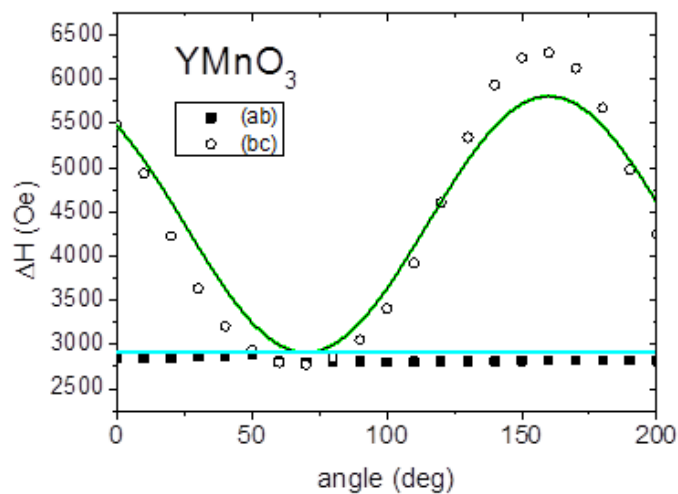


**Figure 4.** Angular dependencies of ESR linewidth at 300K in  $YMnO_3$ .  $S(S+1)D^2/J=0.96(K)$

## LECTURE NOTES

### References

- [1] Shannon, R. D. (1976) *Acta Cryst. A* 32(5) 751-767.
- [2] Wang, Y.T., et al (2013) *Adv. Condens. Matter Phys.* 2013 1-13.
- [3] Zhou, J.-S., et al (2006) *Phys. Rev. B* 74(1) 014422.
- [4] Dagotto, E., et al (2001) *Physics Reports.* 344 1-153.
- [5] S. Petit, S., et al (2007) *Phys. Rev. Lett.* 99, 266604.
- [6] Junghwan Park, J. et al (2003) *Phys.Rev.B* 68, 104426
- [7] Gellé, A., et al (2009) *EPL* 88, 37003.
- [8] Vajk, O. P. et al (2005) *Phys. Rev. Lett.* 94, 087601 (2005).
- [9] P.J. Janhavi, P.J., et al (2004) *J. Magn. Reson* 168(2) 284–287  
Deisenhofer, J., et al (2002) *Phys. Rev. B* 65(10) 104440.
- [10] Yatsyk, I.V. et al (2012) *JETP Lett.* 96(6) 416-420.
- [11] Eremina, R.M., et al (2016) *Appl. Magn. Reson.* 47(8) 869-879.
- [12] Raikher, Yu. L., et al (1994) *Phys. Rev. B.* 50 6250 – 6259.
- [13] Raikher, Yu. L., et al (1992) *Sov. Phys. JETP* 75 764-771.
- [14] Eremina, R.M., et al (2013) *JETP Letters* 98 848-852.
- [15] Eremina, R.M., (2014) *Magnetic Resonance in Solids* 16 14102.

**The study of  $\text{ReF}_3$  Nanoparticles by NMR**

Alakshin E.M.<sup>1</sup>, Kondratyeva E.I.<sup>1</sup>, Kuzmin V.V.<sup>1</sup>, Safiullin K.R.<sup>1,2</sup>, Stanislavovas A.A.<sup>1</sup>,  
Savinkov A.V.<sup>1</sup>, Klochkov, A.V.<sup>1</sup>, Tagirov, M.S.<sup>1,2</sup>

<sup>1</sup> Kazan Federal University, 420008, Kazan, Russian Federation,

<sup>2</sup> Institute of Applied Research, 420111, TAS, Kazan, Russian Federation

e-mail: alakshin@gmail.com

It is known that, when passing from a bulk material to nanoparticles, the parameters change significantly and new unique properties may arise. The synthesis and investigation of rare-earth trifluorides nanocrystals attract a great interest due to the unique magnetic, electric, and optical properties of these objects. Many techniques for nanoparticles synthesis (mechanosynthesis, detonation synthesis, electric explosion, plasmachemical synthesis, self propagating high temperature synthesis, vaporphase synthesis, thermal decomposition and recovery, deposition from colloidal solutions, etc.) and the change of their structure has been approved.

The methods of nanosized samples was approved The size distributions of particles and the X-ray diffraction spectra were also reported. Water clusters were found in  $\text{PrF}_3$  nanosamples, and their size was determined by nuclear magnetic resonance (NMR) cryoporometry and highresolution transmission microscopy. A nuclear pseudoquadrupole resonance of  $^{141}\text{Pr}$  was observed for the first time, the parameters of the nuclear spin Hamiltonian were determined, and the parameters of the crystal electric field in nanocrystals and microcrystals were found to differ significantly. The spin kinetics of adsorbed and liquid  $^3\text{He}$  in contact with crystalline nanopowders of Van Vleck paramagnet  $\text{PrF}_3$  was studied by NMR methods at 1.5 K. The parameters of nuclear magnetic relaxation of  $^3\text{He}$  were found to correlate with the particle sizes. A qualitative model of magnetic relaxation of  $^3\text{He}$  was proposed to describe the experimental data.

The magnetic phase transition in  $\text{DyF}_3$  is accompanied by a considerable change in the character of fluctuations of the magnetic moments of dysprosium ions, which affect the spin kinetics of  $^3\text{He}$  in contact with the substrate.

This work was supported by the Russian Foundation for Basic Research, project no. 16-32-60155 mol\_a\_dk.

## Investigation of nature of self organization of nanosystems by magnetic resonance

S.B. Orlinskii

Kazan Federal University, 420008 Kazan, Russia

Herein, we present the results of investigation of two different self organization of nanosystems, as native asphaltene self-assembly and sintered clusters of detonation nanodiamond by magnetic resonance.

The majority of vanadium and nickel compounds are present in heavy petroleum as porphyrins and located in asphaltenes. In general, petroleum porphyrins exist in homologous manifolds of several structural classes and can manifest great structural diversity. A series of papers nowadays is devoted to the determination of various vanadyl porphyrins (VP), to application of state-of-the-art mass-spectroscopic techniques for that purpose as well as to the development of different pathways of the effective vanadyl extraction. Dickie and Yen were the first to suggest that, having many of the same interactive groups as asphaltenes, petroporphyrins could also play a role in asphaltene self-assembly, adsorption, and phase separation. It is common knowledge that intermolecular interactions, such as hydrogen bonding, dipole–dipole interactions,  $\pi$ – $\pi$  stacking etc. in asphaltenes lead to aggregation into nanoaggregates in the bulk oil phase and the formation of elastic films at organic–aqueous interfaces although the basic asphaltene structure and mechanism of aggregation continue to be debated. The relationship between petroporphyrins and asphaltenes is largely unexplored .

While the EPR spectra either in X- or W-band do not reveal the changes caused by adsorption of oil asphaltenes on the surface of  $\gamma$ -alimina, a perceptible difference in  $^1\text{H}$  ENDOR spectra and appearance of  $^{27}\text{Al}$  ENDOR spectra are obtained. High-frequency EPR/ENDOR allows to resolve the anisotropy of the magnetic properties of stable vanadyl complexes being a part of asphaltenes and, therefore, is orientation selective for the space structure of VP complexes.

We present the first results of observation of enormously high concentrations of NV – ensembles created directly by a high-pressure high-temperature (HPHT) sintering procedure of detonation nanodiamond (DND) particles, which were produced through the detonation of strong explosives and have a size of 4–5 nm. We examine the properties of sintered DND clusters by using electron spin-echo (ESE) detected electron paramagnetic resonance (EPR) spectroscopy, photoluminescence, and high-frequency optically detected magnetic resonance (ODMR) spectroscopy. Based on the measurements performed we provide a rough estimation of the concentration of the NV centers in sintered DND clusters. Extremely high concentrations up to  $10^4$  ppm (1%) of NV – centers were observed in sintered clusters of DND, which allow one to fabricate structures with one NV – center per  $\text{nm}^3$ . The results presented are opening new perspectives in the unique NV – -containing diamond fabrication, thus allowing further development and investigations of the systems with one NV – center per nanometer after milling.

It appears that application of double resonance techniques, especially at high frequencies (high magnetic fields), could significantly improve the understanding of the mechanisms of the aggregation (complex formation, self-organization) of various oil constituents and other high-molecular disordered systems of biogenic and synthetic origins.

## Applications of NMR & NQR techniques for detection of energetic and dangerous materials

B.Z. Rameev<sup>1,2</sup>

<sup>1</sup> Gebze Technical University, Department of Physics, P.B. 141, Gebze-Kocaeli 41400, Turkey.

<sup>2</sup> E.K. Zavoisky Physical-Technical Institute, FRC Kazan Scientific Center of RAS, 420029, Kazan 420029, Russian Federation

e-mail: rameev@gtu.edu.tr

The detection of energetic (explosive) and dangerous substances is a very important security issue of modern society [1-4]. Energetic materials are solid, liquid or gaseous substances (or mixtures of these) which store a large amount of chemical energy that can be released in a very short time [5]. There are various classes of energetic materials, such as explosives, propellants, pyrotechnics, fuels and some others. As regards the dangerous (hazardous) materials, this category is even broader than energetic materials, and usually they are divided for nine main classes: explosives, gases, flammable & combustible liquids, flammable solids, oxidizing substances (& organic peroxides), toxic & infectious substances, radioactive materials, and corrosives [6,7].

The problem of detection of energetic materials is directly connected with issue of finding remains of explosives after the wars and local conflicts. Another important problem is detection of dangerous materials (explosives, flammables, toxic and highly reactive materials) which can be used by various terroristic groups over the world. Especially a problem of detection of various improvised explosive devices (IEDs), manufactured from homemade explosive materials (HME), has an enormous importance for life safety of civilians. In the aviation and other transport lines as well as for providing the security of public places, there is a problem of non-invasive detection of the explosive/dangerous substances in the baggage, suits, cars, under people clothes and others.

Available techniques for detection of energetic and dangerous substances can be divided on the two large group of *bulk* and *trace* explosive detection methods. Although many techniques of trace detection have proven their high effectiveness (such as dogs, ion mobility / mass / Raman / LIBS/ terahertz spectrometry, etc.), their solely use is unlikely to warrant the reliable explosive detection in the most of practical situations. On the other hand, in spite of the availability of various devices for bulk detection, currently there is NO a cost-effective commercial solution for broad use in airport checkpoint, mass-transport exits, parcel scanners, mine detection devices, etc. For most of bulk detection techniques, available nowadays, there are a number of problems to be resolved before their practical use. It is also obvious that an effective device *should combine a few methods*, including at least one bulk detection technique to increase reliability of the explosive detection and provide a minimal false alarm rate. Therefore, all bulk detection methods, especially X-ray/neutron/gamma/THz detection techniques and NMR/NQR detection, are extensively studied nowadays.

Minimum number of false alarms would be expected to be provided by the techniques, which are directed to detect neither the metal / plastic encloses or fuses but a material itself. In other words, the chemically specific identification of dangerous materials is expected. Such possibility is provided by spectroscopic techniques. Fortunately, in the case of the explosive substances, only a few explosive types are frequently used although there are hundreds of them. Among various spectroscopic techniques nuclear quadrupole resonance (NQR) and

## LECTURE NOTES

low-field nuclear magnetic resonance (NMR) are considered as very promising bulk explosives detection methods, based on the chemical identification of content.

The NQR frequency spectrum can be considered as a “fingerprint” of a specific chemical compound. Therefore, NQR is very promising methods for the detection of explosive and other compounds, which contain quadrupole nuclei in their structure [8,9]. It is well known that most of energetic and explosive solid materials include the  $^{14}\text{N}$  nitrogen nuclei. The main issues in the  $^{14}\text{N}$  NQR detection of explosives are the followings: a low Signal-to-Noise Ratio (SNR) especially for some of explosives with low-frequency NQR lines; influence of spurious signals due to resonant magneto-acoustic and piezoelectric ringing; and radio-frequency interference signals. The most fundamental issue, that hinders a practical use of NQR technique for the detection of explosives, is a very weak  $^{14}\text{N}$  signal [1]. Various methods have been proposed to increase the sensitivity which are the multipulse NQR [10], the double NQR-NMR technique [11], cross-polarization [12-15], double NQR-NQR methods [16, 17], use of superconducting quantum interference devices (SQUIDs) [18, 19] and giant magnetoresistance (GMR) sensors [20].

In our work on NQR detection the most interesting results have been received using the cross-relaxation enhanced NQR and multifrequency NQR approaches. We have shown that multifrequency (two/three) NQR technique allows filtering spurious signal after radiofrequency pulses and increases the sensitivity of NQR detection of RDX and other substances [16, 21-25, 26]. It has been also demonstrated that the cross-relaxation-enhanced NQR in low magnetic fields can be successfully applied to shorten the effective spin-lattice relaxation time, that is to increase the SNR of the AN detection [27].

Each technique has own limitations. NQR technique can be used for the detection of nitrogen-based solid-state explosives, but it useless in the case of liquid substances. However, liquids can be successfully detected by NMR technique. Considering restriction on application of high magnetic fields to scan the luggage and people, only time-domain NMR in low or moderate magnetic fields (with frequencies of few tens of MHz at most) can be applied. In this case, however we have to discriminate between various liquids by the relaxation and diffusion parameters of  $^1\text{H}$  signal which is not trivial task either. First successful applications of NMR method for detection of liquid explosives had been demonstrated as early as in 90<sup>th</sup> years of XX century [28-31]. For liquid explosive detection, most researchers consider so-called time-domain NMR as a prospective technique. In the time-domain NMR (TD-NMR), the spectroscopic information (i.e. resonance frequencies) of the scanned material is neglected. It is NMR in moderate or low magnetic field ( $\leq 1\text{T}$ ) which is based on measurements of spin-lattice and spin-spin relaxation parameters ( $T_1$  and  $T_2$ ) of the proton nuclei. In this case, the parameters, which are important for a specific application, should be taken into consideration. In the case of so-called bottle scanners, there is no task to localize a potential threat; therefore, we can apply much larger magnetic field to analyze the content of a bottle with liquid. Specialized NMR analyzers of the liquid content of bottles have been demonstrated by Quantum Magnetics [10], *Bruker Inc.*[32] and *T<sub>2</sub> Biosystems* [33, 34]. It should be noted that in principle the time-domain NMR can be done in as low magnetic field as Earth's field NMR. Recent progress in experimental techniques allows wider range of applications of Earth's magnetic field NMR [35]. In our recent works, an application of this technique for the liquid identification in plastic bottles and metal cans have been demonstrated (see Ref. [36] and Ref.[37], respectively).

In many studies, the conclusion has been made that the TD-NMR is an effective non-invasive, non-contact method to detect content of concealed liquids. Analysis of literature, as well as our recent studies (see Refs. [38, 39]), however, shows that for reliable discrimination

## LECTURE NOTES

between a large number of liquids, the scanning device has to involve some additional parameters. They could be NMR ones (not only  $T_2$  and  $T_1$  relaxation times probed by standard TD-NMR, but also the proton density, diffusion constant [40] and even spectral information if possible).

We have mentioned that most of energetic/explosive solid materials include the nitrogen nuclei of  $^{14}\text{N}$ . Surprisingly, the situation is somewhat similar in the case of liquids: a great number of energetic liquid substances contain nitrogen in their structure (see, for instance, the list of the common nitrogen-containing energetic liquids in the patent [21]). For this reason, the detection of  $^{14}\text{N}$  NMR signal as an extra parameter for determination of dangerous substances has been proposed by P. Prado *et al.* [41, 42]. It should be noted that the NMR nitrogen detection of energetic substances is not easy task because of specific feature of  $^{14}\text{N}$  NMR technique: its relative sensitivity of is only about 0.018 of the sensitivity of  $^1\text{H}$  NMR (i.e. the nitrogen NMR signal has a very small SNR). It is related to rather small gyromagnetic ratio of  $^{14}\text{N}$  nuclei comparing with  $^1\text{H}$  nuclei. On the other hand, a total number of both nitrogen-containing benign liquids and dangerous/explosive liquids, which does not contain nitrogen, are rather limited. Furthermore, the amount of nitrogen compounds in soft drinks and liquids for safety is negligible. Therefore, the use of  $^{14}\text{N}$  NMR to detect illicit liquids has a very important advantage, barely the fact of detection of  $^{14}\text{N}$  NMR signal from an inspected container gives a security alarm. Thus, the potential prospects of  $^{14}\text{N}$  NMR relaxometry for fast detection of explosives are very high [43].

Another approach is to use techniques, which are totally different from NMR, e.g. dielectric spectroscopy which can measure the dielectric constant and the loss tangent of liquids in the broad range of frequencies up to a few THz [44]. From this point of view, the microwave (MW, frequency range 1-100 GHz) or sub-THz spectroscopy looks very promising to be combined with the time-domain NMR in a single detection device for reliable identification of liquids. In this method, liquid substances are usually irradiated by electromagnetic waves in the range from 1 GHz to 0.3 THz to obtain  $\epsilon'$  and  $\epsilon''$  dielectric constants (or relative permittivity).

Over past few years THz and sub-THz technologies have attracted an essential attention of researchers (see, e.g. [45-47]). The main interest was initially concentrated on the broadband spectroscopic techniques because spectral signatures of various explosives were expected to provide a new and very powerful technique for standoff (distant) detection of explosive, chemical or biological warfare agents and other threat materials. Despite of enthusiasm and very high expectation of the first years of exploration, currently only a few successful implementation of THz technology as model setups to demonstrate feasibility of this technology are known. A real-time in-the-field identification for security applications meets several technical challenges, such a very limited penetration depth, limited bandwidth due to attenuation in ambient conditions, noise floor /scattering losses, etc [25]. For that reason, most of successful applications have been concentrated on the THz imaging systems, which are aimed to detect hidden objects under wear [26, 27]. However, there is a very simple and powerful way to exploit the MW and sub-THz technique in the liquid verification devices, such as a dielectric spectroscopy. This technique provide the values of permittivity constant in the range (or at least at some properly chosen characteristic) frequencies. Furthermore, this technique could be applied in combination with time-domain NMR to obtain better discrimination between benign and threat liquids especially for the case of very large group of liquids (i.e. in the situation that usually met in air-check points). The dielectric function of liquids in the frequency range from nearly 1 GHz up to one THz may serve as a fingerprint signature of a specific liquid at a given temperature. Fortunately, the differences in

reflectance values for the most of pure liquids (excepting water and hydrogen peroxide) are relatively high.

### *Acknowledgement*

This work is supported by NATO Science for Peace and Security Programme, NATO SPS project No. 985005 (G5005). Authors also acknowledge a partial support by East Marmara Development Agency (MARKA, project No. TR42/16/ÜRETİM/0013) and by Research Fund of Gebze Technical University (grants No. BAP 2017-A-105-44).

### **References**

- [1] Miller J.B., Barrall G.A., “Explosives Detection with Nuclear Quadrupole Resonance”, American scientist, Vol. 93 (1), 50 (2005).
- [2] Explosives Detection using Magnetic and Nuclear Resonance Techniques, NATO Science for Peace and Security Series B: Physics and Biophysics. Eds: J.Fraissard, O. Lapina, Springer, 2009.
- [3] B.Z.Rameev, G.V.Mozzhukhin, B. Aktas, Magnetic Resonance Detection of Explosives and Illicit Materials, Applied Magnetic resonance, Volume 43, Issue 4 (2012), Page 463-467. DOI 10.1007/s00723-012-0423-9.
- [4] Explosives Detection using Magnetic and Nuclear Resonance Techniques. Series: NATO Science for Peace and Security Series. Eds: Tomaz Apih, Bulat Rameev, Georgy Mozhukhin, and Jamie Barras Springer, 2014.
- [5] URL: [https://en.wikipedia.org/wiki/Energetic\\_material](https://en.wikipedia.org/wiki/Energetic_material)
- [6] URL: <http://www.unece.org/fileadmin/DAM/trans/danger/publi/unrec/English/Part2.pdf>
- [7] URL: <https://pubchem.ncbi.nlm.nih.gov/search/>
- [8] J. A. S. Smith, “Nitrogen-14 Quadrupole Resonance Detection of RDX and HMX Based Explosives”, European Convention on Security and Detection, vol. 408, pp. 288–292 (1995).
- [9] Allen N. Garroway, Michael L. Buess, Joel B. Miller, Bryan H. Suits, Andrew D. Hibbs, Geoffrey A. Barrall, Robert Matthews, and Lowell J. Burnett., “Remote Sensing by Nuclear Quadrupole Resonance”, IEEE Transactions on Geoscience and Remote Sensing, Vol. 39, No. 6, 1108-1118 (2001) .
- [10] R.A. Marino, S.M. Klainer, “Multiple spin echoes in pure quadrupole resonance” J. Chem. Phys. 67, 3388-3389 (1977).
- [11] R. Blinc, T. Apih, and J. Seliger, “Nuclear Quadrupole Double Resonance Techniques for the Detection of Explosives and Drugs”, Appl. Magn. Reson. 25, 523-534 (2004).
- [12] G.V.Mozjoukhine: The two-frequency Nuclear Quadrupole Resonance for explosives detection. Appl. Magn. Reson. 18, 527-535 (2000).
- [13] T.N. Rudakov, P.A. Hayes, ”Cross-polarisation method for improvement of 14N NQR signal detectability”, Journal of Magnetic Resonance 183, 96-101 (2006)
- [14] Thurber, K.R., Sauer, K.L., Buess, M.L., Klug, C.A., Miller, J.B., “Increasing 14N NQR signal by 1H–14N level crossing with small magnetic fields”, Journal of Magnetic Resonance, 177 (1), 118 (2005).
- [15] J.Lužnik, J.Pirnat, V.Jazbinšek, T.Apih, A.Gregorovič, R.Blinc, J.Seliger, Z.Trontelj.,” Polarization enhanced “single shot” 14N nuclear quadrupole resonance detection of trinitrotoluene at room temperature”, Appl.Phys.Lett.89, 123509 (2006).
- [16] G.V. Mozhukhin, B.Z. Rameev, N. Doğan, B. Aktaş, “The Two-Frequency Multipulse Sequence in Nuclear Quadrupole Resonance of N-14 Nuclei”; [Explosives Detection using Magnetic and Nuclear Resonance Techniques. Series: NATO Science for Peace and Security Series. Subseries: NATO Science for Peace and Security Series B: Physics and Biophysics.] ed. By J.Fraissard, O. Lapina, Springer, 205-230 (2009)

## LECTURE NOTES

- [17] K.L.Sauer, B.H.Suits, A.N.Garroway, J.B.Miller, "Secondary echo in three –frequency nuclear quadrupole resonance of spin-1 nuclei", *J. Chem. Phys.* 118, 5071-5081 (2003).
- [18] M. P. Augustine, D. M. TonThat, J. Clarke. SQUID detected NMR and NQR. *Solid State Nuclear Magnetic Resonance* 11, 139–156(1998).
- [19] J.P.Yesinowski,M.L.Buess et al. Detection of  $^{14}\text{N}$  and  $^{35}\text{Cl}$  in cocaine base and hydrochloride using NQR,NMR and SQUID techniques. *Analytical Chem.*,Vol.67, No.13, 1995, 2256-2263.
- [20] M.Pannetier-Lecoer, C.Fermon, H.Dyvorne, G,Cannies and G.Le Goff, "14N NQR Detection of Explosives with Hybrid Sensors", [Explosives Detection using Magnetic and Nuclear Resonance Techniques. Series: NATO Science for Peace and Security Series. Subseries: NATO Science for Peace and Security Series B: Physics and Biophysics.] ed. By J.Fraissard, O. Lapina, Springer, 31-40 (2009).
- [21] G.V. Mozzhukhin, B.Z. Rameev, N. Doğan, B. Aktaş, Secondary signals in two frequency nuclear quadrupole resonance on  $^{14}\text{N}$  nuclei with  $I=1$ , *J. Magn. Reson.* 193 (1), pp. 49-53 (2008).
- [22] N. Doğan, R. Topkaya, H. Subaşı, Y. Yerli, B. Rameev. Development of Halbach magnet for portable NMR device, *J. Physics: Conference Series*, 153 (2009) 012047.
- [23] G.V.Mozzhukhin, B.Z.Rameev, N.Dogan,B. Aktas. The application of the two frequency composite pulses for NQR detection of nitrogen-based compounds. *J Supercond & Nov Magn* (2011) 24: 653–658.
- [24] G.V.Mozzhukhin, B.Z.Rameev, R.R.Khusnutdinov, N.Doğan, B. Aktaş, Three-frequency composite multipulse nuclear quadrupole resonance (NQR) technique for explosive detection, *Appl. Magn. Reson.* 43 ( 2012), 547-556; DOI 10.1007/s00723-012-0326-9
- [25] B. Rameev, G.V. Mozzhukhin, B. Aktaş (Eds.), Special Issue on Magnetic Resonance Detection of Explosives and Illicit Materials, *Appl. Magn. Reson.* 43 (2012) 463–467; DOI 10.1007/s00723-012-0423-9.
- [26] G. V. Mozzhukhin, J. Barras, G. Kupriyanova, B. Rameev, Two-Frequency Nuclear Quadrupole Resonance for Line Identification. *Appl. Magn. Reson.* 46(2) (2015) 161–179; DOI: 10.1007/s00723-014-0625-4
- [27] G. V. Mozzhukhin, J. Barras, G. Kupriyanova, B. Rameev, Two-Frequency Nuclear Quadrupole Resonance for Line Identification. *Appl. Magn. Reson.* 46(2) (2015) 161–179; DOI: 10.1007/s00723-014-0625-4
- [28] Burnett L.J., *Liquid Explosives Detection*, Proceedings of the SPIE 2092, 208-217(1993).
- [29] Kumar S, McMichael W C, Kim Y-W, Sheldon A, Magnuson E E, Ficke L, Chhoa T K - L, Moeller C R, Barrall G A, Burnett L J, Czipott P V, Pence J S and Skvoretz D C, Proceedings of the SPIE, 2934, 126-137(1997).
- [30] Kumar S., McMichael W.C, Kim Y.-W., Sheldon A., Magnuson E.E, Ficke L., Chhoa TK-L., Moeller C.R, Barrall G.A, Burnett L.J, Czipott P.V, Pence J.S and Skvoretz D.C, "Screening sealed bottles for liquid explosives", *Proc. SPIE* 2934, 126–137 (1997).
- [31] Kumar S., "Liquid-Content Verification for Explosives, Other hazards, and Contrabands by Magnetic Resonance", *Appl. Magn. Reson.* 25, 585-597 (2004).
- [32] Mauler J., Danieli E., Casanova F., Blumich B., "Identification of liquids encountered in carr-on-luggage by mobile nmr", [Explosives Detection using Magnetic and Nuclear Resonance Techniques, NATO Science for Peace and Security Series B: Physics and Biophysics.] ed. By J.Fraissard, O. Lapina, Springer, 193-203 (2009).
- [33] Kumar S., Prado P.J., "Detection of concealed liquid explosives and illicit drugs in unopened bottles", [Explosives Detection using Magnetic and Nuclear Resonance Techniques, NATO Science for Peace and Security Series B: Physics and Biophysics]. ed. By J.Fraissard, O. Lapina, Springer, ,73-79(2009)

- [34] Pablo J. Prado, Igor Mastikhin and Mats T. Karlsson, Rapid Method to Screen Unopened Bottles to Detect Concealed Drugs , *Applied Magnetic Resonance*, 2012, DOI: 10.1007/s00723-012-0325-x
- [35] Mohoric A., Stepišnik J., *Progress in Nuclear Magnetic Resonance Spectroscopy*, 54, 166–182(2009).
- [36] H. Sato-Akaba, H. Itozaki, Development of the Earth's Field NMR Spectrometer for Liquid Screening, *Appl. Magn. Res.* 43(4), 579-589 (2012), DOI: 10.1007/s00723-012-0346-5
- [37] E. Balcı, B. Rameev , H Acar, G.V. Mozzhukhin, B. Aktaş, B. Çolak, P.A. Kupriyanov, A.V. Ievlev, Y.S. Chernyshev, V.I. Chizhik. Development of Earth's Field Nuclear Magnetic Resonance (EFNMR) Technique for Applications in Security Scanning Devices. *Appl. Magn. Reson.* 47(1) (2016) 87-99 (DOI: 10.1007/s00723-015-0730-z )
- [38] B.Z. Rameev, G.V. Mozzhukhin, R.R. Khusnutdinov, B. Aktas, A.B.Konov, D.D.Gabidullin, N.A. Krylatyh, Y.V. Fattakhov, K.M.Salikhov. Novel approaches in nuclear magnetic/ quadrupole resonance techniques for explosives detection. *Proc. SPIE 8357, Detection and Sensing of Mines, Explosive Objects, and Obscured Targets XVII*, 83570Z (1 May 2012); DOI: 10.1117/12.923625.
- [39] A.B. Konov, K.M. Salikhov, E.L. Vavilova, B.Z. Rameev, Multiparameter NMR Identification of Liquid Substances, In: *Magnetic Resonance Detection of Explosives and Illicit Materials* (Eds: T. Apih, B.Rameev, G.Mozzhukhin, J. Barras), NATO Science for Peace and Security Series B: Physics and Biophysics, Springer, 2014, pp.111-122.
- [40] Gradišek A., Apih T., “NMR-Based Liquid Explosives Detector”, *Appl. Magn. Reson.* 38 (4), 485-493 (2010).
- [41] P. Prado, Detecting Hazardous materials in containers utilizing nuclear magnetic resonance based measurements. Patent US 2014/0225614 A1, Aug.14, 2014.
- [42] P. Prado, Botled Liquid Scanner for Security Checkpoints, in NATO book “Magnetic Resonance Detection of Explosives and Illicit Materials”, NATO Science for Peace and Security Series - B: Physics and Biophysics, Eds: Tomaz Apih, Bulat Rameev, Georgy Mozzhukhin, and Jamie Barras Springer (2013) 89-98.
- [43] D. McAteer, J. Akhavan, Nitrogen-14 NMR Spectroscopic Detection of Explosophores in Solution, *Propellants, Explosives, Pyrotechnics* 41(2) (2016) 367-370.
- [44] Y. Divin, M. Lyatti, U. Poppe, K. Urban, Identification of liquids by high-Tc Josephson THz detectors, *Physics Procedia* 36 (2012) 29-34.
- [45] B.M.Fischer, THz imaging for fast detection of hidden threats, 2nd EU Conference on Detection Explosives (2nd EUCDE), Rome, Italy, 13-15 March, 2013. Presentation OP20 (Programme & Abstract Book, p.46).
- [46] J.F. Federici, B. Schulkin, F. Huang, D. Gary, R. Barat, F. Oliveira and D. Zimdars, THz imaging and sensing for security applications—explosives, weapons and drugs, *Semicond. Sci. Technol.* 20 (2005) S266–S280 doi:10.1088/0268-1242/20/7/018.
- [47] A.A.Vertiy, S. Ozbek, A.V. Pavlyuchenko, M. Tekbas, A. Kizilhan, H. Çetinkaya, A. Unal, S.B. Panin, Proceedings of IEEE International Symposium on Antennas and Propagation (APSURSI), 3-8 July 2011, p. 2111-2114.
- [48] G.V. Mozzhukhin, B.Z. Rameev, G.S. Kupriyanova, and Bekir Aktaş, Cross-Relaxation Enhanced NQR of Ammonium Nitrate in Low Magnetic Field, In: *Magnetic Resonance Detection of Explosives and Illicit Materials* (Eds: T. Apih, B.Rameev, G.Mozzhukhin, J. Barras), NATO Science for Peace and Security Series B: Physics and Biophysics, Springer, 2014, pp.45-59.

## Dynamic nuclear polarization in silicon at ultra-low temperatures

S. Vasiliev

Wihuri Physical Laboratory, Department of Physics and Astronomy, University of Turku,  
20014 Turku, Finland

I shall report on a series of experiments on dynamic nuclear polarization (DNP) in P and As doped silicon. The study is performed in a strong 4.6 T magnetic field and temperatures down to 0.1 K, when the donor electron spins are fully polarized and the relaxation times of electrons and nuclei are very long.

We performed DNP experiments with the donor nuclei as well as the  $^{29}\text{Si}$  nuclei of the host lattice, which for a normal isotope composition, are present with a 4.7% abundance. Two major DNP mechanisms: the Overhauser effect and the Solid effect appear to be very effective at our experimental conditions. We demonstrate that very high values of the donor nuclear polarization can be obtained using the Overhauser effect at extremely low values of RF power. The Solid effect can be utilized for a site selective polarization of  $^{29}\text{Si}$  nuclei. Finally, I shall explain how the DNP effects can be used for manipulation of the  $^{29}\text{Si}$  nuclear spins in a certain lattice sites near donors. The latter possibility makes them promising candidates for using as qubits for quantum computing.

## Magnons Bose-Einstein Condensation and Spin Superfluidity.

Yu.M. Bunkov

Kazan Federal University, 420008, Kremlevskaya st.18, Kazan, Russia

The superfluid current of spins – spin supercurrent – is one more representative of superfluid currents, such as superfluid mass current in superfluids  $^4\text{He}$ ; superfluid current of electric charge in superconductors; superfluid current of hypercharge in Standard Model of particle physics; superfluid baryonic current and current of chiral charge in quark matter; etc. The spin supercurrents emerge in the systems, where the symmetry under spin rotations is spontaneously broken. They carry spin without dissipation in the ordered magnets, such as solid ferro and antiferromagnets, and spin-triplet superfluid  $^3\text{He}$ . However, in 1984 the new state of matter has been discovered in antiferromagnetic superfluid  $^3\text{He}$  – the spontaneously self-organized phase-coherent precession of spins [1, 2]. This state has all the signatures of spin superfluidity, but it is radically different from the conventional ordered states in magnets. It is the quasi-equilibrium state, which emerges on the background of the ordered magnetic state, and which can be represented in terms of the Bose condensation of magnetic excitations – magnons [3]. The magnon BEC opened the new class of the systems, the Bose-Einstein condensates of quasiparticles and collective modes, whose number is not conserved. Representatives of this class in addition to BEC of magnons are the BEC of phonons, exciton-polaritons, photons, rotons and other possible bosonic modes. The life time of these condensates is finite, but can be very long, reaching minutes in antiferromagnetic superfluid  $^3\text{He-B}$ . Furthermore, the lifetime of BEC state may be infinite in the case, when loses (evaporation) of quasiparticles compensated by creation of a new quasiparticles.

The 30 years of magnons BEC investigations in different antiferromagnetic states of superfluid  $^3\text{He}$  well established the physics of excited magnon BEC and phenomenon of spin superfluidity. The review of these investigations one can find, for example in the book [4]. There are no any specific properties of antiferromagnetic superfluid states of  $^3\text{He}$ , which have advantage for magnon BEC formation in  $^3\text{He}$ , except the very small Gilbert damping factor of magnons, which can be as low as  $10^{-8}$ . Indeed it should be possible to find magnon BEC phenomena in other solid magnetics. In Kazan, there was successfully found the formation of magnon BEC in antiferromagnets with coupled nuclear-electron precession, like  $\text{MnCO}_3$  and  $\text{CsMnF}_3$  at 1.5K temperature by CW [5] and pulsed [6] NMR. The observation was done on quasinuclear branch of precession, which characterized by Gilbert damping factor of about  $10^{-5}$  and the repulsive interaction between magnons.

Recently, in Kazan Federal University, a breakthrough discovery was made. There was observed a conventional magnon BEC with  $k = 0$  in Yttrium Iron Garnet (YIG) film at room temperature.

YIG characterized by a very small Gilbert damping factor  $\alpha$  about  $10^{-5}$ , the one of the best value for solid magnetic materials. Owing the exceptionally long lifetime of magnetic excitations YIG is used in microwave and spintronic devices that can operate at room temperature. It makes YIG an ideal platform for the development of microwave magnetic technologies, which have already resulted in the creation of the magnon transistor and the first magnon logic gate. Significant interest has also developed in quantum aspects of magnon dynamics, using YIG as the basis for new solid-state quantum measurement and information processing technologies including cavity-based QED, optomagnonics, and optomechanics. That is why the formation of magnon BEC in YIG and observation of spin supercurrent, like in  $^3\text{He}$ , should leads to a development of new branch of physics - Supermagnonics.

## LECTURE NOTES

We have made a first observation of magnon BEC and spin supercurrent in a normally magnetized YIG film. In this conditions the minimum of energy corresponds to  $k = 0$  like in atomic BEC. Furthermore, the magnetic properties of YIG are in one to one corresponds to a properties of antiferromagnetic superfluid  $^3\text{He-A}$  in deformed aerogel, the system, where magnon BEC and spin superfluidity have been discovered early [7,8]. Our recent investigations of  $^3\text{He}$  in aerogel, give us an idea of experiments in YIG. We have found the experimental results, very similar to one from magnon BEC in  $^3\text{He -A}$ . This result will be described in the lecture.

This work was supported by the Russian Science Foundation, project no. 16-12-10359.

### References

- [1] Borovik-Romanov A. S., Bunkov Yu. M., Dmitriev, V.V., Mukharskii, Yu. M. Long-lived induction signal in superfluid  $^3\text{He-B}$ ". JETP Lett. 40, 1033-1037 (1984).
- [2] Fomin I. A. Long-lived induction signal and spatially nonuniform spin precession in  $^3\text{He-B}$ . JETP Lett. 40, 1037-1040 (1984).
- [3] Bunkov Yu. M., Volovik G. E. Bose-Einstein Condensation of Magnons in Superfluid  $^3\text{He}$ . J. of Low Temp. Phys. 150, 135-144 (2008).
- [4] Bunkov Yu. M., Volovik G. E. Spin Superfluidity and Magnon BEC. Novel Superfluids Ch.4, (eds. Bennemann, K. H. & Ketterson, J. B. Oxford Univ. Press, Oxford, 2004).
- [5] Bunkov, Yu. M. et al. High-Tc Spin Superfluidity in Antiferromagnets. Phys. Rev. Lett. 108, 177002 (2012).
- [6] Tagirov, M. S. et al. Magnon BEC in Antiferromagnets with Suhl-Nakamura Interaction. J. Low Temp. Phys. 175, 167-176 (2014).
- [7] Hunger, P., Bunkov, Yu. M., Collin, E. & Godfrin, H. Evidence for Magnon BEC in Superfluid  $^3\text{He-A}$ ". J. of Low Temp. Phys 158, 129134 (2010).
- [8] Sato, T. et al. Coherent Precession of Magnetization in the Superfluid  $^3\text{He A-Phase}$ . Phys. Rev. Lett. 101, 055301 (2008).

## **NMR in new superfluid phases of $^3\text{He}$**

V.V. Dmitriev

P.L.Kapitza Institute for Physical Problems RAS, Moscow, Russia

One of the examples of superfluid Fermi systems with unconventional Cooper pairing is superfluid  $^3\text{He}$  where the pairing occurs with spin and orbital angular momentum equal to 1. In isotropic space the free energy and the superfluid transition temperature are degenerate with respect to spin and orbital momentum projections. This allows a variety of superfluid phases with the same transition temperature, but in zero magnetic field only two phases (A and B) with the lowest energy are realized. The orbital degeneracy may be lifted by anisotropic impurities, e.g., by globally anisotropic aerogel in which strands are aligned on average along the same direction. Recent experiments show that in this case new superfluid phases of  $^3\text{He}$  (polar phase and polar-distorted A and B phases) can be realized. In the first half of the lecture, a brief introduction to superfluid  $^3\text{He}$  will be given. In the second half, the NMR properties of A, B and the new phases will be considered to demonstrate how these properties make it possible to identify all these superfluid states.

## Experimental vs GIAO calculated NMR spectra for [1,2]diazepino[4,5-*b*]indole derivatives

A.V. Muratov, Yu.V. Berestneva, E.V. Raksha, A.B. Eresko

L.M. Litvinenko Institute of Physical Organic and Coal Chemistry, 83114, Universitetskaya str., 24, Donetsk

e-mail: a\_eresko77@mail.ru

### Introduction

The benzodiazepinone scaffold is an extremely rewarding template for drug discovery. Biological activity of compounds bearing a 1-aryl-2,3-benzodiazepine skeleton is best demonstrated by tofisopam, a well-known anxiolytic drug from this family, or the former drug candidate talampanel [1, 2], that reached the human clinical development stage. Related fused heterocyclic systems, such as indolo[1,2]diazepines, can be regarded as potentially useful scaffolds for drug discovery. It is known that medium-sized indolo-fused azacycles constitute structural arrangements in many natural and synthetic bioactive compounds [3, 4]. But no considerable effort has been devoted to the synthesis of [1,2]diazepino[4,5-*b*]indoles as well as their reactivity and structural features. As a continuation of our research into the synthesis and reactivity of new heterocyclic systems having a diazepine ring linked to various heterocycles [5, 6], we report the results of synthesis as well as molecular modeling of structure and NMR shieldings for the new indolo-fused [1,2]diazepines.

### Results and discussions

The primary method of the formation of 1,2-diazepine ring annelated with heterocycle moiety is still a condensation of 1,5-dicarbonyl compounds with hydrazine [5-8]. Our planned approach to [1,2]diazepino[4,5-*b*]indoles **1-3** involved synthesis of the start diazepine **1** followed by its structural modification to afford derivatives **2** and **3** (Fig. 1).

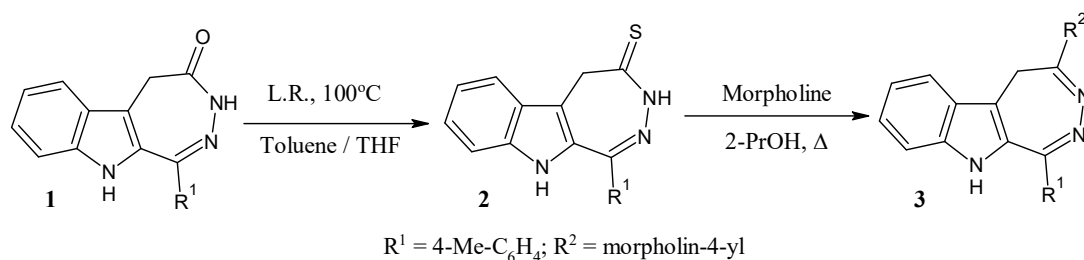


**Figure 1.** Scheme of the [1,2]diazepino[4,5-*b*]indoles synthesis

Starting [1,2]diazepino[4,5-*b*]indole **1** was obtained by cyclization of the ethyl [2-(4-methylbenzoyl)-1*H*-indol-3-yl]acetate with hydrazine hydrate in the presence of acetic acid as a catalyst. [1,2]diazepino[4,5-*b*]indole **1** was transformed into the corresponding thione **2** by reaction with Lawesson's reagent in heated toluene as described elsewhere [9, 10]. Diazepine-4-thione **2** reacted with an appropriate amount of morpholine by heating at reflux in propan-2-ol to yield compound **3**. Structures of the new compounds were determined by NMR spectroscopy.

A feature of the morpholine derivative **3** NMR <sup>1</sup>H spectra as compared to corresponded 1,2-diazepinon **1** and 1,2-diazepin-thion **2** is the appearing of the methylene group protons as two broadened signals with chemical shifts at 2.98 and 4.30 ppm (Table 1), that points out on

the non-planar structure of the diazepine ring. It is obvious that the presence of two bulk substituents in the diazepine core reduces its conformational mobility, so separate signals for the equatorial and axial protons of the methylene group are observed in NMR  $^1\text{H}$  spectra of the compound **3**.

**Table 1.** Calculated ( $\delta_{\text{calc}}$ , ppm) and experimental ( $\delta_{\text{exp}}$ , ppm) values of the  $^1\text{H}$  chemical shifts of [1,2]diazepino[4,5-*b*]indoles **1-3**

Atom	<b>1</b>			<b>2</b>			<b>3</b>		
	$\delta_{\text{calc}}$	$\delta_{\text{exp}}$	$\Delta\delta$	$\delta_{\text{calc}}$	$\delta_{\text{exp}}$	$\Delta\delta$	$\delta_{\text{calc}}$	$\delta_{\text{exp}}$	$\Delta\delta$
H1	7.883	7.65	0.233	7.922	7.73	0.192	7.887	7.7	0.187
H2	7.392	7.06	0.332	7.433	7.13	0.303	7.370	7.04	0.330
H3	7.493	7.18	0.313	7.567	7.26	0.307	7.461	7.17	0.291
H4	7.433	7.38	0.053	7.495	7.42	0.075	7.451	7.39	0.061
H5	7.685	11.08	3.394	7.745	11.41	3.664	7.743	11.16	3.417
H6	3.672	3.59	0.082	4.06	4.01	0.05	4.364	4.3	0.064
H7	3.675	3.59	0.085	4.06	4.01	0.05	2.364	2.98	0.615
H8	8.286	10.64	2.353	9.723	12.51	2.786	-	-	-
H9,10	7.800	7.64	0.16	7.837	7.66	0.177	7.878	7.7	0.178
H11,12	7.493	7.24	0.253	7.523	7.32	0.203	7.443	7.24	0.203
H13,14,15	2.364	2.42	0.056	2.390	2.44	0.05	2.338	2.43	0.092
H16-H19	-	-	-	-	-	-	3.476	3.38	0.096
H20-H23	-	-	-	-	-	-	3.755	3.61	0.145

Molecular geometry optimization was carried out for the studied [1,2]diazepino[4,5-*b*]indoles **1-3** by B3LYP/6-31G(d,p)/PCM method. Parameters of molecular geometry as well as electronic structure for the diazepine ring were estimated. Only conformers with the lowest total energies were considered for all studied 1,2-diazepine molecules. Structural models of the 1,2-diazepines **1-3** with atom labels used for further discussion of the chemical shifts calculations are listed on Fig 2. The seven-membered heterocycle is in boat conformation. Atoms C9 and C10 are coplanar to the indole plane: the C1-C3-C6-C9 and C5-N1-C8-C10 torsion angles are within 0.2 - 2.0° and 177.7 - 178.8°, respectively.

For the most stable conformers of the studied molecules  $^1\text{H}$  chemical shifts were estimated. The B3LYP/6-31G(d,p)/PCM optimized geometries were used for magnetic shielding tensors calculation by standard GIAO method. Concerning the spectral patterns of protons, inspection of calculated and experimental values (Table 1) reveals the following

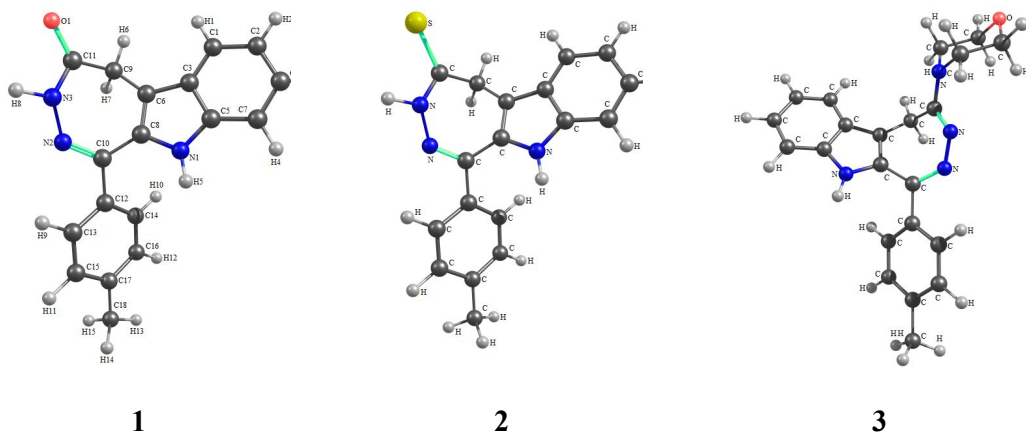


**Figure 2.** The equilibrium configurations of the [1,2]diazepino[4,5-*b*]indoles **1-3** (B3LYP/6-31G(d,p)/PCM method)

features. The patterns of  $^1\text{H}$  spectra for [1,2]diazepino[4,5-*b*]indoles are correctly reproduced at used computational level. A linear correlation between the theoretical and experimental proton chemical shifts is clearly visible in Fig. 3 (the signals from exchangeable NH protons were not considered).

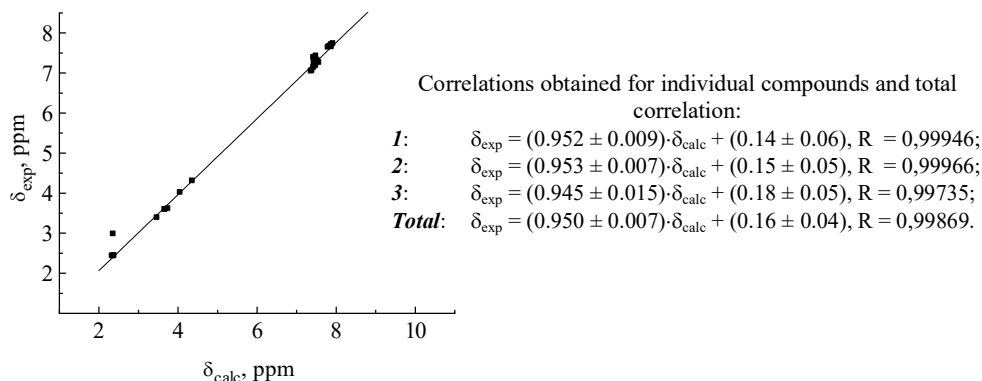


**Figure 3.** Total linear correlation between the theoretical and experimental proton chemical shifts of [1,2]diazepino[4,5-*b*]indoles **1-3**

Good quantitative agreement within 0.05 – 0.33 ppm between theoretical and experimental proton chemical shifts is observed for these compounds, which appears to be very satisfactory, taking into consideration the fact that the experimental chemical shifts in solution are subject to solvent, concentration and temperature effects.

### Experimental

$^1\text{H}$  NMR spectra were recorded on a Bruker Avance II 400 (400 MHz) in  $\text{DMSO-d}_6$  with TMS as an internal standard. The CHN elemental analysis was performed using a Fisons AE1108 analyzer, and the results were found to be in good agreement ( $\pm 0.25\%$ ) with the calculated values.

Initial molecular geometries of the [1,2]diazepino[4,5-*b*]indoles **1-3** were generated using the algorithm of complete inclusion of possible geometric and steric factors implemented in the Conformer plugin of the Marvin software package [11]. Molecular geometry and electronic structure parameters, thermodynamic characteristics of the [1,2]diazepino[4,5-*b*]indoles were calculated using the Gaussian 09 [12] software package. Geometric parameters, harmonic vibrational frequencies, and the vibrational contribution to the zero-point vibrational energy were determined after full geometry optimization in the framework of B3LYP/6-31G(d,p) density functional calculations. The solvent (DMSO) effect was considered in the PCM approximation. The magnetic shielding tensors ( $\chi$ , ppm) for  $^1\text{H}$  nuclei of the 1,2-diazepine derivatives were calculated with the B3LYP/6-31G(d,p) optimized geometries by standard GIAO (Gauge-Independent Atomic Orbital) approach [13]. The calculated magnetic isotropic shielding tensors,  $\chi_i$ , were transformed to chemical shifts relative to TMS,  $\delta_i$ , by  $\delta_i = \chi_{\text{ref}} - \chi_i$ , where both,  $\chi_{\text{ref}}$  and  $\chi_i$ , were taken from calculations at the same computational level.  $\chi$  Values for magnetically equivalent nuclei were averaged.

### Conclusions

Correlations between experimental chemical shifts and GIAO-calculated isotropic shielding constants of protons as obtained from new [1,2]diazepino[4,5-*b*]indoles were established in order to assess the performance of NMR spectral calculations. Linear

regressions  $\delta_{\text{calc}} = a\delta_{\text{exp}} + b$  yield standard deviations of 0.007 – 0.05 ppm for hydrogen atoms.

### References

- [1] Luszczyki, J. J. Third-generation antiepileptic drugs: mechanisms of action, pharmacokinetics and interactions. *Pharmacol. Rep.* 2009, 61, 197–216.
- [2] Iwamoto, F. M.; Kreisl, T. N.; Kim, L.; Duic, J. P.; Butman, J. A.; Albert, P. S.; Fine, H. A. Phase 2 trial of talampanel, a glutamate receptor inhibitor, for adults with recurrent malignant gliomas. *Cancer* 2010, 116, 1776–1782.
- [3] Sundberg, R. J. *Indoles*; Academic: New York NY, 1996.
- [4] Somei, M.; Yamada, F. Simple indole alkaloids and those with a non-rearranged monoterpenoid unit. *Nat. Prod. Rep.* 2005, 22, 73-103.
- [5] Tolkunov, V. S.; Eresko, A. B.; Khizhan, A. I.; Shishkin, O. V.; Palamarchuk, G. V.; Tolkunov, S. V. Heterocyclization of 2-acyl-3-indolylacetic acids using hydrazine. Synthesis of 2,3-dihydro-2-oxo-5-R1-1H-[1,2]diazepino[4,5-b]indoles. *Chem. Heterocycl. Comp.* 2009, 45, 726-734.
- [6] Eresko, A. B.; Tolkunov, V. S.; Tolkunov, S. V. Condensed diazepines. Synthesis of 1-aryl-3,5-dihydro-4H-1-benzofuro-[2,3-d][1,2]diazepin-4-ones. *Chem. Heterocycl. Comp.* 2010, 46, 1127-1132.
- [7] Wang, J.; Wang, L.; Guo, Sh.; Zha, Sh.; Zhu J. Synthesis of 2,3-Benzodiazepines via Rh(III)-Catalyzed C–H Functionalization of N-Boc Hydrazones with Diazoketoesters. *Org. Lett.* 2017, 19, 3640-3643.
- [8] Espahbodinia, M.; Ettari, R.; Wen, W.; Wu, A.; Shen, Yu-Ch.; Niu, Li; Grasso, S.; Zappalà M. Development of novel N-3-bromoisoxazolin-5-yl substituted 2,3-benzodiazepines as noncompetitive AMPAR antagonists. *Bioorg. Med. Chem.* 2017, 25, 3631–3637.
- [9] Cava, M.P.; Levinson, M.I. Thionation reactions of lawesson's reagents. *Tetrahedron* 1985, 41, 5061-5087.
- [10] Eresko, A.; Tolkunov, V.; Tolkunov, S. Simple and efficient preparation of 3-substituted 6-(4-chlorophenyl)-9-methyl-12H-[1]benzofuro[3,2-e][1,2,4]triazolo[4,3-b][1,2]diazepines via a silylation–amination reaction. *Monatsh. Chem.* 2011, 142, 931-934.
- [11] Marvin 5.10.4, ChemAxon, Calculator Plugins, 2014, <http://www.chemaxon.com/>.
- [12] Gaussian 09, Revision B.01, M. J. Frisch, G. W. Trucks, H. B. Schlegel, G. E. Scuseria, M. A. Robb, J. R. Cheeseman, G. Scalmani, V. Barone, B. Mennucci, G. A. Petersson, H. Nakatsuji, M. Caricato, X. Li, H. P. Hratchian, A. F. Izmaylov, J. Bloino, G. Zheng, J. L. Sonnenberg, M. Hada, M. Ehara, K. Toyota, R. Fukuda, J. Hasegawa, M. Ishida, T. Nakajima, Y. Honda, O. Kitao, H. Nakai, T. Vreven, J. A. Montgomery, Jr., J. E. Peralta, F. Ogliaro, M. Bearpark, J. J. Heyd, E. Brothers, K. N. Kudin, V. N. Staroverov, T. Keith, R. Kobayashi, J. Normand, K. Raghavachari, A. Rendell, J. C. Burant, S. S. Iyengar, J. Tomasi, M. Cossi, N. Rega, J. M. Millam, M. Klene, J. E. Knox, J. B. Cross, V. Bakken, C. Adamo, J. Jaramillo, R. Gomperts, R. E. Stratmann, O. Yazyev, A. J. Austin, R. Cammi, C. Pomelli, J. W. Ochterski, R. L. Martin, K. Morokuma, V. G. Zakrzewski, G. A. Voth, P. Salvador, J. J. Dannenberg, S. Dapprich, A. D. Daniels, O. Farkas, J. B. Foresman, J. V. Ortiz, J. Cioslowski, and D. J. Fox, Gaussian, Inc., Wallingford CT, 2010.
- [13] Wolinski, K.; Hilton, J.F.; Pulay, P. Efficient implementation of the gauge-independent atomic orbital method for NMR chemical shift calculations. *J. Am. Chem. Soc.* 1990, 112, 8251-8260.

## Decay of multiple quantum NMR coherences in quasi-one-dimensional chains in calcium fluorapatite

G.A. Bochkin<sup>1</sup>, F.B.Fel'dman<sup>1</sup>, I.D.Lazarev<sup>1,2</sup>, S.G.Vasil'ev<sup>1</sup>, V.I.Volkov<sup>1</sup>

<sup>1</sup>Institute of Problems of Chemical Physics of Russian Academy of Sciences, Chernogolovka, Moscow Region, Russia 142432

<sup>2</sup>Faculty of Fundamental Physical-Chemical Engineering, Lomonosov Moscow State University, GSP-1, Moscow, Russia 119991

e-mail: [bochkin.g@yandex.ru](mailto:bochkin.g@yandex.ru)

Multiple quantum (MQ) NMR experiment is considered on chains of fluorine atoms in calcium fluorapatite. The second moments of the line shapes of the MQ coherences on the evolution period of the MQ NMR experiment are calculated analytically in the approximation of nearest neighbor interactions. The calculated values are used for a description of the experimental data with semi-phenomenological formulas assuming that the relaxation of the MQ coherences follows the Gaussian law on the evolution period. A satisfactory agreement with the experimental data is demonstrated.

### Introduction

Multiple quantum (MQ) spectroscopy [1] is an effective method for investigating the spatial distribution of nuclei in solids [1,2,3]. It also proved useful for the study of correlated clusters on the preparation period [4,5] and the dependence of the decoherence time in strongly correlated clusters on their size, both in one- [4] and three-dimensional cases [6]. This is possible because MQ NMR experiment allows both creating correlated clusters of spins (on the preparation period) and studying their relaxation (on the evolution period) [7,8]. The relaxation on the evolution period occurs due to the dipole-dipole interaction. The second moments of the line shape of MQ coherence of various orders are useful for estimating the speed of dipolar relaxation of those coherences.

In the present work, we consider the fluorine chains in fluorapatite. The distance between neighboring chains in the crystal is about 2.7 times bigger than the distance between the neighboring fluorine atoms on the same chain, which allows us to consider the system to be quasi-one-dimensional. The chains are sufficiently long that they can be considered infinite for calculation purposes; besides, in the  $zz$  model, calculations for several finite (6 to 48 atoms) chains didn't give better agreement with experimental data than the calculation for an infinite chain [9].

The behavior of the system on the preparation period, in the approximation of nearest-neighbor interactions, had been investigated in [10] and an exact solution found. Only MQ coherences of order 0 and  $\pm 2$  appear. We use that solution as the initial condition for investigation of the behavior of the system on the evolution period. The density matrix of the system has the form:

$$\rho = \rho_0 + \rho_2 + \rho_{-2}, \quad (1)$$

where  $\rho_n$  describes the coherence of order  $n$ . The  $\rho_n$  can be expressed as follows:

$$\rho_0 = \frac{1}{2} \sum_k \cos(2D\tau \sin k) (1 - 2a_k^+ a_k) \quad (2)$$

$$\rho_2 = -\frac{1}{2} \sum_k \sin(2D\tau \sin k) a_k a_{-k} \quad (3)$$

$$\rho_{-2} = \frac{1}{2} \sum_k \sin(2D\tau \sin k) a_k^+ a_{-k}^+ \quad (4)$$

where  $D$  is the dipolar interaction constant between nearest neighbors,  $\tau$  is the length of the preparation period;  $k = -\pi, \frac{2\pi}{N} - \pi, \dots, \pi - \frac{2\pi}{N}$ ;  $N$  is the chain length; and  $a_k, a_k^+$  are the fermion operators:

$$a_k^+ = \frac{1}{\sqrt{N}} \sum_m e^{ikm} 2^{m-1} I_1^z I_2^z \dots I_{m-1}^z I_m^-, \quad a_k = \frac{1}{\sqrt{N}} \sum_m e^{-ikm} 2^{m-1} I_1^z I_2^z \dots I_{m-1}^z I_m^+ \quad (5)$$

where  $I_m^+, I_m^-$  are the raising and lowering operator of spin  $m$ , and  $I_m^\alpha$  is the  $\alpha$ -projection ( $\alpha = x, y, z$ ) of the spin angular momentum operator.

On the evolution period, we use the following Hamiltonian:

$$H_{dz} = D \sum_{i=1}^{N-1} (2I_i^z I_{i+1}^z - I_i^x I_{i+1}^x - I_i^y I_{i+1}^y) \quad (6)$$

However, the analytical calculation of relaxation of the MQ coherence on the evolution period with this Hamiltonian is too complicated. Therefore, we only calculate the second moment of the line shape of the relaxation of that coherence:

$$M_2^{(n)} = -\frac{d^2 F_n(\tau, t)}{dt^2} \frac{1}{F_n(\tau, 0)} \Big|_{t=0}, \quad (n = 0, 2), \quad (7)$$

where  $F_n(\tau, t)$  is the intensity of the MQ coherence of the order  $n$  after a preparation period of length  $\tau$  and evolution period of length  $t$ .

By substituting the expression for the intensity of MQ coherence

$$F_n(\tau, t) = \frac{\text{Tr}[e^{-iH_{dz}t} \rho_n(\tau) e^{iH_{dz}t} \rho_{-n}(t)]}{\text{Tr}(I_z^2)} \quad (8)$$

into (7), we obtain

$$M_2^{(n)} = \frac{\text{Tr}([\rho_n, H_{dz}][H_{dz}, \rho_{-n}])}{\text{Tr}(I_z^2) F_n(\tau, 0)} \quad (9)$$

For a comparison with the experimental data, we note that the relaxation of the MQ coherences on the evolution period can be approximated by the Gaussian function, with the addition of a constant term for the MQ coherence of order 0:

$$\tilde{F}_n(\tau, t) = [F_n(\tau, 0) - A_n^{st}] \exp\left(-\frac{F_n(\tau, 0) M_2^{(n)}(\tau) t^2}{F_n(\tau, 0) - A_n^{st} 2}\right) + A_n^{st}. \quad (10)$$

The constant term is added because there exists a part of density matrix (2) not subject to dipolar relaxation [11], which is responsible for the MQ coherence of order 0 not tending to zero (at time scales considered here, which are much less than  $T_1$ ). We use the analytical expression for the stationary coherence intensity from there.

### Calculation of the second moment of MQ coherence of order zero

We have found that the flip-flop part of the Hamiltonian (6) in the approximation of nearest neighbor interactions

$$H_{ff} = -D \sum_{i=1}^{N-1} (I_i^x I_{i+1}^x + I_i^y I_{i+1}^y) \quad (11)$$

commutes with the  $\rho_0$  part of the density matrix (the order-0 MQ coherence at the end of the preparation period) for chain lengths  $N \gg 1$ . Therefore, the flip-flop part does not contribute to the second moment of MQ coherence of order 0. This allows us to use the solution in the  $zz$  model [9,11], with the Hamiltonian

$$H_{zz} = 2D \sum_{i=1}^{N-1} I_i^z I_{i+1}^z \quad (12)$$

A long calculation [12] gives

$$M_2^{(0)}(\tau) = 4D^2 \left( 1 - \frac{2J_0^2(2D\tau) + 2J_2^2(2D\tau)}{1 + J_0(4D\tau)} \right), \quad (13)$$

where  $J_k$  are the Bessel functions of the first kind of order  $k$ .

### Calculation of the second moment of MQ coherence of order two

For the MQ coherence of order 2, the flip-flop part of the Hamiltonian has to be taken into account. Using the formula (9), we need to calculate

$$\begin{aligned} \text{Tr}([\rho_2, H_{dz}][H_{dz}, \rho_{-2}]) &= \text{Tr}([\rho_2, H_{zz}][H_{zz}, \rho_{-2}]) + \text{Tr}([\rho_2, H_{ff}][H_{ff}, \rho_{-2}]) + \\ &+ \text{Tr}([\rho_2, H_{ff}][H_{zz}, \rho_{-2}]) + \text{Tr}([\rho_2, H_{ff}][H_{ff}, \rho_{-2}]) \end{aligned} \quad (14)$$

The cross terms (the second and third summands in the right-hand side of the above equation) turn out to be zero. This can be shown (for the second summand) as follows.  $\rho_2$  is a sum of terms, each of which is a product containing two raising operators, one of which acts on an odd-numbered spin, and the other on the even-numbered spin. This is easier to see from the solution on the preparation period for the finite chain [13]. The same is true for the commutator  $[\rho_2, H_{zz}]$ . On the other hand, the commutator  $[H_{ff}, \rho_{-2}]$ , as a simple calculation shows, is a sum of products containing two lowering operators acting on two even-numbered or two odd-numbered spins. Therefore the trace of their product is zero. (The proof for the other term is similar).

That means the second moment of MQ coherence of order 2 is a sum of contributions from flip-flop and  $zz$  parts of the Hamiltonian.

Again, the solution for the intensity of MQ coherence on the evolution period in the  $zz$  model [11, 9] can be used for the calculation of the contribution of the  $zz$  part. The contribution of the flip-flop part can be calculated using the fermionic representation. In the end, we obtain the following [12]:

$$M_2^{(2)} = \frac{4D^2}{1 - J_0(4D\tau)} \left( \frac{3}{2}(1 - J_0(4D\tau)) - 2J_1^2(2D\tau) - \frac{1}{2}J_2(4D\tau) \right) \quad (15)$$

### Comparing the theoretical predictions and the experimental data

The experiments were performed on a Bruker Avance III spectrometer on a single crystal of calcium fluorapatite with static magnetic field of 9.4 T (the corresponding frequency on  $^{19}\text{F}$  nuclear spins is 376.6 MHz). The results of the comparison of the semi-phenomenological formula (9) and the exact solution in the  $zz$  model with the experimental data are presented in Figs. 1,2. One can see that the semi-phenomenological formula (10) with calculated coefficients gives a better agreement with experimental data than the exact solution in the  $zz$  model.

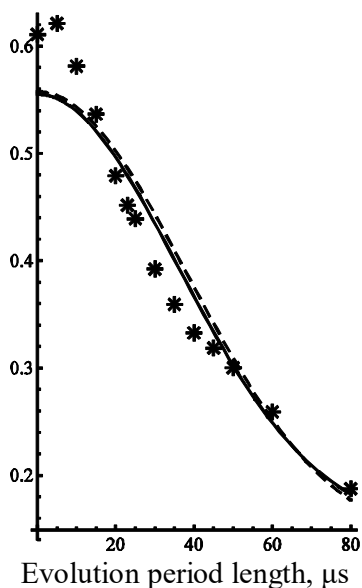


**Figure 1.** Experimental (points) and theoretical (lines) intensity of MQ coherence of order 0 for length of the preparation period of 126  $\mu\text{s}$  in fluorapatite. The solid line is the Gaussian function with the calculated stationary intensity, initial intensity and second moment. The dashed curve is the prediction of the  $zz$  model.

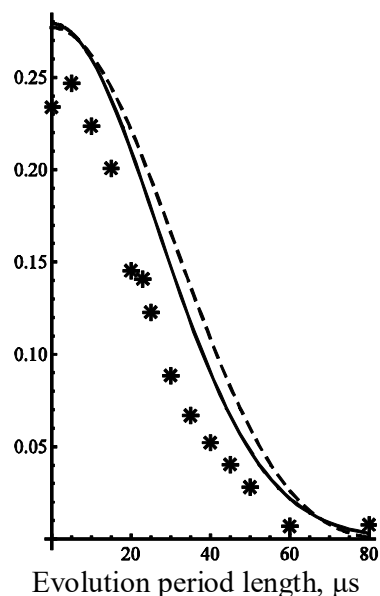


**Figure 2.** Experimental (points) and theoretical (lines) intensity of MQ coherence of order 2 for length of the preparation period of 139.2  $\mu\text{s}$  in fluorapatite. The solid line is the Gaussian function with the calculated initial intensity and second moment. The dashed curve is the prediction of the  $zz$  model.

### References

- [1] J. Baum, M. Munovitz, A.N. Garroway, A. Pines, *J.Chem.Phys.* **83**, 2015 (1985)
- [2] J. Baum, A. Pines, *J.Am.Chem.Soc.* **108**, 7447 (1986)
- [3] J. Baum, K.K. Gleason, A. Pines, A.N. Garroway, J.A.Reimer, *Phys.Rev.Lett.* **56**, 1377 (1986)
- [4] H.C. Krojanski, D. Suter, *Phys.Rev.Lett.* **93**, 090501 (2004)
- [5] G. Cho, P. Capellaro, D.G. Cory, C. Ramanathan, *Phys.Rev.B* **74**, 224434 (2006)
- [6] G.A. Bochkin, E.B. Fel'dman, S.G. Vasil'ev, V.I. Volkov, *Appl.Magn.Reson.* **49**, 25 (2018)
- [7] S.I. Doronin, E.B. Fel'dman, I.I. Maximov, *J.Magn.Reson.* **171**, 37 (2004)
- [8] G. Kaur, A. Ajoy, P. Cappellaro. *New J.Phys.* **15** (9), 093035 (2013)
- [9] G.A. Bochkin, E.B. Fel'dman, S.G. Vasil'ev, V.I. Volkov, *Chem.Phys.Lett.* **680**, 56-60 (2017)
- [10] E.B.Fel'dman, S.Lacelle, *J.Chem.Phys.* **107**, 7067 (1997)
- [11] G.A. Bochkin, E.B. Fel'dman, S.G. Vasil'ev, *Z.Phys.Chem.* 231 (3), 513-525 (2017)
- [12] G.A.Bochkin, E.B.Fel'dman, I.D.Lazarev, S.G.Vasil'ev, *J.Exp.Theor.Phys.* In press (Russian version: Бочкин Г.А., Васильев С.Г., Лазарев И.Д., Фельдман Э.Б. *ЖЭТФ* **154**, 621 (2018)).
- [13] S.I. Doronin, I.I. Maksimov, E.B. Fel'dman, *J.Exp.Theor.Phys.* **91**, 597 (2000)

## Atomic-scale probing of paramagnetic centers in nanodiamonds by $^3\text{He}$ NMR.

Gleb Dolgorukov<sup>1</sup>, Vyacheslav Kuzmin<sup>1</sup>, Kajum Safiullin<sup>1</sup>, Andrey Stanislavovas<sup>1</sup>, Egor Alakshin<sup>1</sup>, Timur Safin<sup>1</sup>, Boris Yavkin<sup>1</sup>, Sergei Orlinskii<sup>1</sup>, Alexander Klochkov<sup>1</sup>, Murat Tagirov<sup>1,2</sup>

<sup>1</sup> Institute of Physics, Kazan Federal University, 420008, Kremlevskaya 18, Kazan, Russian Federation

<sup>2</sup> Institute of Applied Research, TAS, 420111, Levo-Bulachnaya 36a, Kazan, Russian Federation

The broad spectrum of potential applications of nanodiamonds initiated a large number of scientific studies of their properties. Recently it was demonstrated that some types of paramagnetic centers in nanodiamonds (NV-centers) can be successfully used as nanoscale sensors of the surrounding environment in NMR [1]. That requires the accurate determination of location of paramagnetic centers in nanodiamonds.

A new original technique that provides detailed information on the spatial distribution of paramagnetic impurities in nanodiamonds is presented here [2]. It is based on the measurement of relaxation times of adsorbed  $^3\text{He}$  separated from the sample surface by variable thickness of preadsorbed layer of an inactive gas.

Detonation nanodiamonds powder with nearly spherical particles and with sizes of 3-10 nm was used as a sample. Transmission electron microscopy (TEM), electron paramagnetic resonance (EPR), powder X-ray diffraction and nitrogen adsorption techniques were used for the detailed sample characterization.

Adsorbed  $^3\text{He}$  NMR experiments were performed in the temperature range of 1.5-4.2 K at 5-19 MHz resonance frequencies using a home-built pulsed NMR spectrometer [3]. In our experiments  $^3\text{He}$  was adsorbed either on a clean sample surface or onto preadsorbed layers of nitrogen. Preadsorption of the sample with a certain amount of nitrogen layers was performed during the slow cooling from room temperature down to 4.2 K.

We performed NMR measurements of adsorbed  $^3\text{He}$  on nanodiamonds with clean surface and with surface with preadsorbed nitrogen layers. Measured  $^3\text{He}$  longitudinal magnetization recovery and transverse magnetization decay curves are described well by single exponential functions.

The obtained temperature dependencies of adsorbed  $^3\text{He}$  spin-lattice relaxation rates show nonlinear behavior with maxima values  $T_1^{-1}\text{max}$  (Fig. 1). The temperature  $T_{\text{max}}$  of the maxima relaxation depends on the  $^3\text{He}$  monolayer coverage. It was found that the value of the maximum relaxation rate  $T_1^{-1}\text{max}$  strongly depends on the amount of preadsorbed nitrogen layers (Fig. 2), i.e. on the distance between the adsorbed  $^3\text{He}$  and nanodiamond surface. The closer adsorbed  $^3\text{He}$  is to the nanodiamond surface, the faster relaxation occurs.

EPR measurements on this sample revealed a high concentration of paramagnetic centers (order of  $10^{20}$  per gram). It is also known that paramagnetic centers in detonation nanodiamonds are located in nanodiamond shell [4], which is consistent with performed sample characterization.

Taking into account these facts we suggest the  $^3\text{He}$  relaxation model [2], which implied that  $^3\text{He}$  relaxation is governed by paramagnetic centers and intrinsic dipolar relaxation in adsorbed  $^3\text{He}$  film. The fits of experimental data by this model provide distance to paramagnetic centers (Fig.2). The obtained average distance between paramagnetic centers of

nanodiamonds and its surface is  $0.6\pm 0.1$  nm. This value is in a good agreement with the fact that paramagnetic centers are located in the nanodiamond shell.

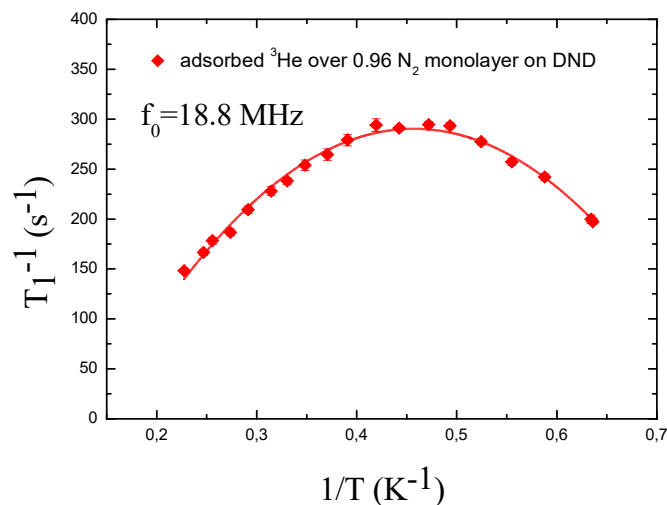


**Figure 1.** Temperature dependences of  $^3\text{He}$  spin–lattice relaxation rate  $T_1^{-1}$  at monolayer coverage of the nanodiamond powder sample preplated with nitrogen layer ( $N = 0.96$ ). Solid line represent fit by the parabolic function.

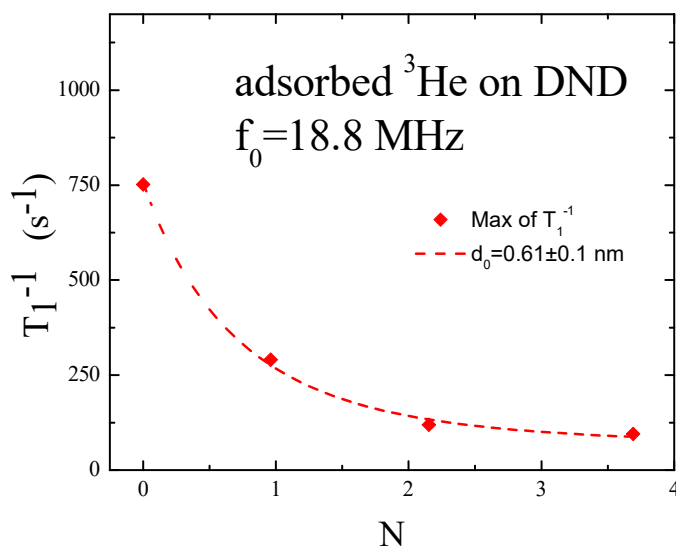


**Figure 2.** The dependence of  $^3\text{He}$  spin-lattice relaxation rate adsorbed on nanodiamonds (full monolayer coverage) on amount of preadsorbed nitrogen layers at 18.8 MHz resonance frequency.

The NMR measurements of adsorbed  $^3\text{He}$  on nanodiamonds have been performed at low temperatures. The suggested relaxation model explains obtained experimental data on  $^3\text{He}$  relaxation and allows to determine the location of near-surface paramagnetic centers in nanodiamonds quantitatively with a high precision. According to the relaxation model and the

## PROCEEDINGS

obtained experimental results, the average distance between paramagnetic centers and surface of nanodiamonds is  $0.5 \pm 0.1$  nm. This value is consistent with the information on detonation nanodiamond structure obtained during the sample characterization. The proposed technique can be used in studies of nanoscaled samples with paramagnetic impurities.

### References

- [1] T. Staudacher, et al. Nuclear Magnetic Resonance Spectroscopy on a (5-Nanometer)<sup>3</sup> Sample Volume. – *Science*, 2013, 339, 561
- [2] Kuzmin V. et al. Angstrom-scale probing of paramagnetic centers location in nanodiamonds by <sup>3</sup>He NMR at low temperatures. – *Phys. Chem. Chem. Phys.*, 2018, 20, 1476
- [3] Alakshin et al. The home-built pulse nuclear magnetic resonance spectrometer with digital quadrature detection for <sup>3</sup>He research at low temperatures. – *Magn. Reson. Solids*, 2013 15, 13104
- [4] O. A. Shenderova, – *Detonation nanodiamonds: science and applications*, Pan Stanford Publishing, Singapore, 2014

## Conventional magnon BEC in YIG films

Yu. M. Bunkov<sup>1</sup>, A. R. Farhutdinov<sup>1</sup>, G. V. Mamin<sup>1</sup>, S. B. Orlinskii<sup>1</sup>, T. R. Safin<sup>1</sup>,  
P. M. Vetoshko<sup>2</sup>, D. G. Zverev<sup>1</sup> and M. S. Tagirov<sup>1,3</sup>

<sup>1</sup>Kazan Federal University, 420008, Kazan, Russia.

<sup>2</sup>Russian Quantum Center, 143025, Moscow, Russia.

<sup>3</sup>Institute of Applied Research, TAS, 420111, Kazan, Russia.

e-mail: farhutdinov@yandex.ru

We report the observation of conventional magnon Bose-Einstein condensation (BEC of magnons with  $k = 0$ ) at room temperature. The experiments were performed in thin films of Yttrium Iron Garnet (YIG) with magnetic field  $\mathbf{H}_0$  perpendicular to the plane of the film.

The condition of magnon BEC formation in magnetically ordered materials is the same as for a diluted gas. The BEC forms at the temperature below the critical temperature  $T_c$

$$T_c = 3.31 \frac{\hbar^2}{k_B m} \left(\frac{N}{V_S}\right)^{2/3}, \quad (1)$$

where  $N$  is the number of bosons in the volume  $V_S$ . The density of the magnons at the equilibrium conditions is always below the critical density. Indeed, we are able to increase the number of magnons using external excitation. For example, if one can deflect the magnetization of the system  $\mathbf{M}$  from the direction of the external magnetic field  $\mathbf{H}_0$  by an angle  $\beta$ , at constant temperature, the number of magnons increases by the

$$N = \frac{\chi H_0}{\hbar \gamma} (1 - \cos \beta), \quad (2)$$

where  $\chi$  – magnetic susceptibility,  $\gamma$  – gyromagnetic ratio. The critical density of magnons at given temperature results from the eq. (1). At higher concentration, the magnons form the BEC state. This liquid has all properties of superfluid liquid. Due to the magnons interaction their resonant frequency depends on the density of the magnons. This behavior results in the effect similar to Meissner effect for superconductors – in our case it is the compensation of the inhomogeneity of the magnetic field by a spatial redistribution of the magnons density. Thus, the uniform precession of magnetization in non-uniform magnetic field is spontaneously formed. This effect was described previously in [1] as a Long Living Induction Decay signal. For the case of BEC we have an excited coherent state of magnons with  $k = 0$ , however, this state arises as a result of a change in the density of magnons [2].

According to [3] the critical value of  $\beta$  for magnon BEC formation in YIG film at room temperature is about  $2.5^\circ$ . External magnetic field  $\mathbf{H}_0$  is directed perpendicular to the plane of the film in our experiments. Magnons were pumped using field  $\mathbf{H}_1$  with frequency  $f = 9.26$  GHz oscillated within the film plane. Thus, we reach BEC transition at room temperature. The signals of Long Lived Induction Decay and CW magnetic resonance typical for the conventional magnon BEC in antiferromagnetic superfluid  $^3\text{He}$  [4] and others magnetically ordered systems were observed.

This work was supported by the Russian Science Foundation (project no. 16-12-10359).

## PROCEEDINGS

### References

- [1] A. S. Borovik-Romanov, Yu. M. Bunkov, V. V. Dmitriev, Yu. M. Mukharskiy. JETP Lett. **40**, 1033 (1984)
- [2] Yu.D. Kalafati, V.L. Safonov, J. Magn. Magn. Mater. 123, 184 (1993).
- [3] Yu. M. Bunkov and V. L. Safonov, J. Magn. Magn. Mater. 452, 30 (2018).
- [4] Yu.M. Bunkov, G. E. Volovik, Novel Superfluids, (Oxford University press, Oxford, 2013).

## Investigation of synthetic octacalciumphosphate content and structure with electron paramagnetic resonance.

A Fedotov<sup>1</sup>, M Gafurov<sup>2,\*</sup>, I Smirnov<sup>1</sup>, B Yavkin<sup>2</sup>, G Mamin<sup>2</sup>, S Orlinskii<sup>1</sup> and VS Komlev<sup>1</sup>

<sup>1</sup> A.A. Baikov Institute of Metallurgy and Materials Science, Russian Academy of Sciences, 49 Leninsky Pr., Moscow, Russia

<sup>2</sup> Kazan Federal University, 18 Kremlevskaya Str., Kazan, Russia

e-mail: marat.gafurov@kpfu.ru

Among the various calcium phosphates (CP) used for bone implants preparation, octacalcium phosphate (OCP) is of great interest. Materials based on OCP can easily be transformed into natural hydroxyapatite, the main inorganic material of bone tissue in the human body, providing a higher rate of transformation compared to the other CP, which directly affects the patient recovery time.

OCP is a metastable CP due to the presence of a large quantity of water molecules in the crystal lattice. Slight temperature influence or pH fluctuations can lead to irreversible transformation of OCP into non biocompatible compounds. Thus, formation of OCP implants with standard methods is impossible, so new technological approaches are needed.

OCP material, which investigated in this work, made by transformation of the initial ceramics  $\alpha$ -tricalciumphosphate ( $\alpha$ -TCP).  $\alpha$ -TCP ceramic granules were immersed to 1000 ml of sodium acetate aqueous solution with glutamic amino acid and orthophosphoric acid. Such buffer system make  $\alpha$ -TCP transform to dicalciumphosphate dihydrate (DCPD). Further hydrolysis of DCPD in sodium acetate aqueous solution leads to formation of OCP.

The aim of this work is to investigate OCP ceramics, made by DCPD hydrolysis, by electron paramagnetic resonance (EPR). EPR may detects paramagnetic impurities, trapped free radicals or hole centres.

Pure, non-substituted OCP is supposed to be EPR silent. In the investigated samples no EPR signal was detected at room temperature (i.e. concentration of the paramagnetic impurities  $C < 10^{15}$  spin/g) while after the irradiation a signal in the central part of the spectrum appears with the total concentration of  $C \sim 8(1) \cdot 10^{16}$  spin/g.

The central part of the spectrum (in the magnetic field range of 300-400 mT) for the irradiated species was investigated in details. From Figure 1 it follows that a pair of weak lines with the splitting of about 500 mT due to the  $H^0$  (nuclear spin  $I = 1/2$ ) could be observed. This feature is also characteristic for the HA and TCP materials synthesized by solid state reaction. But the part of the spectrum in the range of the magnetic fields of 340-350 mT resembles those for HA and TCP synthesized by the wet precipitation techniques. The remarkable differences for CaP produced by various methods could be exploited for the fairly simple identification of the synthesizing route of the commercial CaP materials, for example which is often a proprietary information.

We have studied the behavior the signal in the range of the magnetic fields of 340-350 mT comprehensively. Figure 2 presents the dependence of the spectrum on microwave power. At least two different sorts of paramagnetic centres could be distinguished: while the intensity and amplitude of the broad line in the middle of the spectrum with the linewidth of 1 mT is growing with power (denoted as a paramagnetic centre 1, PC<sub>1</sub> while the second “structural” paramagnetic centre (PC<sub>2</sub>) with the with the maximal splitting of 55 mT starts to saturate already at  $P_{MW} = 10$  mW. Lineshape of PC<sub>1</sub> resembles those for the carbonate centered stable

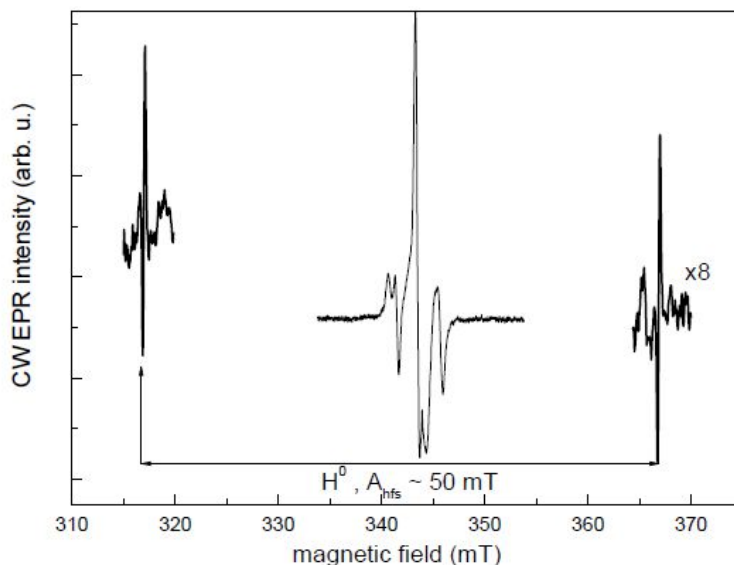


**Figure 1.** Conventional room-temperature X-band EPR of X-irradiated sample of OCP.

radicals in HA. To study the nature of PC<sub>1</sub> in details we have measured transverse ( $T_2$ ) and longitudinal ( $T_1$ ) relaxation times at  $T = 100$  K by pulsed methods ( $\pi/2$ - $\tau$ - $\pi$  and  $\pi$ - $T$ - $\pi/2$ - $\tau$ - $\pi$  pulse sequence, correspondingly) in the magnetic field marked by the blue dashed line in Figure 2.  $T_2$  curve can be described by only one exponential decay with  $T_2 = 1.8 \mu\text{s}$ .  $T_1$  curve is presented in Figure 3.

Experimental points on  $T_1$  curve were approximated by one-, two- and three exponents with the corresponding  $T_1$  times (1)  $T_1 = 0.5$  ms; (2)  $T_1^{(1)} = 0.06$  ms,  $T_1^{(2)} = 0.7$  ms; (3)  $T_1^{(1)} = 0.02$  ms,  $T_1^{(2)} = 0.2$  ms,  $T_1^{(3)} = 1.2$  ms. As it follows from Figure 3, three-exponential description is the best one. Assuming that the centre with the longest  $T_1$  belongs to PC<sub>2</sub>, there are two types of the fast relaxing centres in OCP.

EPR pattern of the slowly relaxing PC<sub>2</sub> resembles that in HA. In the irradiated HA samples EPR is mainly due to the stable  $\text{NO}_3^{2-}$  ions preferably substituting one of the PO<sub>4</sub><sup>3-</sup> position in the HA structure (substitution of B-type). Their powder EPR spectra can be described by the

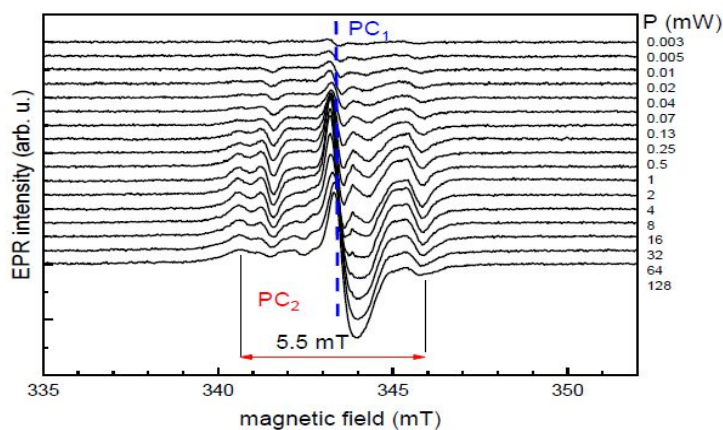


**Figure 2.** Conventional room-temperature X-band EPR of the X-irradiated sample of OCP at different microwave power levels. Lines with different microwave saturation behavior are marked.

spin-Hamiltonian of the axial symmetry. The HA spectra could be simulated properly if we

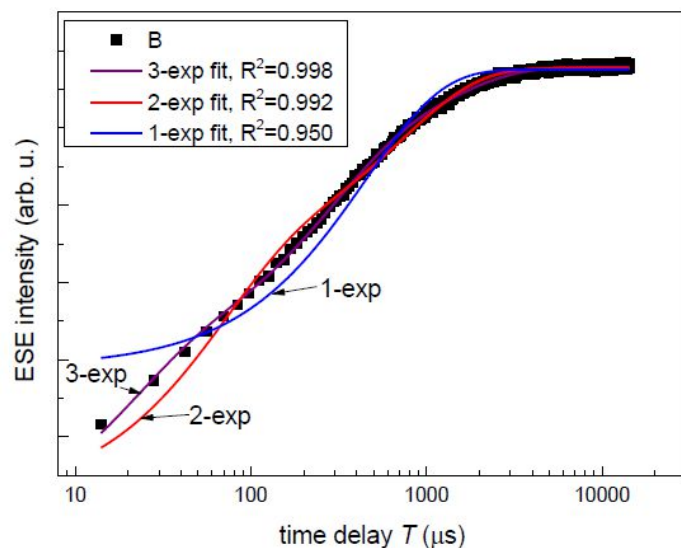


**Figure 3.** T1 curve (filled squares) with the corresponding approximations by one-, two- and three exponents.

supposed a Gaussian (continuous) distribution of  $A_{\parallel}$  with a deviation of 0.40 mT around the mean value of 6.65(40) mT and a discrete distribution of  $A_{\perp}$  around 3.37(5) mT, while the components of  $g$ -factors for all of the obtained radical's modifications are the same ( $g_{\parallel} = 2.0011(1)$ ,  $g_{\perp} = 2.0052(1)$ ).

As it follows from the presented results, in OCP we have to suggest  $A_{\parallel} = 5.5/2 = 2.7$  mT. Such small value forces to suggest the presence of other nitrogen containing radicals such as NO<sub>2</sub>, for example, or other paramagnetic centers.

Modern EPR techniques offer various opportunities for the rapid testing and comprehensive analysis of the condensed matter. The capabilities of even conventional EPR approaches for investigation and analysis of calcium phosphate materials are still not fully exploited and described in details. We hope that our paper would serve as a first step in understanding the nature and structure of various paramagnetic centers in octacalciumphosphates with the purpose of their usage as sensitive intrinsic probes to follow the changes under the doping or surface treatment.

The work was funded by the Russian Foundation for Basic Research 18-29-11086 MK.

**NMR study of electron-doped cubic manganites**  
 **$\text{Sr}_{1-x}\text{La}_x\text{MnO}_3$**

A.Yu. Germov, Z.N. Volkova, A.P. Gerashenko, K.N. Mikhalev, S.V. Verkhovskii

Institute of Metal Physics, Ural Branch of the Russian Academy of Sciences, 620108,  
 S. Kovalevskaya st. 18, Yekaterinburg, Russian Federation.

e-mail: [germov@imp.uran.ru](mailto:germov@imp.uran.ru)

Among strongly correlated magnetic materials, the  $\text{Sr}_{1-x}\text{La}_x\text{MnO}_3$  perovskite oxides are probably the most famous family of the doped manganites showing the metal-insulator transition. On the insulating side of the transition, the magnetic ground state of the doped  $\text{Sr}_{1-x}\text{La}_x\text{MnO}_3$  oxides ( $x > 0.7$ ) is heterogeneous with the ferromagnetic nanosize domains embedded in the antiferromagnetically ordered lattice of the  $\text{Mn}^{3+}$  ( $^3t_{2g}^1e_g$ ) ions. By applying magnetic field the percolation of these conducting ferromagnetic domains occurs yielding a metal-insulator transition with the colossal magnetoresistance effect, a very large reduction of electrical resistivity. The percolation threshold can be achieved at the concentration of doped holes  $(1-x) > 0.16$ .

However, on opposite side of the  $\text{Sr}_{1-x}\text{La}_x\text{MnO}_3$  family, the antiferromagnetic insulating cubic  $\text{SrMnO}_3$  revealed a metallic-like conductivity behavior at very small concentration of the doped electrons ( $x \leq 0.04$ ) appearing due to the heterovalent substitution of  $\text{Sr}^{2+}$  by  $\text{La}^{3+}$ . Such behavior of the doped electrons was explained in terms of the canted antiferromagnetic

metal phase [1]. The corresponding homogeneous ground state of the electron-doped manganite was put upon doubt in the recent  $^{55}\text{Mn}$  NMR experiments [2-4] evidencing a separation of the Mn cations in two species with differently occupied 3d-shell.

Unlike  $^{55}\text{Mn}$ , the NMR signal of  $^{87}\text{Sr}$  nuclei is observed both in the antiferromagnetic and the paramagnetic states. The  $^{87}\text{Sr}$  NMR shift is proportional to the local density of the itinerant doped electrons surrounding the Sr sites, so that the  $^{87}\text{Sr}$  NMR tool allows us to probe spatial distribution of the doped electrons with a resolution of about the cubic unit cell size. The  $^{87}\text{Sr}$  NMR spectra of the electron-doped cubic polycrystalline manganites  $\text{Sr}_{1-x}\text{La}_x\text{MnO}_3$  ( $x = 0; 0.02; 0.04$ ) have been obtained in magnetic field  $H_0 = 11.747$  T at the temperature range from 20 K to 370 K (Fig. 1). For  $x = 0.02$  spectrum the steepness of the low-frequency wing of the central line and its peak position are practically the same as the central line in the parent  $\text{SrMnO}_3$ . Also similarities between spin-spin relaxations allow us to decompose the spectra of the La-

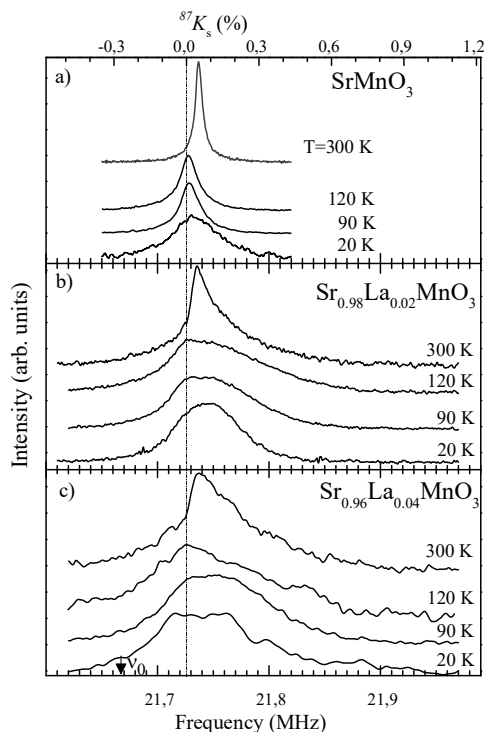


**Figure 1.** The  $^{87}\text{Sr}$  NMR spectra obtained at magnetic field  $H_0 = 11.747$  T in the polycrystalline  $x = 0.00$  (a),  $0.02$  (b),  $0.04$  (c) samples at  $T = 300; 120; 90$  and  $20$  K.

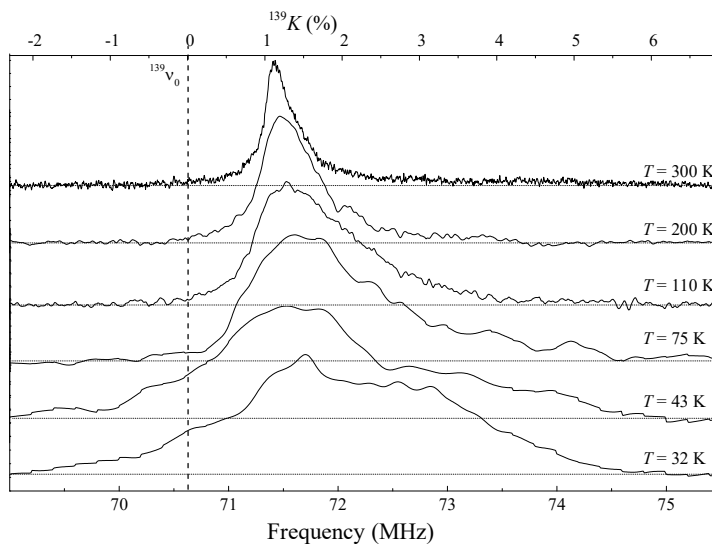


**Figure 2.**  $^{139}\text{La}$  NMR spectra obtained at  $H_0 = 11.747$  T in polycrystalline  $\text{Sr}_{0.98}\text{La}_{0.02}\text{MnO}_3$  at  $T = 300, 200, 110, 75, 43, 32$  K. Diamagnetic point  $^{139}\text{V}_0$  is designated by a dash line.

containing oxides and distinguish part corresponding to the higher electron density regions. It determines the fraction of Sr atoms in the electron doped regions (EDRs).

It is shown that itinerant electrons are inhomogeneously distributed in the La-containing manganites in the paramagnetic phase, creating EDRs with a number of  $e_g$  electrons per Mn larger than in the rest part of the oxide. At room temperature the network of the overlapping EDRs does not cover all Sr sites. Nevertheless, the number of the Sr-sites inside an EDR exceeds the site percolation threshold even for  $x = 0.02$  at  $T = 300$  K, so that the  $e_g$  electrons can move on large distances.

In the antiferromagnetic phase, below 80 K, the EDRs cover the entire crystal. In this temperature range the doped electrons separate into two species: below 50 K, some of them slow down their motion and form static ferromagnetic domains, which are considered as bound magnetic polarons of small size with the effective moment  $p_{\text{eff}} = 23(10) \mu_B$ . The second species concern the doped electrons which remain itinerant at low temperature participating in the fast hopping in the antiferromagnetic G-type ordered lattice of the  $\text{Mn}^{4+}$  ions.

The  $^{139}\text{La}$  NMR spectra of the manganite  $\text{Sr}_{1-x}\text{La}_x\text{MnO}_3$  ( $x = 0.02$ ) have been obtained in magnetic field  $H_0 = 11.747$  T (Fig.2) in the temperature range from 32 K up to 300 K. Difference between the temperature dependencies of the  $^{139}\text{La}$  and  $^{87}\text{Sr}$  NMR line shifts and widths indicate the location of EDRs predominantly on La ions. The  $^{139}\text{La}$  NMR spectra of the manganite  $\text{Sr}_{1-x}\text{La}_x\text{MnO}_3$  ( $x = 0.02, 0.04$ ) obtained at zero external magnetic field ( $H_0 = 0$  T) at 4 K and 77 K evidencing the localization of ferromagnetic domains on La site.

This study is supported by the project of fundamental researches of the Ural Branch of the Russian Academy of Sciences № 18-10-2-37 and grant from the Russian Foundation for basic Research № 18-32-00030 in the assignment of the state program «Spin».

## References

- [1] H. Sakai et. al., Phys. Rev. B **82**, 180409 (2010).
- [2] A. Trokiner et. al., Phys. Rev. B **93**, 174413 (2016).
- [3] A. Germov et. al., JETP letters, **102**, 11, 727 (2015).
- [4] A. Germov et. al., Phys. Rev. B **96**, 104409 (2017).

**Synthesis and sintering of the synthetic hydroxyapatite doped with aluminum**

M. Goldberg<sup>1</sup>, V. Smirnov<sup>1</sup>, O. Antonova<sup>1</sup>, A. Konovalov<sup>1</sup>, D. Titov<sup>1</sup>, V.S. Komlev<sup>1</sup>, S. Barinov<sup>1</sup>, A. Rodionov<sup>2</sup>, M Gafurov<sup>2</sup>, and S Orlinskii<sup>2</sup>

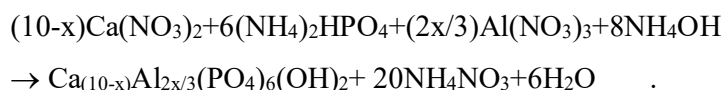
<sup>1</sup> A.A. Baikov Institute of Metallurgy and Materials Science, Russian Academy of Sciences,,  
49 Leninsky pr., Moscow, Russia

<sup>2</sup> Kazan Federal University, 18 Kremlevskaya Str., Kazan, Russia

e-mail: margo.goldberg@yandex.ru

Hydroxyapatite (HA) is one of the most attractive biomaterials for bone reconstruction due to its excellent biological compatibility and osteoconductivity [1,2]. During recent years there have been efforts in developing synthetic HA to enhance its biological and mechanical properties for use in biomedical applications that can be mainly achieved by cationic substitutions of calcium ions [1]. Aluminum can serve as one of the substituents but the biological effect of Al remains controversial (both positive and negative functions of the element in human bone metabolism have been reported) while introduction of Al ions can lead to the significant lattice distortions and influence on sintering processes [4]. Formation of ceramics based on HA and Al<sub>2</sub>O<sub>3</sub> attracts much attention due to enhanced mechanical properties of sintered materials [5]. In our previous work we have demonstrated enhanced solubility of Al in the β-tricalcium phosphate matrix synthesized by precipitation method [6]. In present paper we use the same reaction route to synthesize aluminum substituted hydroxyapatite (Al-HA) powders and to investigate them by different analytical methods to follow the changes caused by aluminum introduction on powders properties and materials sintering.

Samples of Al-HA with the chemical formula Ca<sub>10-x</sub>Al<sub>2x/3</sub>(PO<sub>4</sub>)<sub>6</sub>(OH)<sub>2</sub> were synthesized with x = 0; 0.2 by the precipitation method according to the following reaction using reactants of analytical grade and deionized water:



Calcium and aluminum nitrate solutions were mixed with a diammonium hydrogen phosphate solution in the corresponding ratios. The pH value of the reaction mixture was maintained at a level of 9.0–9.5 by adding aqueous ammonia. Powders were ripened at mother solution during 21 days at temperature of 25°C for full crystallization of precipitate [7]. The obtained powders were filtered, washed and dried at 60°C for 24 h. The powders were heat treated at 300°C for 3 h in air to remove ammonium nitrate, an impurity phase.

For determination of Al content in the precipitates, powders were heat treated at 900 °C for water removing, dissolved in HCl – HNO<sub>3</sub> mixture and analyzed by atomic emission spectrometry with inductively coupled plasma (AES-ICP, HORIBA Jobin Yvon, ULTIMA 2). The powder materials were characterized by the X-ray diffraction (XRD) method (Shimadzu XRD-6000, CuKα radiation) with identification of phase composition according to JCPDS and PCPDFWIN databases. The specific surface area (S) of powders was determined by low-temperature nitrogen adsorption measurements (BET, Micromeritics TriStar analyzer).

PROCEEDINGS

Continuous wave (CW) EPR spectra of the samples were obtained using table-top Labrador (Ekaterinburg, Russia) and ESP-300 (Bruker) spectrometers operating at 9.4 – 9.9 GHz (X-band) microwave frequency. PC concentration was estimated at room temperature in the double cavity ER4105DR of ESP-300 by comparing the integrated intensities of the spectra of a test sample and a reference samples (Cu-DETC solution and  $Mn^{2+}$  in MgO powder). X-ray irradiation of the synthesized powders was provided by using URS-55 tube (U = 55kV, I = 16mA, W anticathode) at room temperature with the estimated dose of 5 kGy to create stable paramagnetic centers in the nominal pure material. The shrinkage data of the sintering powder compacts were obtained using a dilatometer (NETZSCH DIL 402C). Measurements of shrinkage were carried out in the range from room temperature to 1450 °C in argon atmosphere the heating rate was 10 °C/min.

Data on Al content in the investigated species are presented in Table 1 which shows that the chemical composition of synthesized materials is close to the predetermined one.

**Table 1.** Powder composition and surface area for the investigated species.

Ca substitution by Al, mol.%	Stoichiometric formulae	Al theoretical, mol. %	Al theoretical, wt. %	Al measured, wt. %	S, m <sup>2</sup> /g
0	Ca <sub>10</sub> (PO <sub>4</sub> ) <sub>6</sub> (OH) <sub>2</sub>	0	0	< 10 <sup>-4</sup>	91±1
20	Ca <sub>8</sub> Al <sub>1.33</sub> (PO <sub>4</sub> ) <sub>6</sub> (OH) <sub>2</sub>	20	3.629	3.62 ± 0.04	90±1

According to the XRD analysis, both powders consist of apatite-like phases with the low crystallinity degree (Figure 1). The only detected phase in both samples was hydroxyapatite (JCPDS #9-432). The shape of triplet between 30.5 ° and 33.5 ° of HA sample became smoother and transformed into the duplet with introduction of Al due to decrease of crystallinity degree of powders in correspondence with ref. [8].

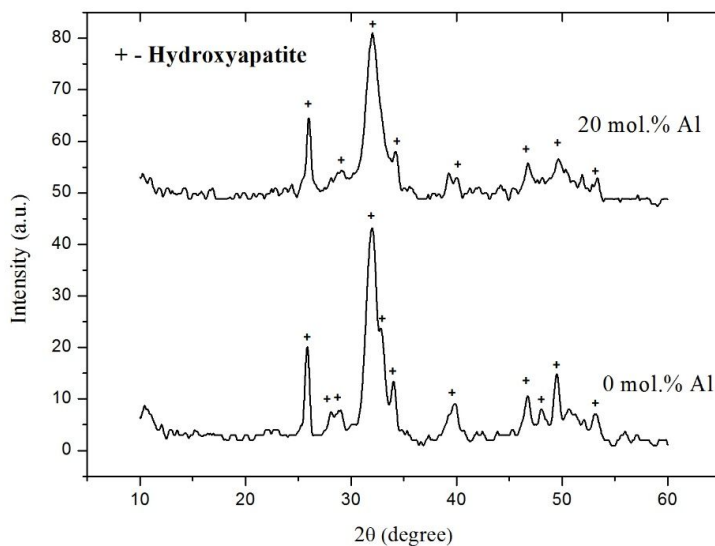


**Figure 1.** XRD spectra of Al-substituted HA powders. Peaks marked with “+” correspond to HA (JCPDS No: 9 -432).

According to the gas absorption data, aluminum introduction does not change the specific area of the synthesized powders that is in the range of 90-91 m<sup>2</sup>/g (Table 1).

Pure HA and Al-HA samples are supposed to be EPR silent. Indeed, in the investigated species no EPR signals within the sensitivity limits of our equipment was found that confirms the purity of the initial reagents and proper synthesis treatment [9]. The paramagnetic centers appear after the X-ray irradiation (Figure 2). The EPR patterns are very close to each other and mainly are due to the known in HA synthesized by the wet precipitation technique from the nitrate containing reagents CO<sub>2</sub><sup>-</sup> and NO<sub>3</sub><sup>2-</sup> stable radicals [10]. As we have shown previously in refs [9], introduction of even non-paramagnetic impurities can lead to the significant changes of the relaxation and spectroscopic parameters of the radiation induced defects. From the presented EPR results it follows that the spectroscopic parameters of the obtained radiation-induced defects do not change with the aluminum doping and, therefore, gives an opportunity to follow electron-nuclei interactions with the Al nuclei in the way similar to the previously described for other aluminum containing matrices [12].

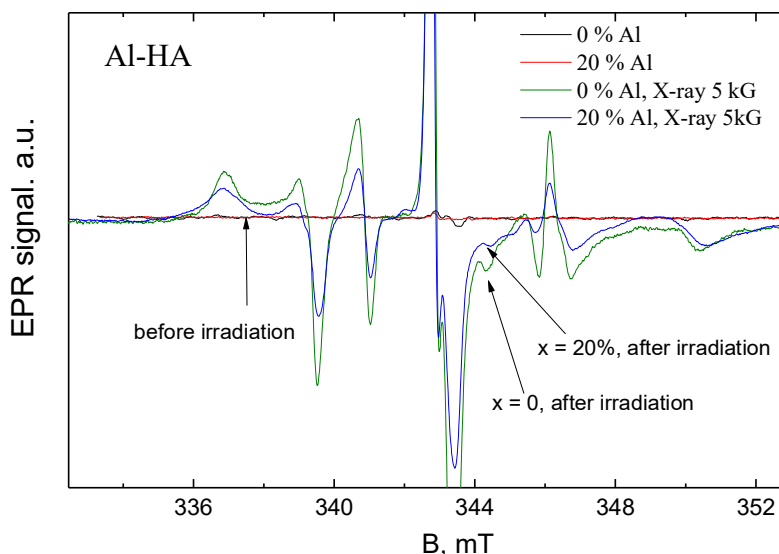


**Figure 2.** EPR spectra of Al-HA samples before and after X-ray irradiation.

The figure 3 shows the change of the shrinkage of HA and Al-HA compact during non-isothermal sintering obtained by dilatometer study. Al introduction led to shift the material sintering beginning point from 910 °C to 756 °C. The sintering of Al-HA ceramic passed in the two stages and the shrinkage reached value of 29,99 % compared to 23,06 % for pure HA. The starting of the low temperature densification could be attributed to the defect structure formed by introduction of Al ions in the HA lattice. Further sintering at 1200-1400 °C occurred simultaneously with transformation of HA into tricalcium phosphate and Ca<sub>9</sub>Al(PO<sub>4</sub>)<sub>7</sub>(OH)<sub>2</sub> phases [14,6].

Summarize, the influence of Al introduction in synthetic HA was studied and changes in the powders properties and sintering processes were demonstrated. Al-HA materials characterized by defect structure, which leads to the beginning of sintering at lower temperature, compared to pure HA.

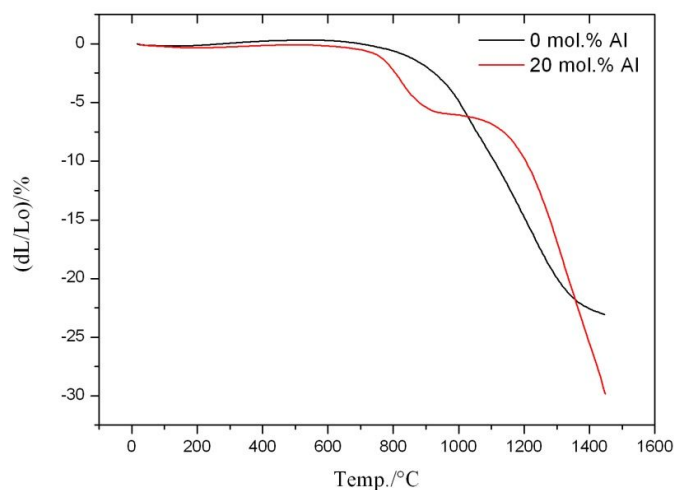


**Figure. 3** Temperature dependence of shrinkage for the samples HA and Al-HA at heating rate 10 °C/min

#### Acknowledgements

The powders synthesis and XRD, SEM, AES-ICP and gas absorption investigations were performed with financial support of Russian Science Foundation under the grant # 16-13-00123. EPR analysis was conducted with support of State assignment № 007-00129-18-00.

#### References

- [1] Barinov S 2010 Russ. Chem. Rev.79 13
- [2] Laskus A, Kolmas J 2017 Int. J. Mol. Sci.18 2542
- [3] Wang P.E., Chaki T.K. 1993 J. Mater. Sci. Med. 4 150.
- [4] Wang M, Wang L, Shi C, Sun T, Zeng Y, Zhu Y 2016 Phys. Chem. Chem. Phys. 18 21789
- [5] Horng Y, Min H, 1994 Mater. Sci. Eng. C. 2 77.
- [6] Goldberg M, Smirnov V, Protsenko P, et al. 2017 Ceram. Int. 43 13881
- [7] Goldberg M, Smirnov V, Ievlev V, et al. 2012 Inorg. Mater. 48 181
- [8] Kolekar T, Thorat N, Yadav H, Magalad V, Shinde M, Bandgar S, Kim J, Agawane G 2016 Ceram. Int. 42 5304
- [9] Murzakhanov F, Gabbasov B, Iskhakova K, et al. 2017 Magn. Reson. Solids 19 17207
- [10] Gafurov M R, Biktagirov T B, Mamin G V, Shurtakova D V, Klimashina E S, Putlyayev V I and Orlinskii S B 2016 Phys. Solid State 58 469
- [11] Biktagirov T, Gafurov M, Mamin G, Klimashina E, Putlayev V, Orlinskii S 2014 J. Phys. Chem. A 118 1519
- [12] Herklotz F, Lavrov E, Weber J, Mamin G, Kutin Y, Volodin M, Orlinskii S 2011 Phys. Status Solidi B 248 1532
- [13] Mukhambetov I, Lamberov A, Yavkin B, Gafurov M, Mamin G, Orlinskii S 2014 J. Phys. Chem.C 118 14998
- [14] Weng J., Liu X., Zhang X., Ji X. 1994 J. Mater. Sci. Lett. 13 159

## Multiferroicity of CuCrO<sub>2</sub> tested by ESR

Gotovko S.K., Svistov L.E.

P.L. Kapitza Institute For Physical Problems RAS, 119334, Kosygina st., Moscow, Russia

e-mail: sofyagotovko@gmail.com

CuCrO<sub>2</sub> an example of quasi-two-dimensional antiferromagnet ( $S = 3/2$ ) with triangular lattice structure.

Below  $T_N \approx 24$  K one side of the triangular lattice slightly distorts ( $\Delta a/a \approx 10^{-4}$ ); the neutron scattering experiments detected a three dimensional coplanar magnetic order with incommensurate wave vector  $\mathbf{q}_{ic} = (0.329, 0.329, 0)$  directed along the distorted side. According to the results of NMR and ESR investigations, spins form the spin planes with normal vector  $\mathbf{n}$ . For zero magnetic field  $\mathbf{H}$  normal vector  $\mathbf{n}$  of the spin plane is codirected with  $\mathbf{q}_{ic}$ . As three possible distortions of triangular lattice are possible, six magnetic domains occur in the sample. Orientation of the spin plane of magnetic structure is defined by strong easy axis anisotropy perpendicular to triangular plane and weak anisotropy perpendicular to one side of the triangle. One of the possible projection of spin plane is schematically shown in the inset in fig. 1 by bold red line (I), two other projections are shown with bold black lines (II and III).

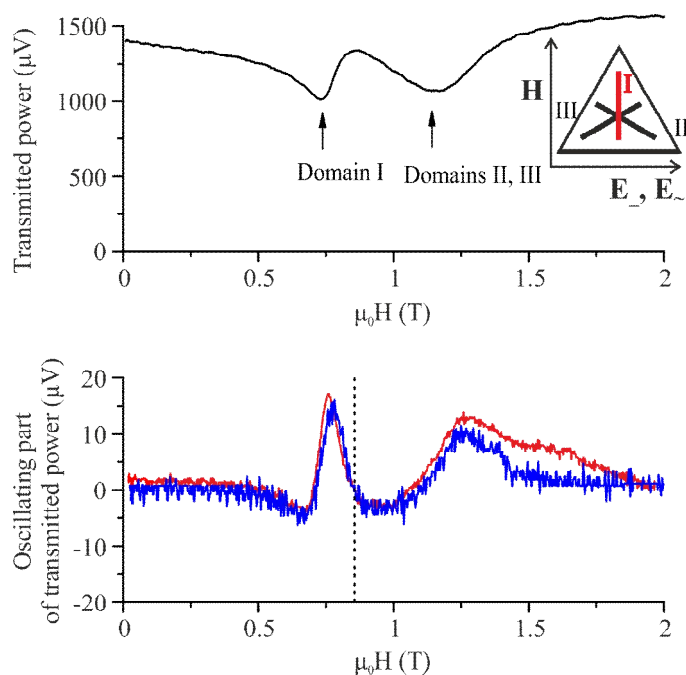


**Figure 1.** Top panel: Field scan of  $P_{tr}(H)$ . Bottom panel: field scan of the half-difference of  $P_{tr}(H)$ .  $E_{\sim} = 125$  kV/m,  $E_{\perp} = 500$  kV/m. The blue solid line shows a scaled field derivative of the transmitted power. Two different coefficients were used for scaling: one for  $H < 1.1$  T and the other for higher fields.  $\nu = 38.6$  GHz and  $T = 4.2$  K.

Simultaneously with the appearance of three-dimensional magnetic order, the sample acquires an electric polarization  $\mathbf{P} \approx 120$   $\mu\text{C}/\text{m}^2$ , which is perpendicular to the spin plane [1]. According to [2], main magnetoelectric properties of CuCrO<sub>2</sub> have a natural explanation in frame of Dzyaloshinski-Landau theory of magnetic phase transitions. Theory allows defining

of the eigenfrequencies of spin plane oscillations (ESR frequencies). Eigenfrequencies depend not only on external magnetic field  $\mathbf{H}$  but also on external electric field  $\mathbf{E}$ . External electric field  $\mathbf{E}$  leads to the shift of eigenfrequencies, and, correspondingly, to the shift of resonance magnetic field  $H_{res}$  at the constant frequency of generation. We report the results of the study of electric field influence on ESR frequency in  $\text{CuCrO}_2$ . The shift of frequencies by electric field is small, because of that we used the modulation technique, so we studied the alternating shift of frequency in presence of alternating electric field. In frame of the theory  $\Delta H_{res} = P \cdot E / 2\chi_{\perp} H_{res}$ , where  $\chi_{\perp}$  is the magnetic susceptibility of spin system at  $\mathbf{H}$  perpendicular to  $\mathbf{n}$ .

Alternating electric field  $E_{\sim}$  was applied to the sample at frequency  $\sim 300$  GHz. Mutual orientations of applied fields is shown in inset to fig.1 (upper panel). Transmitted through the resonator UHF-power  $P_{tr}(H)$  and its oscillating part  $P_{tr}^{\sim}(H)$  at the frequency of alternating field modulation were measured with the phase detection technique, so  $P_{tr}^{\sim}(H)$  is expected to have a shape of derivative of  $P_{tr}(H)$ . Experimental dependencies measured at  $T = 4.2$  K and generator frequency  $\nu = 38.6$  GHz are presented in fig. 1 (bottom panel).

Response  $P_{tr}^{\sim}(H)$ , measured with phase detection technique (red curve on bottom panel of fig.1), has a shape of derivative of transmitted power.  $P_{tr}(H)$  and  $P_{tr}^{\sim}(H)$  are measured in arbitrary but the same units. Constant electric field  $E_{\sim} = 500$  kV/m was used for electric monopolarization of the sample, so with the change of the sign of electric field the sign of electric polarization and the phase of response also changed. Measured dependencies, knowledge of ESR field–frequency spectra and the value of electric polarization allow comparing the value of the shift of frequencies in presence of electric field with the theoretically expected shift.

Expected curve of  $P_{tr}^{\sim}(H)$ , obtained by scaling of derivative of  $P_{tr}(H)$  with the coefficient calculated in frame of the theory [2], is presented in bottom panel of fig. 1 (blue curve). The results demonstrate an agreement with theoretical expectations of a phenomenological model. It was shown that the low-frequency dynamics of magnetically ordered  $\text{CuCrO}_2$  is defined by joint oscillations of the spin plane and electric polarization.

## References

- [1] K. Kimura, H. Nakamura, S. Kimura, M. Hagiwara, T. Kimura Tuning Ferroelectric Polarization Reversal by Electric and Magnetic Fields in  $\text{CuCrO}_2$  // Phys. Rev. Lett. 2009. V. 103. 107201.
- [2] V.I. Marchenko On Antiferromagnetic Transition in  $\text{CuCrO}_2$  // JETP 2014. V. 119. P. 1084.

**Resinous-asphaltene aggregates by NMR analysis**

D. Ivanov

Department of Physics, Kazan (Volga region) Federal University, Kazan 420111, Russian Federation

e-mail: f.ma.dima@mail.ru

Resins and asphaltenes primarily make the greatest contribution to the formation of solid-state structures in oil. Resins and asphaltenes are very important fractions of crude oil, oil residues, and bitumen. The tendency of asphaltenes to aggregate distinguishes them from other components of oil. Aggregation of asphaltenes can cause complex nonlinear effects in the rheological processes characteristic of asphaltene-containing solutions, including oil and water-oil emulsions. In turn, the anomalies of the rheological properties of oil cause the latter to be classified as non-Newtonian fluids.

A promising approach for solving this problem is the use of the nuclear magnetic resonance (NMR) method [1]. The choice of NMR as a physical method for studying such complex systems as oil is not accidental and is due to a number of undeniable advantages: the method is non-destructive, sensitive to the component composition of the object under study, and the possibility of research directed at the site of the object under investigation [2, 3].

Summarizing the experimental results obtained in this paper, it can be concluded that the use of the NMR method makes it possible to characterize the state of asphaltene aggregates. It is shown that the size of a resinous-asphaltene coat directly depends on the size of aggregates of asphaltenes.

The work was supported by the scholarship program of British Petroleum in the promising areas of development of the oil and gas industry.

**References**

- [1] LaTorraca G.A. Low-field NMR determinations of the properties of heavy oils and water-in-oil emulsions // *Magnetic Resonance Imaging*. – 1998. – V. 16. – №. 5. – P. 659-662.
- [2] Yang Z., Hirasaki G.J. NMR measurement of bitumen at different temperatures // *Journal of Magnetic Resonance*. – 2008. – V. 192. – №. 2. – P. 280-293.
- [3] Sun B. In situ fluid typing and quantification with 1D and 2D NMR logging // *Magnetic resonance imaging*. – 2007. – V. 25. – №. 4. – P. 521-524.

## Contributions of different parts of dipole-dipole interactions to relaxation of multiple quantum NMR coherences in a single crystal of calcium fluorapatite

G.A. Bochkin<sup>1</sup>, E.B. Fel'dman<sup>1</sup>, I.D. Lazarev<sup>1,2</sup>, S.G. Vasil'ev<sup>1</sup>

<sup>1</sup>Institute of Problems of Chemical Physics, Chernogolovka, Moscow Region, 142432, Russia

<sup>2</sup>Lomonosov Moscow State University, Faculty of Physics and Chemistry, Moscow, 119991, Russia

e-mail: the.ilia.lazarev@gmail.com

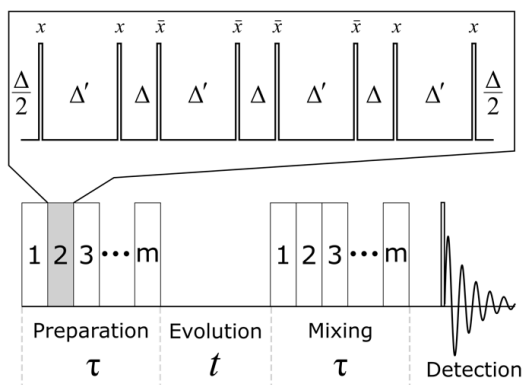


**Figure 1.** Scheme of the MQ NMR experiment;  $\tau$  is the duration of the preparation and mixing periods;  $t$  is the durations of the free evolution period. The basic cycle of the multipulse sequence, consisting of eight  $\pi/2$ -pulses with the duration  $t_p$  separated by delay  $\Delta$  and  $\Delta' = 2\Delta + t_p$  is repeated  $m$  times for obtaining the necessary time  $\tau = 12m(\Delta + t_p)$ ;  $m$  is a natural number.

problem was not clear until now.

We investigated numerically the dependence of the second moment  $M_2^n$  of the line shape of the MQ NMR coherence of order  $n$  ( $n = 0, \pm 2$ ) on the number of spins both for the  $zz$  model ( $M_2^{(n)}(H_{zz})$ ) and for the  $H_{dz}$  interaction ( $M_2^{(n)}(H_{dz})$ ) in homonuclear systems.

In fig.2 the ratios of  $\frac{M_2^{(n)}(H_{zz})}{M_2^{(n)}(H_{dz})}$  ( $n = 0, \pm 2$ ) are presented for 6-18 spins. One can see that

the ratio  $\frac{M_2^{(n)}(H_{zz})}{M_2^{(n)}(H_{dz})}$  increases with the growth of the number  $N$  of spins. We proved that the

flip-flop part of  $H_{dz}$  does not contribute to the  $M_2^0$  in the approximation of the nearest neighbor interactions for  $N \gg 1$ . At the same time the flip-flop part of the DDI is significant

Multiple quantum (MQ) NMR [1] (fig.1) not only creates MQ coherences but allows also to investigate their relaxation [2]. MQ NMR coherences emerge on the preparation period of the MQ NMR experiment, and their relaxation occurs on the evolution period [1]. Dipolar relaxation of MQ NMR coherences can be considered as the simplest model of decoherence of many-qubit coherent clusters [3]. An investigation of decoherence in such clusters is very important for quantum devices (in particular, for quantum computers).

Relaxation of MQ NMR coherences in one-dimensional systems was studied with the second moments of the line shapes of MQ coherences of different orders [2, 4]. Recently the investigation of the dipolar relaxation of MQ NMR coherences in spin chains was performed using the  $zz$  model [5] in which the flip-flop part of the dipole-dipole interactions [6] is neglected on the evolution period of the MQ NMR experiment. However, the applicability of the  $zz$  model to the considered

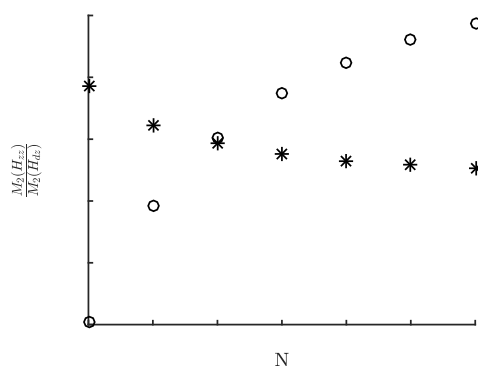


**Figure 3.** The dependence of the ratio of the second moments  $\frac{M_2^{(0)}(H_{zz})}{M_2^{(2)}(H_{zz})}$  for the line shapes  $H_{zz}$  and  $H_{xz}$  interactions on the spin chain length (circles denote the ratio  $\frac{M_2^{(0)}(H_{zz})}{M_2^{(2)}(H_{zz})}$  of the MQ NMR coherences of orders  $n = 0, 2$  on the number of spins for the system with stars denote the ratio  $\frac{M_2^{(0)}(H_{zz})}{M_2^{(2)}(H_{zz})}$ ;  $D\tau = 2$ ).

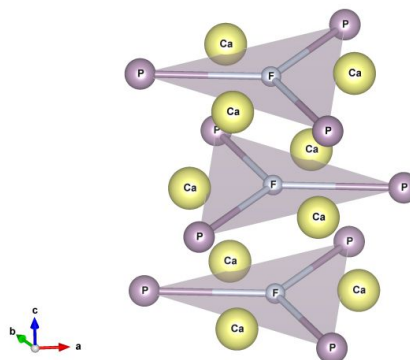


**Figure 3.** Part of the crystal structure of the fluorapatite  $\text{Ca}_5(\text{PO}_4)_3\text{F}$  showing surroundings of the fluorine atoms. Oxygen atoms have been removed for clarity. Fluorine atoms are equally spaced ( $r_{\text{FF}} = 344$  pm) and arranged in columns along the c-axis of the crystal. Every fluorine atom is surrounded by three equidistant phosphorus atoms ( $r_{\text{FP}} = 367.3$  pm) situated in vertexes of equilateral triangles in the planes perpendicular to the c-axis.

for the second moment  $M_2^{\pm 2}$  of the line shape of the MQ NMR coherence of the plus/minus second order.

The experimental investigation of MQ NMR dynamics and relaxation were performed on a single crystal of calcium fluorapatite  $\text{Ca}_5(\text{PO}_4)_3$  [2]. The structure of this crystal

contains parallel chains of  $^{19}\text{F}$  atoms (nuclear spin  $1/2$ ) arranged along the c-axis. The distance between neighboring chains is about three times larger than the distance between adjacent fluorine atoms in a chain [7, 8]. As a result, the system can be considered as a set of isolated spin chains. An isolated spin chain is the underlying model for the theoretical description of the spin dynamics on the preparation period of the MQ NMR experiment [1]. Every F atom in calcium fluorapatite is surrounded by three P atoms at the same distance. All these four atoms lie in the same plane perpendicular to the chains of F atoms and, accordingly, to the c-axis. The arrangement of atoms in fluorapatite is shown in fig.2 (the image was prepared using VESTA software [9]). The specially tailored multi-pulse sequence which irradiates  $^{19}\text{F}$  spins on the preparation period of the MQ NMR experiment [1] eliminates the heteronuclear interactions of  $^{31}\text{P}$  ( $s = 1/2$ ) and  $^{19}\text{F}$  spins. However, such averaging does not occur on the evolution period of the experiment [1] since the irradiation is absent. The role of the heteronuclear interactions in the dipolar relaxation of MQ NMR coherences is not clear so far.

Relaxation of MQ NMR coherences is caused by the secular (with respect to the external magnetic field directed along the z axis) dipole-dipole interactions (DDI). In order to simplify an investigation of the relaxation process with the full DDI Hamiltonian we restrict ourselves to the  $zz$  part of  $H_{ddz}$ , neglecting its flip-flop part. For a linear chain of  $^{19}\text{F}$  spins,

when every  $^{19}\text{F}$  spin interacts with three  $^{31}\text{P}$  spins ( $s = 1/2$ ):

$$H_{zz} = 2 \sum_{i < j} D_{ij} I_i^z I_j^z + 2 \sum_i \sum_{j=1}^3 J_{ij} I_i^z S_{ij}^z, \quad (1)$$

where  $D_{ij}$  is the coupling constant of fluorine spins  $i$  and  $j$ ,  $D_{i,i+1} = D$ ;  $J_{ij}$  ( $i = 1, \dots, N$ ;  $j = 1, 2, 3$ ) is the dipolar coupling constant of fluorine spin  $i$  and phosphorus spin  $j$ , and  $S_{ij}^z$  is the

$z$ -projection of the angular spin moment of phosphorus spin  $j$  ( $j = 1, 2, 3$ ) interacting with fluorine spin  $i$  ( $i = 1, 2, \dots, N$ ). The density matrix of the system  $\rho(\tau)$  at the time moment  $\tau$  of the preparation period was obtained from exact solutions for MQ NMR dynamics [10, 11].

Since we have a system consisting of  $4N$  spins ( $N$  fluorines and  $3N$  phosphorus), the intensity  $F_0(\tau, t)$  and  $F_{\pm 2}(\tau, t)$  the MQ NMR coherence of the zeroth order during the evolution period at the time moment  $t$  is

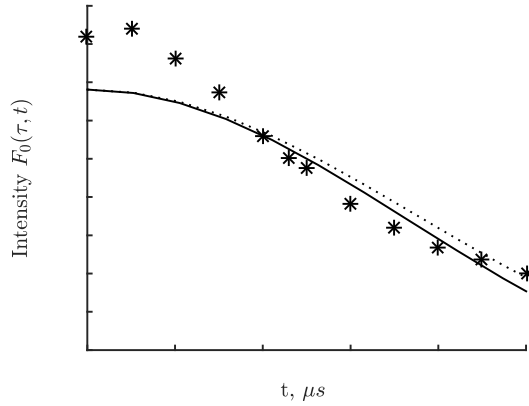


**Figure. 5** The experimental and theoretical intensities of the MQ NMR coherence of the zeroth order on the evolution period of the MQ NMR experiment for  $N = 100$  spins in the chain and the duration of the preparation period is  $\tau = 126 \mu s$ . The solid line is the theoretical results obtained with Eq.(2); the dotted line is the theoretical results obtained without accounting for the heteronuclear interactions [5]. The points are the experimental values of the intensity of the MQ NMR coherence of the zeroth order for a quasi-one-dimensional chain of  $^{19}\text{F}$  nuclear spins in a single crystal of calcium fluorapatite.

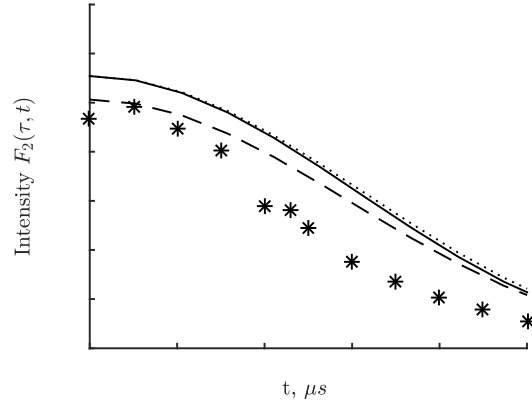


**Figure. 5** The experimental and theoretical intensities of the MQ NMR coherence of the second order on the evolution period of the MQ NMR experiment for  $N = 100$  spins in the chain and the duration of the preparation period  $\tau = 139.2 \mu s$ . The solid line is the theoretical results obtained with Eq.(3); the dot-line is the theoretical results obtained without an account of the heteronuclear interactions [5]. The dashed line is the results of numerical calculations of the MQ NMR coherence of the second order for a system consisting of 12 spins. The points are experimental values of the intensity of the MQ NMR coherence of the second order for a quasi-one-dimensional chain of  $^{19}\text{F}$  nuclear spins in a single crystal of calcium fluorapatite.

$$F_0(\tau, t) = \frac{4 \cos^3(Jt)}{N(N+1)^2} \sum_{i, i' = 2, 4, \dots, N \text{ or } i, i' = 1, 3, \dots, N-1} \left( \prod_{i \neq i'} \cos[(D_{ii'} - D_{ii})t] \right) \times$$

$$\left( \sum_k \sin(kl) \sin(kl') e^{-2iDl \cos(k)} \right)^2 \quad (1)$$

$$F_{\pm 2}(\tau, t) = -\frac{4 \cos^6(J\tau)}{N(N+1)^2} \sum_{i=1,3,\dots,N-1 \text{ or } i'=2,4,\dots,N} \left( \prod_{i \neq l, i \neq l'} \cos[(D_{i'} - D_{ii})t] \right) \times$$

$$\left( \sum_k \sin(kl) \sin(kl') e^{-2iDl \cos(k)} \right)^2 \quad (1)$$

One can see in fig.4 and fig.5 that accounting for the heteronuclear interactions significantly improves the agreement of the theoretical results with the experimental data.

Although in fig.5 the agreement between the experimental and theoretical results is improved when the heteronuclear contributions are considered, discrepancy between the theoretical and experimental data is bigger than in fig.4. It is possible the discrepancy is mostly due to neglecting the flip-flop part of the DDI in the  $zz$  model. Indeed, one can see from fig.2 that the flip-flop part of the DDI is getting more significant with increasing number of spins. We performed numerical calculation of the intensity of the MQ NMR coherence of the second order for a system consisting of 12 spins. fig.5 demonstrates that even for this system with a small number of spins the numerical results are in better agreement with the experimental data than the predictions of the  $zz$  model.

## References

- [1] J.Baum, M.Munowitz, A.N.Garroway, and A. Pines, Multiple-quantum dynamics in solidstate NMR, *J. Chem. Phys.* 83, 2015–2025 (1985).
- [2] G.Kaur, A.Ajoy, P.Cappellaro, Decay of spin coherences in onedimensional spin systems, *New J.Phys.* 15 (2013) 093095.
- [3] G.A. Bochkin, E.B. Fel'dman, S.G. Vasil'ev, V.I. Volkov, Dipolar relaxation of multiple quantum coherences as a model of decoherence of many-qubit coherent clusters, *Appl.Magn.Reson.* 49 (2018) 25–34.
- [4] S.I. Doronin, E.B. Fel'dman, I.I. Maximov, Line shapes of multiple quantum NMR coherences in one-dimensional quantum spin chains in solids, *J.Magn.Reson.* 171(2004) 47–42.
- [5] G.A. Bochkin, E.B. Fel'dman, S.G.Vasil'ev, V.I. Volkov, Dipolar relaxation of multiple quantum NMR coherences in one-dimendional systems, *Chem. Phys. Lett.* 680(2017) 56–60.
- [6] A.Abragam, *The principles of nuclear magnetism.* Oxford. Clarendon Press, 1961.
- [7] M.Braun, C.Jana,  $^{19}\text{F}$  NMR spectroscopy of fluoridated apatites, *Chem.Phys.Lett.* 245 (1995) 19–22.
- [8] N.Leroy, E.Bres, Structure and substitutions in fluorapatite, *Eur.Cells Mater.* 2 (2001), 36–48
- [9] K.Momma, F.Izumi, VESTA 3 for three-dimensional visualization of crystal, volumetric and morphology data, *J.Appl.Crystallogr.* 44 (2011) 1272–1276.
- [10] E.B.Fel'dman, S.Lacelle, Multiple quantum NMR spin dynamics in one-dimensional quantum spin chains, *Chem.Phys.Lett.* 253(1996) 27–31.
- [11] S.I.Doronin, I.I. Maksimov, E.B. Fel'dman, Multiple-quantum dynamics of one-dimensional nuclear spin systems in solids, *J. Exp. Theor. Phys.* 91(2000) 597–609.

## Investigation of YVO<sub>4</sub> monocrystals doped by <sup>143</sup>Nd<sup>3+</sup> and <sup>145</sup>Nd<sup>3+</sup> rare earth ions by EPR and crystal-field parameters calculations.

R. F. Likero<sup>1</sup>, I. V. Yatsyk<sup>1,2</sup>, R. M. Eremina<sup>1,2</sup>, Yu. D. Zavartsev<sup>2,3</sup>, A. S. Kutovoi<sup>2,3</sup>

<sup>1</sup>Kazan (Volga region) Federal University, 420008, Kremlevskaya st. 18, Kazan, Russia

<sup>2</sup>Zavoisky Physical-Technical Institute, Federal Research Center “Kazan Scientific Center of RAS”, 420029, Sibirsky trakt 10/7, Kazan, Russia

<sup>3</sup>Prokhorov General Physics Institute, Russian Academy of Sciences, 119991, Vavilova St., 38, Moscow, Russia

e-mail: [rodionlikero@gmail.com](mailto:rodionlikero@gmail.com)

### Introduction

Isotopically pure rare-earth ions doped into dielectric crystal are currently considered as perspective materials for quantum memory application [1]. For example, odd neodymium isotopes (<sup>143</sup>Nd and <sup>145</sup>Nd) doped into yttrium orthovanadate monocrystal (YVO<sub>4</sub>). These crystals are already in use in laser systems (but with natural abundance of RE ions). Since rare-earth elements forming paramagnetic centers in this crystal, it can be studied by electron paramagnetic resonance method which allows to determine values of g-tensor, A-tensor of hyperfine structure and crystal field parameters.

The first paper about investigation of Stark levels of Nd impurity centers in YVO<sub>4</sub> was published in 1968 [2] and EPR data were presented in [3]. The energy level scheme was obtained and 25 from 26 ground term levels were identified [4]. The crystal-field analysis and investigation of the polarization and relative intensities of transition between the sublevels <sup>4</sup>F<sub>3/2</sub> to <sup>4</sup>I<sub>13/2</sub>, <sup>4</sup>I<sub>11/2</sub>, <sup>4</sup>I<sub>9/2</sub> in Nd<sup>3+</sup>:YVO<sub>4</sub> crystals have been performed, where Nd<sup>3+</sup> ions occupy positions with point symmetry D<sub>2d</sub> [5].

For effective quantum memory usage of RE ions with nonzero nuclear spin is required. The presence of other isotopes (including those with zero nuclear spin) is undesirable, because contribution of these isotopes into useful signal is rather small. Also, their presence will shorten phase time of active ions due to spin-spin interaction. In the paper [6] it was shown that optical pumping of the hyperfine levels in isotopically enriched <sup>145</sup>Nd<sup>3+</sup>:Y<sub>2</sub>SiO<sub>5</sub> crystals is more efficient, owing to the longer population relaxation times of hyperfine levels. By optically cycling the population many times through the excited state a nuclear spin flip can be forced in the ground state hyperfine manifold, in which case the population is trapped for several seconds before relaxing back to the pumped hyperfine level.

### Samples and experiments

Neodymium doped YVO<sub>4</sub> crystals were grown by the Czochralski method in Ir crucibles in the 99 vol.% Ar + 1 vol.% O<sub>2</sub> atmosphere. The purity of primary components, i.e. V<sub>2</sub>O<sub>5</sub> and Nd<sub>2</sub>O<sub>3</sub> was no worse than 99.75%. We studied three YVO<sub>4</sub> monocrystals doped with: 0.001 at. % <sup>143</sup>Nd<sup>3+</sup>, 0.005 at. % <sup>143</sup>Nd<sup>3+</sup> and 0.005 at. % <sup>145</sup>Nd<sup>3+</sup>. YVO<sub>4</sub> belongs to the I4<sub>1</sub>/amd space group [7] with the following unit cell parameters: a = b = 7.118(0) Å, c = 6.289(0) Å. The direction of the axes in the crystal was determined from X-ray diffraction analysis. The crystal was cut perpendicular to the b axis. Then, main crystallographic directions were chosen for further measurements.

The electron configuration of Nd<sup>3+</sup> ions is 4f<sup>3</sup> with the main ground state <sup>4</sup>I<sub>9/2</sub>. The quantum properties of these ions are described by Kramers theorem which states that

eigenstate of Kramers ion are at least doublefold degenerate. Because of that, calculations were done in approximation of effective spin  $S_{\text{eff}} = 1/2$ . Hamiltonian, which contains  $g$ -tensor and  $A$ -tensor is shown below:

$$\mathcal{H} = \mathbf{SAI} + g\beta\mathbf{HS}_{\text{eff}} \quad (1)$$

Typical EPR spectrum for (0.005% at.)  $^{143}\text{Nd}^{3+}$  in  $\text{YVO}_4$  is shown at fig. 1. We observe 8 lines ( $I = 7/2, 2I+1$ ) of the hyperfine structure on EPR spectra of  $^{143}\text{Nd}$  and  $^{145}\text{Nd}$ . Angular dependencies of resonance magnetic fields of EPR signals in  $^{143}\text{Nd}^{3+}:\text{YVO}_4$  monocrystal rotated in (ac) and (ab) – planes were obtained on X-band EPR spectrometer Bruker EMX+ at  $T = 15$  K. The angular dependence of resonance magnetic field is shown at fig. 2 for (0.005% at.)  $^{143}\text{Nd}^{3+}:\text{YVO}_4$ , crystal rotated in (ac) - plane.

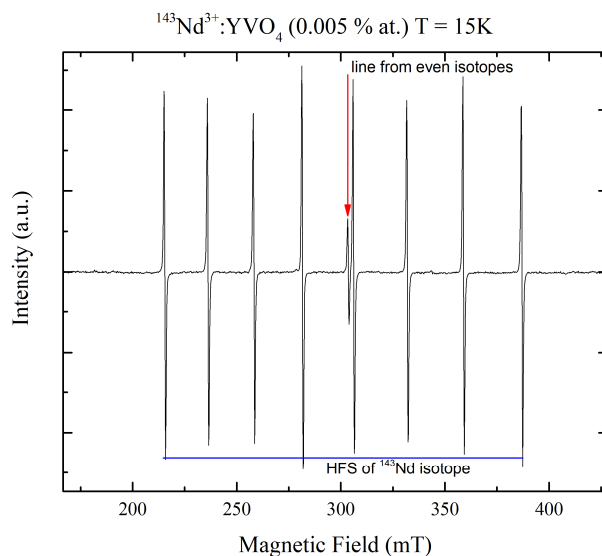


**Figure 1.** EPR spectrum of  $^{143}\text{Nd}^{3+}:\text{YVO}_4$  (0.005% at.) recorded in (ac)-plane at 15 K, microwave frequency  $\nu = 9.63919$  GHz

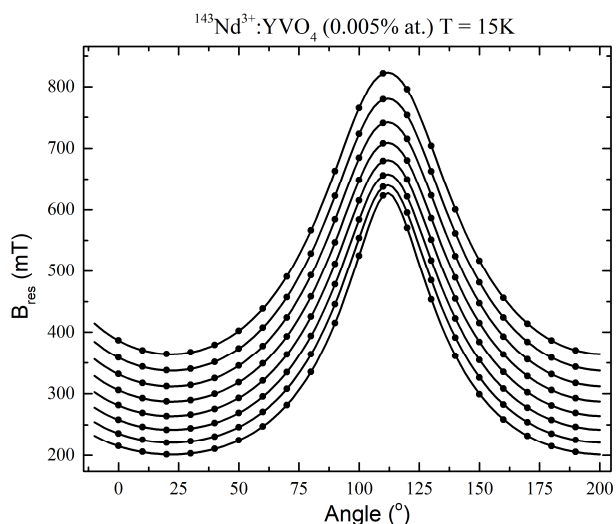


**Figure 2.** Angular dependence of resonance magnetic fields of EPR signal for  $^{143}\text{Nd}^{3+}:\text{YVO}_4$  (0.005% at.), rotated in (ac)-plane at  $T = 15$  K, microwave frequency  $\nu = 9.63919$  GHz

### Crystal field parameters calculation

Crystal-field parameters of Nd ions in GdVO<sub>4</sub> and YVO<sub>4</sub> were obtained by Anderson et. al [8] from fitting Stark levels scheme. Crystal-field calculations and optical spectra measurements for Nd doped YMO<sub>4</sub> laser hosts (M = V, P, As) were performed by Guillot et. al [7]. Y<sup>3+</sup> ions are eightfold coordinated by oxygen ions, forming [YO<sub>8</sub>] dodecahedra and they are located in positions with a D<sub>2d</sub> site symmetry. Nd<sup>3+</sup> ions are replacing Y<sup>3+</sup> ions in these positions, forming paramagnetic centers. The Nd<sup>3+</sup> ion has a 4f<sup>3</sup> electronic configuration and <sup>4</sup>I<sub>9/2</sub> ground multiplet state. The crystal-field splits the J = 9/2 multiplet into twofold degenerate levels. Since Y<sup>3+</sup> sites have D<sub>2d</sub> site symmetry, CF Hamiltonian have the following structure in crystallography coordinate system:

$$\mathcal{H} = B_2^0 O_2^0 + B_4^0 O_4^0 + B_6^0 O_6^0 + B_4^4 O_4^4 + B_6^4 O_6^4 \quad (2)$$

Crystal-field parameters  $B_k^q$  for Nd<sup>3+</sup> ions in YVO<sub>4</sub> were fitted for the best coincidence of calculated and measured values of the Stark energy levels and components of g-tensor, presented in Table 2. In addition, the parameters of the crystal-field determined in the papers [5], [7] are given in Table 2.

**Table 2.** Experimentally obtained and theoretically calculated values of crystal field parameters, g-factors and electron energy levels of Nd<sup>3+</sup> ion in YVO<sub>4</sub>.

	Experiment	Our calculations	Guillot-Noel <sup>b</sup>	Zundu <sup>c</sup>
$B_2^0$	-	54.3	-312	-14.7
$B_4^0$	-	164.2	476	219.6
$B_4^4$	-	-568.3	-1405	-602.2
$B_6^0$	-	66.9	-924	-318.2
$B_6^4$	-	-260.3	-237	39.5
g <sub>x</sub>	2.358	2.349 ± 0.005	2.361 ± 0.003	-
g <sub>y</sub>	2.358	2.349 + 0.005	2.361 ± 0.003	-
g <sub>z</sub>	0.915	0.914 ± 0.005	0.915 ± 0.004	-
$\epsilon_0(\text{cm}^{-1})$	0 <sup>a</sup>	0	0	0
$\epsilon_1(\text{cm}^{-1})$	108 <sup>a</sup>	124	130	152.9
$\epsilon_2(\text{cm}^{-1})$	173 <sup>a</sup>	215	197	202.6
$\epsilon_3(\text{cm}^{-1})$	226 <sup>a</sup>	344	243	231
$\epsilon_4(\text{cm}^{-1})$	433 <sup>a</sup>	428	453	452.1

<sup>a</sup> data from Ref. [2]; <sup>b</sup> data from Ref. [7]; <sup>c</sup> data from Ref. [5]

We used extended Stevens operators, in the [7] Wybourne notation and in [5] Butler's notation was used. The two major types of operators, i.e. the Stevens and Wybourne ones used to express the crystal-field Hamiltonians, the relationship between the crystal-field parameters in the two notations can be found in the review [9]. Only the lowest doublet of the Nd<sup>3+</sup> ground multiplet is populated at low temperatures, so the magnetic properties of the system can be described by the Kramers doublet with effective spin  $S_{\text{eff}} = 1/2$  spin.

### Conclusion

The crystal-field parameters for Nd<sup>3+</sup> were defined from analysis of Stark energy levels and experimental g- tensor value.

### Acknowledgments

This work was supported by the Russian Science Foundation (project no.16-12-00041).

## PROCEEDINGS

### References

- [1] C.W. Thiel, Th. Bottger, R.L. Cone, Rare-earth-doped materials for applications in quantum information storage and signal processing, *J. Lumin.* 131 (2011) 353-361.
- [2] Kh. Bagdasarov, G. Bogomolova, A. Kaminskii, V. Popov, *Dokl. Akad. Nauk. USSR* 180 (1968) 1347
- [3] U. Ranon, Paramagnetic Resonance of  $\text{Nd}^{3+}$ ,  $\text{Dy}^{3+}$ ,  $\text{Er}^{3+}$  and  $\text{Yb}^{3+}$  in  $\text{YVO}_4$ , *Physics Letters* 28A (1968) 228-229
- [4] N. Karyanis, C.A. Morrison, D.E. Wortman, Analysis of the ground term energy levels for triply ionized neodymium in yttrium orthovanadate, *J. Chem. Phys.* 10 (1975) 4125-4129.
- [5] L. Zundu, H. Yidong, Crystal-field analysis of the energy levels and spectroscopic characteristics of  $\text{Nd}^{3+}$  in  $\text{YVO}_4$ , *J. Phys.: Condens. Matter* 6 (1994) 3737-3748.
- [6] E. Z. Cruzeiro, A. Tiranov, J. Lavoie, A. Ferrier, P. Goldner, N. Gisin, M. Afzelius, Efficient optical pumping using hyperfine levels in  $^{145}\text{Nd}^{3+}:\text{Y}_2\text{SiO}_5$  and its application to optical storage, *New J. Phys.* 20 (2018) 053013.
- [7] O. Guillot-Noel, A. Kahn-Harari, B. Viana, D. Vivien, E. Antic-Fidancev, P. Porcher, Optical spectra and crystal-field calculations of  $\text{Nd}^{3+}$  doped Zircon-type  $\text{YMO}_4$  laser hosts ( $M = \text{V}, \text{P}, \text{As}$ ), *J. Phys.: Condens. Matter* 10 (1998) 6491-6503.
- [8] F.G. Anderson, P.L. Summers, H. Weidner, P. Hong, R.E. Peale, *Phys. Rev. B* 50 (1994-II) 14802-14808.
- [9] C. Rudowicz, M. Karbowski, Disentangling intricate web of interrelated notions at the interface between the physical (crystal-field) Hamiltonians and the effective (spin) Hamiltonians, *Coordination Chemistry Reviews* 287 (2015) 28-63.

## Analysis and interpretation of ENDOR spectra of LiYF<sub>4</sub> crystal activated with rare-earth ions

K.M. Makushin, G.V. Mamin, M.R. Gafurov, S.B. Orlinskii, I.N. Kurkin, E.I. Baibekov

Kazan Federal University, 420008, Kremlyovskaya Str. 18, Kazan, Russian Federation

e-mail: [lconstantinel@gmail.com](mailto:lconstantinel@gmail.com)

A special interest for spectral study of the double fluorides LiY<sub>1-x</sub>R<sub>x</sub>F<sub>4</sub>, where R is the impurity rare-earth ion, originates from their frequent use in quantum electronics, solid-state lasers and sensors.

Usually, the electron paramagnetic resonance spectra do not provide full information about the hyperfine interactions in the crystal because of high inhomogeneous broadening of the resonance lines [1]. This difficulty is overcome in case of electron-nuclear double resonance (ENDOR) studies.

This work represents an analysis and interpretation of ENDOR spectra of trivalent rare-earth ions R<sup>3+</sup>, which substitute Y<sup>3+</sup> ions in LiYF<sub>4</sub> single crystal. The spectra of Nd<sup>3+</sup>, U<sup>3+</sup>, Ce<sup>3+</sup> ions obtained by the Mims method, were investigated. LiYF<sub>4</sub> crystal has scheelite structure and local tetragonal symmetry at the position of Y ion. The experiment was conducted at X band (9.6 GHz), the magnetic field was perpendicular to crystal c axis. The concentration of the rare-earth impurity ions was of the order of 0.01 at. %.

The results can be described with the following Hamiltonian [2]

$$H_{\text{eff}} = \mu_B \sum_{kj} g_{kj} B_k S_j + \hbar \gamma \sum_{ik} \left( -B_k + \sum_j T_{kj}^{(i)} S_j \right) I_k^{(i)}, \quad (1)$$

where  $B$  – external RF magnetic field,  $S$  – electron spin,  $I$  – nuclear spin,  $T$  – the super hyper-fine interaction (SHFI) parameters and  $g_{kj}$  – g-tensor components. One can partially diagonalize the above Hamiltonian on the electron states  $|\pm M\rangle$ , since the electron part of Zeeman interaction exceeds much the hyperfine interaction energy

$$H_{\text{lig}}(\pm M) = \langle \pm M | H_{\text{eff}} | \pm M \rangle = \pm \frac{g \mu_B B}{2} + \sum_i H^{(i)}(\pm M), \quad (2)$$

where

$$H^{(i)}(\pm M) = \hbar \gamma \left( -B_k + \frac{1}{2} T_{kj}^{(i)} \lambda_j \right) I_k^{(i)} = \mathbf{B}_{\text{eff}}^{(i)}(\pm M) \mathbf{I}^{(i)}, \quad (3)$$

$$B_{\text{eff}}^{(i)}(\text{p}) = \hbar \gamma \left( -B_k \pm \frac{1}{2g} T_{kj}^{(i)} g_{rj} \lambda_r \right). \quad (4)$$

The parameter  $g = \sqrt{\lambda_k \lambda_j g_{kn} g_{jn}}$ , introduced above, is an effective g-factor,  $\lambda(\theta, \varphi) = \frac{\mathbf{B}}{B}$  – direction cosine.

The task reduces to diagonalization of separate Hamiltonians (3) corresponding to different ligands. In the calculations of  $T_{kj}$ , two contributions were considered: magnetic dipole interaction and charge-transfer contribution.

Because  $^{19}\text{F}$  ligands are situated at distances  $\sim 2 \text{ \AA}$  from paramagnetic ion, one cannot neglect overlapping of their electronic wave functions. Electrons from  $2p$  or  $2s$  shell of  $\text{F}^-$  ion partially transfer to  $4f$  shell of rare-earth paramagnetic ion, as a result we have hybrid mixed shell – molecular orbital. When the wave functions of  $2p$  and  $2s$  shells are mixed with  $4f$  shell of the rare earth ion, additional interaction of its electronic shell and nuclear spin of  $\text{F}^-$  appears (Fermi contact interaction). Since the  $4f$  electronic shell is quite compact, the overlapping is negligible at distances over  $3 \text{ \AA}$ . In particular, this contribution wasn't considered for  $^7\text{Li}$ . Because of  $^7\text{Li}$  nuclear spin  $I = \frac{3}{2}$ , one must take to account the quadrupole interaction with the electric field gradient (EFG) of the crystal. Besides, EFG is able to polarize the electronic shells of  $^7\text{Li}$ , so additional EFG on the site of the nuclear spin appears. The corresponding quadrupole interaction can be written as follows:

$$H_Q = (1-\eta)eQV_{zz} \frac{3I_z^2 - I(I+1)}{4I(2I-1)} \quad (5)$$

or

$$H_Q = \alpha I_z^2 - \beta E, \quad (6)$$

where  $E$  – is the identity operator,  $\alpha = \frac{(1-\eta)eQV_{zz}}{4}$ ,  $\beta = 5\frac{(1-\eta)eQV_{zz}}{16}$  and  $(1-\eta)$  – antishielding factor [3], [4]. The magnitude of quadrupole momentum of  $^7\text{Li}$  equals  $Q = -4.1 \cdot 10^{-27} \text{ cm}^2$  in units of the elementary charge. The longitudinal component of EFG,  $V_{zz}$ , was calculated by summation over the crystal lattice. The numerical calculation gives the value  $\alpha = 0.0859 \text{ MHz}$ .

Since Zeeman and SHF interaction prevail over  $H_Q$ , one can obtain the ENDOR frequency shifts using the first-order perturbation theory.

The results of the calculations, as well as the experimental ENDOR spectra of  $\text{Nd}^{3+}$ ,  $\text{U}^{3+}$  and  $\text{Ce}^{3+}$  ions in the frequency domain of  $^7\text{Li}$ , are shown below.

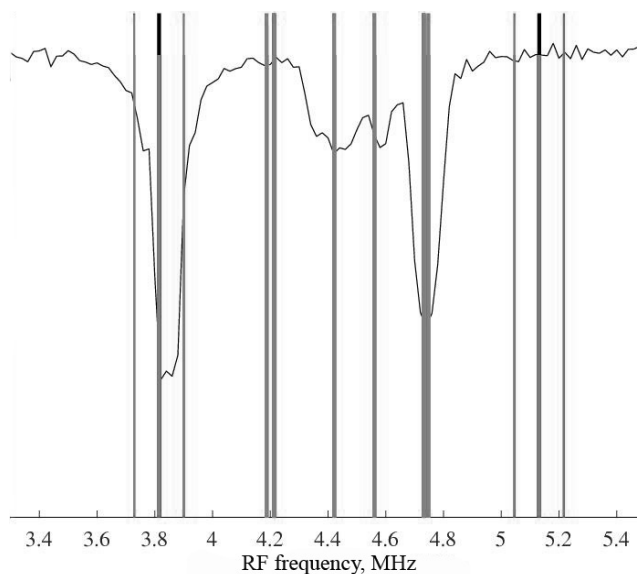


**Figure 1.** The experimental Mims ENDOR spectrum of  $\text{Nd}^{3+}$  ion. The calculated frequencies of transitions are shown with vertical lines.

## PROCEEDINGS

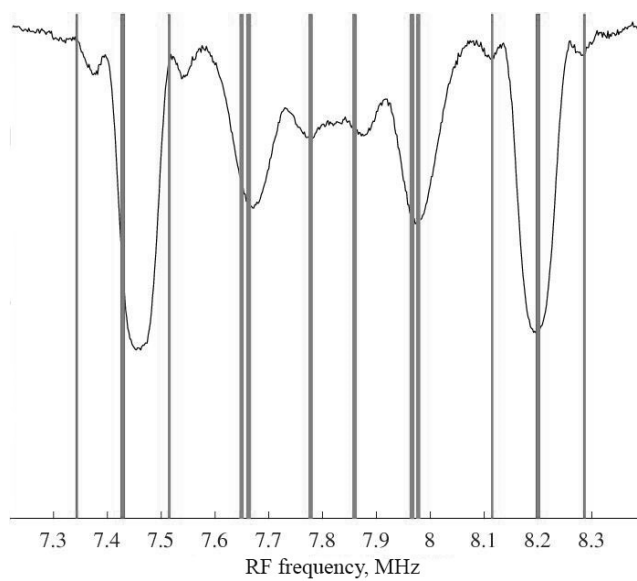


**Figure 2.** The experimental Mims ENDOR spectrum of ion  $\text{Ce}^{3+}$ . The calculated frequencies of transitions are marked with vertical lines.

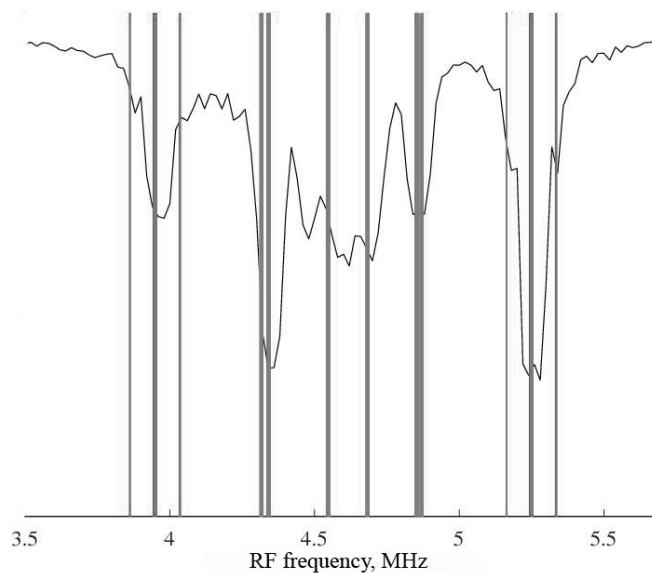


**Figure 3.** The experimental Mims ENDOR spectrum of ion  $\text{U}^{3+}$ . The calculated frequencies of transitions are marked with vertical lines.

As can be seen from the resulting data, good conformity between experimental and calculated spectra is observed.

**References**

- [1] C.P. Slichter, Principles of magnetic resonance. Vol. 1. Springer Science & Business Media, (2013).
- [2] L.K. Aminov, I.N. Kurkin, B.Z. Malkin, Superhyperfine structure in the EPR spectra and optical spectra of impurity f ions in dielectric crystals. Fizika Tverdogo Tela, (2013), Vol. 55, No. 7, pp. 1249–1267.
- [3] J.R. Anderson, Determination of sternheimer antishielding factor of  $li^7$  in lithium fluoride by acoustic nuclear magnetic resonance. Physical Review B, (1971), Vol. 5, P. 4334–4341.
- [4] M.H. Cohen, Quadrupole effects in nuclear magnetic resonance studies of solids, Elsevier, (1957), Vol. 5, P. 321–438.

## High-field T<sub>2</sub> MRI contrast agent based on TbF<sub>3</sub> and DyF<sub>3</sub> nanoparticles

E.M. Alakshin<sup>1</sup>, A.V. Bogaychuk<sup>1</sup>, V.V. Kuzmin<sup>1</sup>, A.V. Klochkov<sup>1</sup>, E.I. Kondrateva<sup>1</sup>,  
I.K. Nekrasov<sup>1</sup>, M.S. Tagirov<sup>1,2</sup>

<sup>1</sup> Kazan Federal University, 420008, Kazan, Russian Federation,

<sup>2</sup> Institute of Applied Research, 420111, TAS, Kazan, Russian Federation

e-mail: igor05071997@mail.ru

Magnetic resonance imaging as a method of non-invasive imaging has extremely high penetration depth of tissue. Moreover, MRI doesn't use radioactive agents or high-energy electromagnetic waves as in the case of PET, SPECT and CT. It is known, the time of nuclear magnetic relaxation of protons is varied for different biological tissues, which makes it possible to distinguish them on the MRI image (contrasting). However, MRI sensitivity is relatively low. Thus in early diagnosis stage, the difference between normal and abnormal regions is usually subtle, and additional contrast is required to highlight the abnormal region.

To achieve this, the following tasks we solved: preparation series of samples of contrast agents (including synthesis of rare-earth trifluorides nanosized TbF<sub>3</sub>, DyF<sub>3</sub>), characterization of samples, preparation of aqueous colloidal solutions); the measurements of relaxivities R<sub>1</sub>, R<sub>2</sub> and its dependencies on magnetic field (Fig.1), concentration of solutions and size of dispersed particles; toxicity estimation towards to biological objects; establishment of optimal parameters proposed contrast agents for practical use.

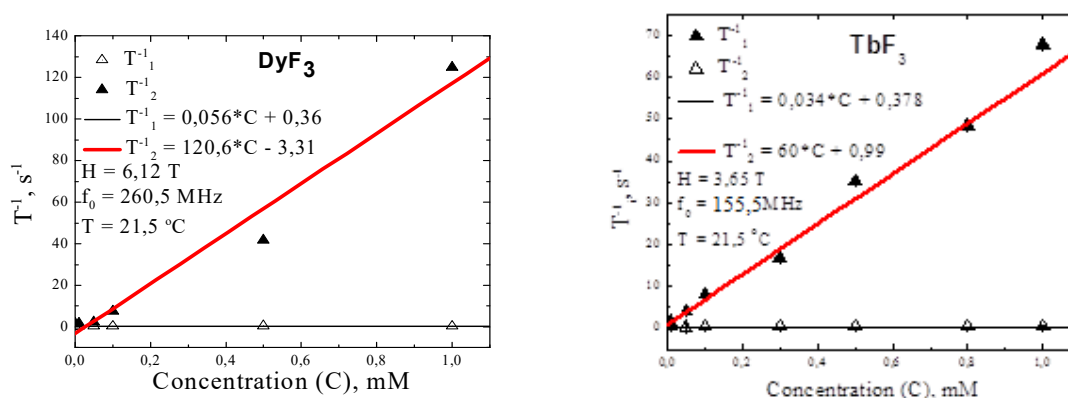


**Figure 1.** Concentration dependences of <sup>1</sup>H relaxation rates in TbF<sub>3</sub>, DyF<sub>3</sub> nanosized solutions.

This work was supported by the Russian Science Foundation (project no. 17-72-10198).

**Application of  $^{71}\text{Ga}$  and  $^{127}\text{I}$  NMR spectroscopy for the mechanistic studies of Ga(III)-mediated reactions of D–A cyclopropanes with pyrazolines**

R.A. Novikov, D.D. Borisov, Y.V. Tomilov

N. D. Zelinsky Institute of Organic Chemistry, Russian Academy of Sciences, 47 Leninsky prosp., 119991 Moscow, Russian Federation.

e-mail: novikovfff@bk.ru, lab6@ioc.ac.ru

Donor-acceptor (D–A) cyclopropanes are very convenient building blocks and are widely used in organic synthesis, especially in construction of naturally and biologically active compounds. Therefore, researches in this field are very perspective direction in modern organic chemistry. Recently, we have developed a new class of multi-component processes of D–A cyclopropanes based on their reactions with pyrazolines, in particular with spiro[cyclopropanepyrazolines] (fig.1). [1] These processes are catalyzed by Ga(III) or Al(III) compounds and have a number of specific features. One of the main features of the process is the participation of the halide anion from Ga-mediator, [2] which is quite unusual for these types of reactions. Considering the high synthetic potential of the processes, special investigations are required to study in details the mechanism, gallium transition complexes, and transfer of the halide anions.

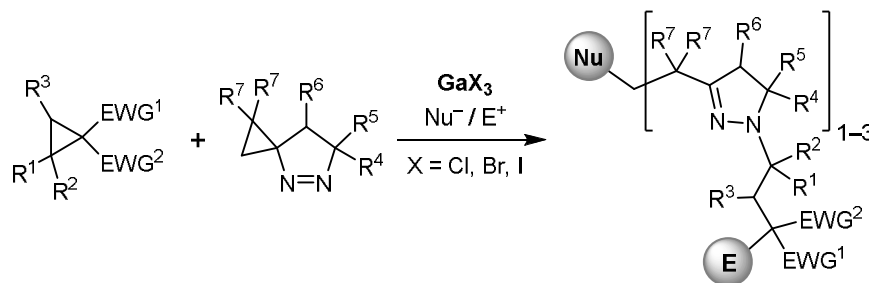


**Figure 1.** Reactions of D–A cyclopropanes with spiro[cyclopropanepyrazolines] mediated by Ga(III) salts.

To study the mechanism, we have synthesized the model complexes of  $\text{GaCl}_3$ ,  $\text{GaBr}_3$  and  $\text{GaI}_3$  with sterically hindered D–A cyclopropane with two Me-groups in both *ortho*-positions to stabilize of intermediate gallium complexes (fig.2). The assignment of their structures is a special very complicated challenge, because the X-Ray is completely inapplicable due to the instability of complexes or their liquid aggregate state. To solve their structures, we have developed a special approach based on the application of  $^{71}\text{Ga}$  NMR spectroscopy, which was specially optimized for these objectives both in terms of acquisition and decoding, [3] because the  $^{71}\text{Ga}$  nucleus has a large quadrupole moment and cannot be used in a conventional manner.

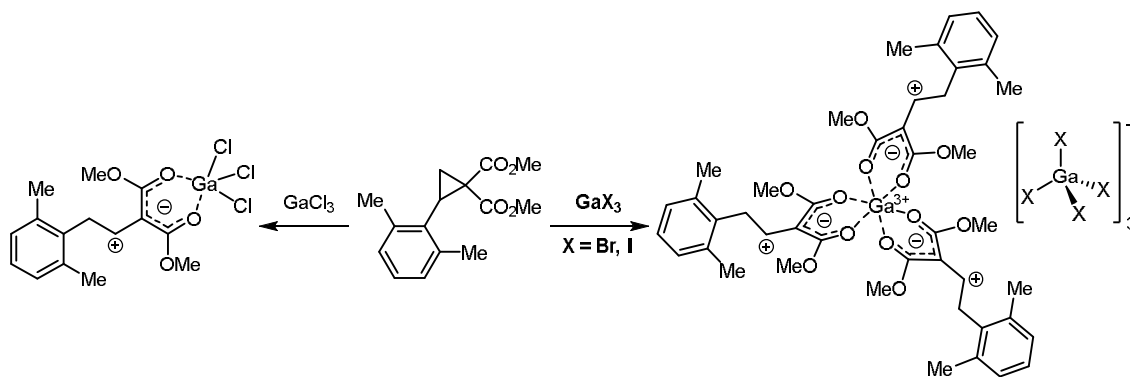


**Figure 2.** Formation of different types of Ga-complexes using model di-Me D–A cyclopropane.

We have found that the type of complexes formed dramatically depends on the halide anion in gallium(III) salt (fig.2). Of particular interest are the complexes with  $\text{GaBr}_3$  and  $\text{GaI}_3$ , which have ionic structures with a strict 3/4 composition (fig.2), and this type of structures was not observed before for D–A cyclopropanes. The key feature is the presence in structure of the  $\text{GaHal}_4^-$  anions, which transport the halide anions in the course of the reactions.  $^{71}\text{Ga}$  NMR spectra have two different signals showing two different types of Ga-atoms, which are quite easily separated by deconvolution (fig.3).  $\text{GaHal}_4^-$  anions have a high symmetry and give narrow intense signals in  $^{71}\text{Ga}$  spectra. Also,  $\text{GaI}_4^-$  anions were detected in  $^{127}\text{I}$  NMR spectra (fig.3).

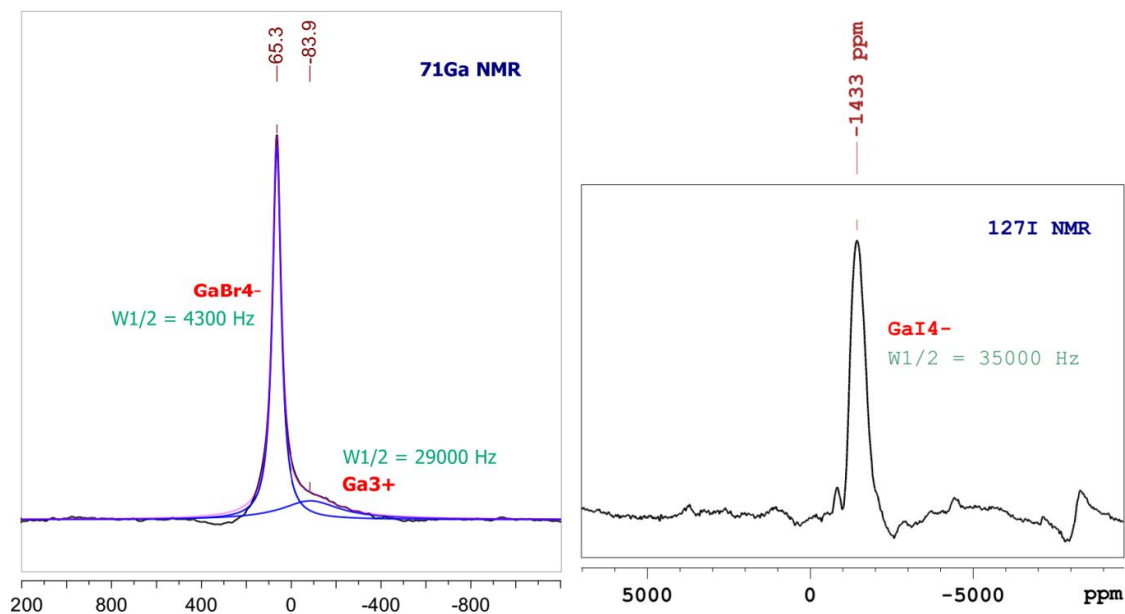


**Figure 3.** Key characteristic  $^{71}\text{Ga}$  (after deconvolution) and  $^{127}\text{I}$  NMR spectra for ionic Ga-complexes indicated on Fig.2.

Complexes with  $\text{GaCl}_3$  have a different type of structure and are covalent (fig.2). Their structures in solutions were studied by 1D and 2D multinuclear NMR spectroscopy. These gallium complexes exist in  $\text{CD}_2\text{Cl}_2$  solution predominantly in a dimeric form due to the formation of two Ga–Cl–Ga bridges (fig.4). Formation of the dimeric structures was investigated using 2D Diffusion Ordered NMR Spectroscopy (DOSY), which allows to estimate a molecular weight of compounds in solution without its isolation (fig.4).

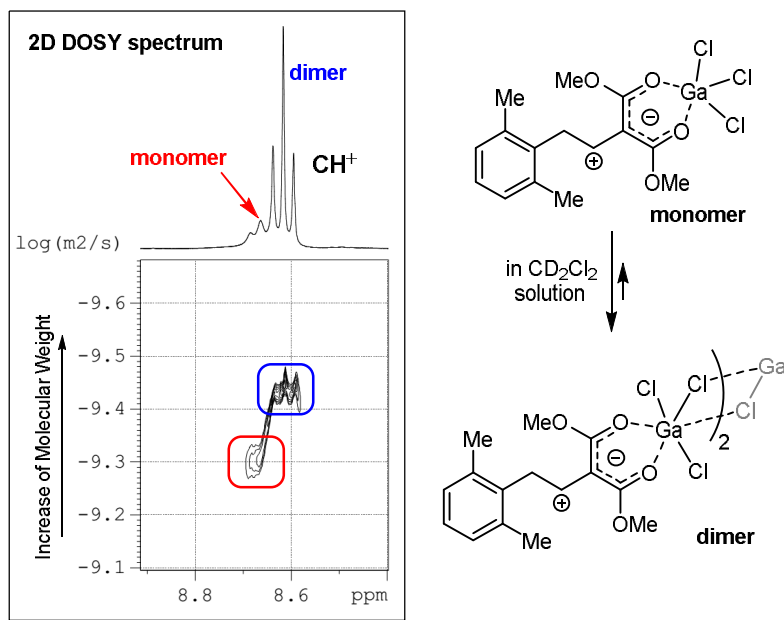


**Figure 4.** <sup>1</sup>H DOSY NMR spectra demonstrating the equilibrium monomer–dimer.

Summary, we have developed a new complex approach to the study of the mechanisms of gallium-catalyzed processes on the example of reactions of D–A cyclopropanes with pyrazolines, based on the analysis of data of <sup>71</sup>Ga NMR spectroscopy, which was specially adapted and optimized for such objectives. It is an important step on the way to the next generation of gallium chemistry.

The work was supported by the Russian President’s Council for Grants (grant MK-3465.2017.3)

#### References

- [1] R.A. Novikov, D.D. Borisov, M.A. Zotova, D.A. Denisov, Y.V. Tkachev, V.A. Korolev, E.V. Shulishov, Y.V. Tomilov. *J. Org. Chem.* **2018**, *83*, 7836–7851.
- [2] R.A. Novikov, D.D. Borisov, A.V. Tarasova, Y.V. Tkachev, Y.V. Tomilov. *Angew. Chem. Int. Ed.* **2018**, *57*, 10293–10298.
- [3] R.A. Novikov, K.V. Potapov, D.N. Chistikov, A.V. Tarasova, M.S. Grigoriev, V.P. Timofeev, Y.V. Tomilov. *Organometallics* **2015**, *34*, 4238–4250.

## Experimental investigation of magnetostriction in LiRF<sub>4</sub> (R=Yb, Tm) in the strong magnetic fields.

D.S. Nuzhina<sup>1</sup>, S. Abe<sup>2</sup>, S.L. Korableva<sup>1</sup>, K. Matsumoto<sup>2</sup>, I.V. Romanova<sup>1</sup>, K. Ubukata<sup>2</sup>,  
M.S. Tagirov<sup>1</sup>

<sup>1</sup> Institute of physics, Kazan Federal University, Kazan, 42008, Russia,

<sup>2</sup> Physics department, Kanazawa University, Kanazawa, 920-11, Japan

e-mail: nuzh.darya@gmail.com

The magnetoelastic properties of rare-earth double fluorides LiRF<sub>4</sub> (R is a rare-earth ion) have been systematically studied experimentally and theoretically since the 1970s [1-6]. The study of magnetic properties of LiRF<sub>4</sub> single crystals is an important problem for the development of the theory of magnetoelastic effects in magnetically concentrated crystals containing rare-earth ions. The effect of magnetostriction has been used to generate ultrasonic vibrations. Materials with a large magnitude of magnetostriction are used to fabricate magnetostrictive transducers [7]. One of the promising materials may be double fluorides of rare earths. LiYF<sub>4</sub> crystals having the same structure as LiRF<sub>4</sub> activated by Ho<sup>3+</sup>, Yb<sup>3+</sup>, Tm<sup>3+</sup>, and Dy<sup>3+</sup> ions are good laser materials [8] and used to convert the frequency of radiation in the infrared and visible spectral regions [9]. The significant influence of magnetic fields on the structure of the crystal lattice of double fluorides of rare earths was observed [10-12]. This effect appears only in strong magnetic fields. The LiTmF<sub>4</sub> is a dielectric van Vleck paramagnet [13], a distinguishing feature of which is a strong magnetoelastic interaction, as evidenced by the giant magnetostriction discovered in ref. [14], and the characteristic extremum of the temperature dependences of elastic constants [1,15]. However, accurate and correct data [16] of the magnetostriction as a function of the magnetic field and temperature, especially in strong magnetic fields (up to 8 T) and at low temperatures, was not observed. Thus, the study of the dependence of the magnetostriction of double fluorides on the magnetic field is an actual problem. The single crystal LiYbF<sub>4</sub> is an antiferromagnet, the temperature of the transition to the magnetically ordered state is T<sub>N</sub> = 130 mK [17]. The magnetostriction of LiYbF<sub>4</sub> single crystal has not been measured as of now.

Magnetostriction measurement of LiYbF<sub>4</sub>, LiTmF<sub>4</sub> single crystals have been carried out on a capacitive dilatometer [18] in static magnetic fields in the range 0-8 T at temperatures of 2, 5, and 10 K.

Rare earth ion Hamiltonian possessing nuclear spin **I** defined in electron-nuclear state space (2J+1)(2I+1) of the main multiplet with total angular electronic angular momentum **J**, can be written as:

$$\mathcal{H} = \mathcal{H}_0 + \mathcal{H}_z + \mathcal{H}_d, \quad (1)$$

where  $\mathcal{H}_0$  is the ion energy in the crystal field, determined by seven independent parameters of the crystal field  $B_q^k$ ,  $\mathcal{H}_z$  is the Zeeman energy,  $\mathcal{H}_d$  is the change in the ion energy in the crystal field under deformation of the lattice, which is determined by the deformation tensor [19].

The magnetostriction of LiYbF<sub>4</sub> single crystal was calculated in the framework of the exchange-charge model taking into account dipole-dipole and electron-deformation interactions (Fig.1). Table 1 and Table 2 show the measured and calculated by diagonalizing

the Hamiltonian (2) energy levels of the lower sublevels of the main multiplet for LiTmF<sub>4</sub> and LiYbF<sub>4</sub> relatively.

$$\mathcal{H}_0 = B_2^0 O_2^0 + B_4^0 O_4^0 + B_4^{-4} O_4^{-4} + B_6^0 O_6^0 + B_6^4 O_6^4 + E_6^{-4} \Omega_6^4, \quad (2)$$

where  $B_p^k$  – independent parameters of the crystal field,  $O_p^k$  – combination of spherical tensor operators, which match with the corresponding Stevens operators [20].

**Table 1.** Energy (cm<sup>-1</sup>) of the Stark sublevels of the main multiplet of the rare-earth Tm<sup>3+</sup> ion in LiTmF<sub>4</sub>.

	Experiment [21]	Calculation
Γ <sub>2</sub>	0	0
Γ <sub>3,4</sub>	31	31
Γ <sub>1</sub>	56	62
Γ <sub>2</sub>	282	281
Γ <sub>2</sub>	319	313
Γ <sub>1</sub>	363	361
Γ <sub>3,4</sub>	-	377
Γ <sub>3,4</sub>	-	402

**Table 2.** Energy (cm<sup>-1</sup>) of the Stark sublevels of the main multiplet of the rare-earth Yb<sup>3+</sup> ion in LiYbF<sub>4</sub>.

	Experiment [17]	Calculation
Γ <sub>5,6</sub>	0	0
Γ <sub>7,8</sub>	235.03	235.4
Γ <sub>7,8</sub>	371.9	366.08
Γ <sub>5,6</sub>	442.64	453.8

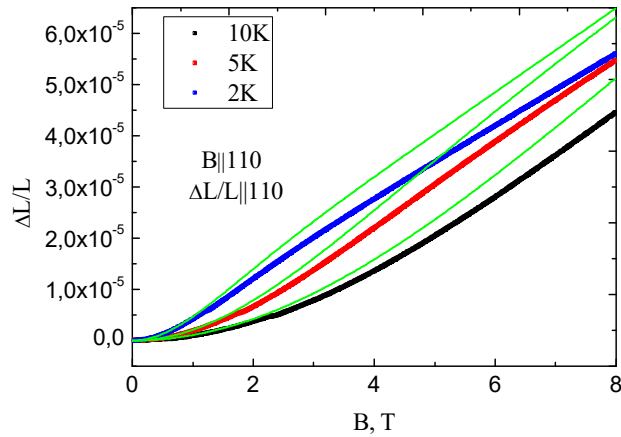


**Figure 1.** Magnetostriction as a function of the magnetic field in LiYbF<sub>4</sub> single crystal  $B \parallel (110)$ , T=2,5,10 K: measured data – points, calculates data – green line.

The work was supported by Russian Foundation for Basic Research (grant № 18-42-160012 p\_a).

**References**

- [1] S.A. Al'tshuler et al. Sov. Sci. Rev.: Sect. A. 6 (1985).
- [2] L.K. Aminov et al. Handbook on the Physics and Chemistry of Rare Earths. 22, (1996).
- [3] A.V. Klochkov et al. Journal of Experimental and Theoretical Physics Letters. 66(4), 266-270 (1997).
- [4] P.E. Hansen & R. Nevald. Physical Review B. 16(1), 146 (1977).
- [5] V. Vasyliiev et al. Optics express. 20(13), 14460-14470 (2012).
- [6] K. Kjaer et al. Journal of Physics: Condensed Matter. 1(33), 5743 (1989).
- [7] I.G. Horbenko, Sound, ultrasound, infrasound. Knowledge, 1986.
- [8] E. Chicklis et al. IEEE Journal of Quantum Electronics, 8. 225-230 (1972).
- [9] R.K. Watts & W.C. Holton. Solid State Communications, 9. 137-139 (1971).
- [10] T.F. Rosenbaum et al. Journal of applied physics, 70(10), 5946-5951 (1991).
- [11] S.A. Al'tshuler et al. JETP Lett. 32(3) (1980).
- [12] L.A. Bumagina et al. Zh. Eksp. Teor. Fiz. 80, 1543-1553 (1981).
- [13] H.P. Christensen, Phys. Rev. B. 19(12), 6573 (1979).
- [14] R.Yu. Abdulsabirov et al., FTT, 35, 1876-1880 (1993).
- [15] F.L. Aukhadeev et al., Fiz. Tverd. Tela 23, 2285 (1981).
- [16] J.L. Dunn et al. Physical Review B. 86(9), 094428 (2012).
- [17] P. Babkevich et al. Physical Review B. 92(14), 144422 (2015).
- [18] S. Abe et al., Cryogenics. 52(10), 452-456 (2012).
- [19] I.V. Romanova et al. Optics and spectroscopy. 116(6), 92-100 (2014).
- [20] S.A. Altshuler, B.M. Kozyrev. M.:Nauka, 1972.
- [21] A.K. Kupchikov et al. FTT. 24, 2373-2380 (1982).

## EPR of calixarenes doped by rare-earth metals ions

E.A. Razina,<sup>a</sup> A.S. Ovsyannikov,<sup>a, b</sup> S. E. Solovieva,<sup>a, b</sup> I. S. Antipin,<sup>a, b</sup> A. I. Konovalov,<sup>a</sup>  
G.V. Mamin,<sup>a</sup> M.R. Gafurov,<sup>a</sup> M.S. Tagirov,<sup>a</sup> S.B. Orlinskii<sup>a</sup>

<sup>a</sup> Kazan Federal University, 420008, Kremlevskaya str.18, Kazan, Russian Federation.

<sup>b</sup> A.E. Arbuzov Institut of Organic and Physical Chemistry of Kazan Scientific Center of Russian Academy of Science, 420088, Arbuzov str. 8, Kazan, Russian Federation.

e-mail: helenrazi@yandex.ru

The development of current computation technologies is closely related to creation of new type materials based on the application of quantum states such as metal-organic grids. Calixarenes doped by rare-earth metal ions are a promising molecular platform for the realization of metal-organic grids, and accordingly have great potential for use as functional materials [1].

The investigated substances were BuS<sub>4</sub>CH<sub>2</sub>COOH calixarenes doped by rare-earth metals ions Lu<sup>3+</sup>, La<sup>3+</sup>, Gd<sup>3+</sup>, Yb<sup>3+</sup>, Er<sup>3+</sup> and S<sub>8</sub>CH<sub>2</sub>COOH doped by Tb<sup>3+</sup>, Dy<sup>3+</sup>. Samples were synthesized by the Antipin I. S. in Laboratory of Organic Chemistry at the Institute of Chemistry of KFU [2]. For the EPR studies calixarenes doped by rare-earth ions Lu<sup>3+</sup>, La<sup>3+</sup>, Tb<sup>3+</sup>, Gd<sup>3+</sup>, Yb<sup>3+</sup>, Er<sup>3+</sup> and Dy<sup>3+</sup> were grown in the form of crystals. Important, calixarenes were doped by rare-earth ions during the synthesis of the molecules in order to allow metal ions to take place in the inner cavity of the calixarenes' molecule. Then the microcrystals were grown by evaporating from saturated solution. The average size of the microcrystals of calixarenes was about 100x100x4 μm (fig. 1).

The EPR spectra were measured by W-band Bruker spectrometer, at a temperature of 15-300K.

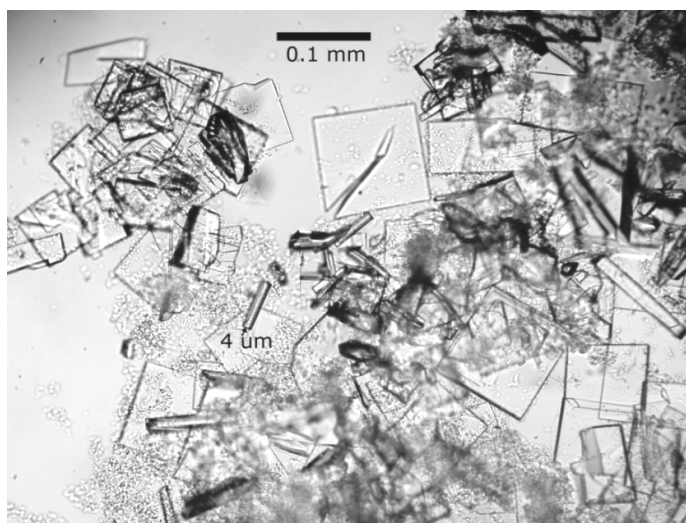


**Figure 1.** BuS<sub>4</sub>CH<sub>2</sub>COOH calixarenes crystals doped by rare-earth metals ions Lu<sup>3+</sup>

The EPR spectra of BuS<sub>4</sub>CH<sub>2</sub>COOH calixarenes doped by Lu<sup>3+</sup>, La<sup>3+</sup> ions and S<sub>8</sub>CH<sub>2</sub>COOH doped by Tb<sup>3+</sup> are shown in figure 2. One can see the EPR lines weren't observed in the measured spectra, due to Lu<sup>3+</sup>, La<sup>3+</sup> and Tb<sup>3+</sup> being nonparamagnetic ions. Thus unwanted paramagnetic dopants weren't detected in the samples.

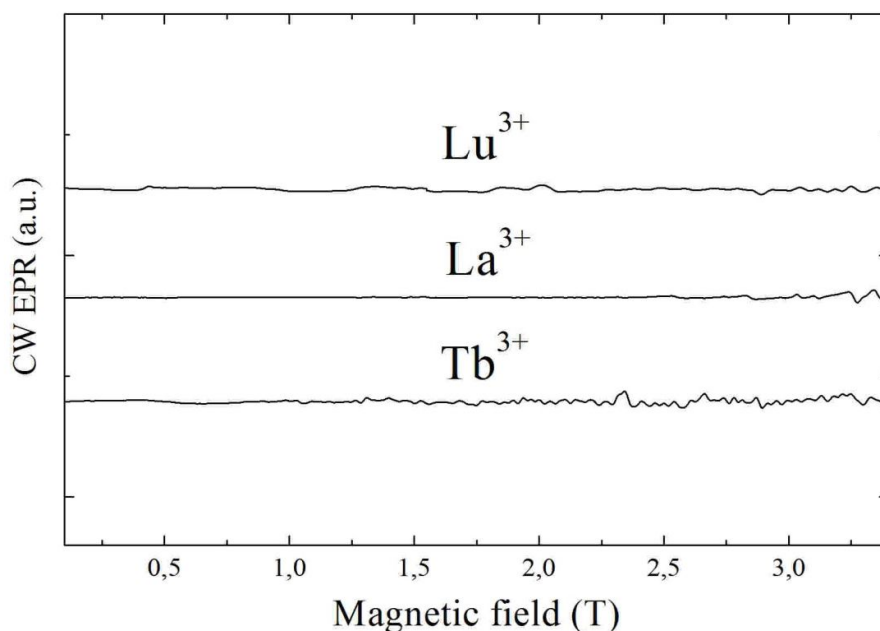


**Figure 2** .Continues wave EPR spectra of  $\text{BuS}_4\text{CH}_2\text{COOH}$  doped by  $\text{Lu}^{3+}$ ,  $\text{La}^{3+}$  ions and spectra of  $\text{S}_8\text{CH}_2\text{COOH}$  doped by  $\text{Tb}^{3+}$  ions

The EPR spectra of  $\text{BuS}_4\text{CH}_2\text{COOH}$  doped by  $\text{Gd}^{3+}$ ,  $\text{Yb}^{3+}$ ,  $\text{Er}^{3+}$  ions and spectra of  $\text{S}_8\text{CH}_2\text{COOH}$  doped by  $\text{Dy}^{3+}$  ions are shown in figure 3. The shape of the lines was complicated to calculate spectroscopic parameters directly so, to deal with it, the approximation was hold. The approximation results are shown in figure 3 by dotted line and its parameters are presented in table 1.

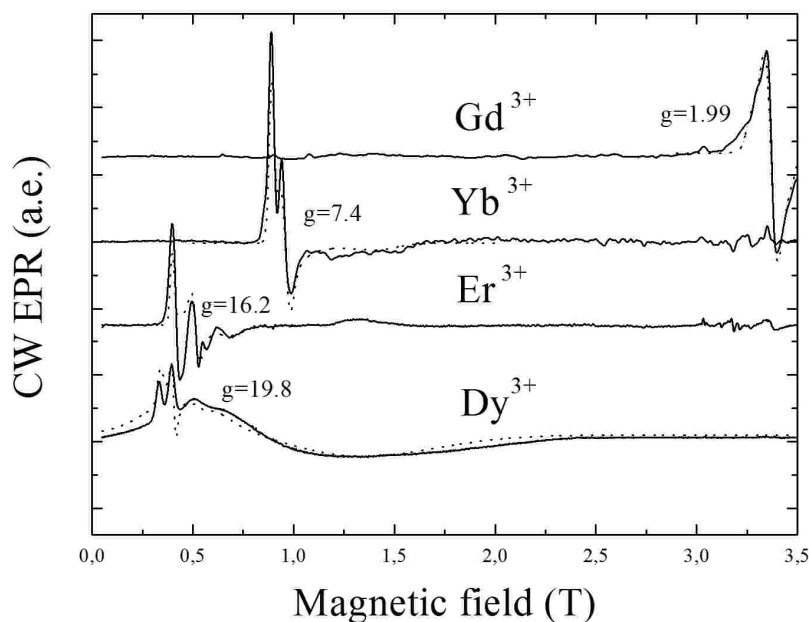


**Figure 3** .Continues wave EPR spectra of  $\text{BuS}_4\text{CH}_2\text{COOH}$  doped by  $\text{Gd}^{3+}$ ,  $\text{Yb}^{3+}$ ,  $\text{Er}^{3+}$  ions and spectra of  $\text{S}_8\text{CH}_2\text{COOH}$  doped by  $\text{Dy}^{3+}$  ions

The calculated g-factors of rare-earth metal ions in calixarenes were compared with the g-factors of free  $Gd^{3+}$ ,  $Yb^{3+}$ ,  $Er^{3+}$ ,  $Dy^{3+}$  ions and g-factors of  $Gd^{3+}$ ,  $Yb^{3+}$ ,  $Er^{3+}$ ,  $Dy^{3+}$  ions in  $CaWO_4$  [3]. The comparison showed the proximity of the calculated g-factor values to the values obtained for the ions in  $CaWO_4$  and the strong discrepancy with the g-factor of free ions values.

**Table 1** - Comparison of g-factors

	S	$g_{zz}$	$g_{yy}$	$g_{xx}$	D (MHz)	g-factors of free ions	g-factors in $CaWO_4$ [3]
S8-Tb	3/2	-	-	-	-	1.5	17.7-17.8
S4-Gd	7/2	2.01(1)	1.98(1)	1.98(1)	880(9)	2	1.9915-1.9916
S4-Yb	1/2	4.70(5)	6.95(5)	7.50(5)	--	1.1	1.05-3.90
S4-Er	1/2	9.5(1)	13.0(1)	16.8(1)	--	1.2	1.25-8.38
S8-Dy	1/2	19.8(5)	16.5(5)	12.0(5)	--	1.3	5.5-7.5
		13.0(5)	5.7(5)	5.7(5)	--		

A standard test of a dopant localization inside the microcrystal is the registration of magnetic field orientation dependencies of the microcrystal.

At first, the orientation dependence of the thiacalix[4]arenes microcrystal doped by  $Gd^{3+}$  ions was measured (fig.4). The sensitivity of the spectrometer was enough to register the spectrum of one microcrystal. However, changes in the EPR spectra were poorly expressed because of the wide width of the lines (.03 – .1 T.). To reduce the spin interaction, and by extension the line width, the calixarenes containing paramagnetic and nonparamagnetic rare-earth ions must have a 1:100 ratio or less.

The sensitivity of the spectrometer did not allowed to register the spectrum of EPR thiacalix[4]arenes doped by Gd/Lu ions in a 1:99 ratio.

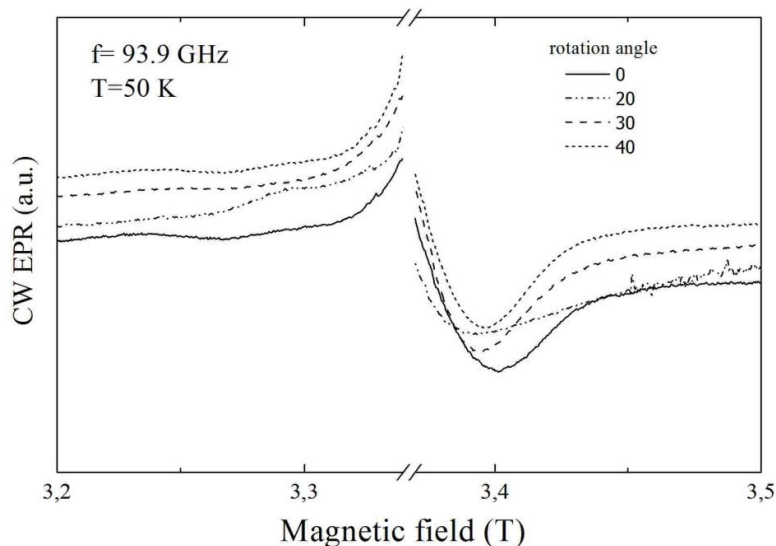


**Figure 4.** Magnetic field orientation dependencies of one particle (microcrystal)  $BuS_4CH_2COOH$  calixarene with  $Gd^{3+}$  (100%)

However, the sensitivity of the spectrometer was sufficient to record the EPR spectra of one thiocalix[4]arenes microcrystal doped by Er/Lu ions in a 1:99 ratio. The spectrums shown in the figure 5 demonstrate the magnetic field orientation dependencies of the microcrystal and point out the localization of dopants inside the microcrystal.

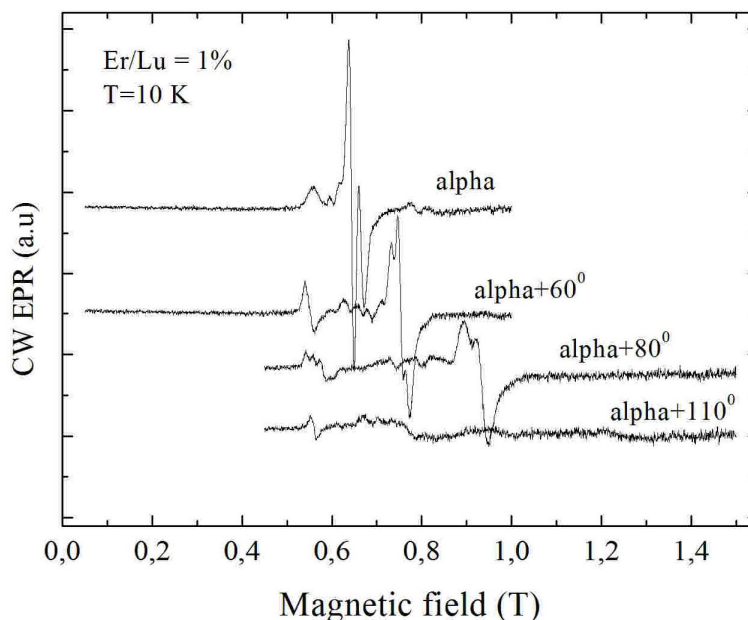


**Figure 5.** Magnetic field orientation dependencies of one particle (microcrystal)  $\text{Bu}_4\text{S}_4\text{CH}_2\text{COOH}$  calixarene with  $\text{Er}^{3+}$  (1%)

### References

- [1] Furukawa H. / H.Furukawa, U.Müller, O.M. Yaghi // *Angewandte Chemie International Edition*. -2015. V. 54. -Iss. 11. -P.3417-343.
- [2] Antipin, I. Thiocalix[4]arene derivatives bearing polymerizable 1,3-butadiyne fragments: Synthesis and incorporation into polydiacetylene vesicles / I. Antipin, V. Burilov, A. Valiyakhmetova, D. Mironova // *RSC Advances*. -2016.–Vol.6. -Is50. -P.44873-44877.
- [3] Kurkin, I.N. EPR of trivalent ions of a group of rare earths in a homologous series of crystals having the structure of  $\text{CaWO}_4$  / I.N. Kurkin // *Collected Paramagnetic Resonance*. 1969.-B.5. -C.31-73.

**Antiferromagnetic resonance in quasy-2D antiferromagnet  
Ba<sub>2</sub>MnGe<sub>2</sub>O<sub>7</sub>**

I.Rodygina<sup>1,2</sup>, V.N.Glazkov<sup>2,1</sup>, T.Masuda<sup>3</sup>

<sup>1</sup> National Research University “Higher School of Economics”, Faculty of Physics, Moscow, Russia

<sup>2</sup> P.Kapitza Institute for Physical Problems RAS, 119334 Moscow, Russia

<sup>3</sup> International Graduate School of Arts and Sciences, Yokohama City University, Yokohama, Kanagawa 236-0027, Japan

e-mail: rodygina\_irina@mail.ru

The quasy-2D antiferromagnet Ba<sub>2</sub>MnGe<sub>2</sub>O<sub>7</sub> was recently studied by neutron scattering and thermodynamic methods [1]. Crystallographic structure features planes of magnetic (S=5/2) manganese ions, which are separated from each other by planes of nonmagnetic barium ions. Therefore, as far as magnetic properties are of interest, sample is considered to be quasi-two-dimensional. Based on the analysis of the inelastic neutron scattering data [1], the exchange integrals inside the plane J<sub>1</sub> and between the planes J<sub>2</sub> were determined. They differ approximately by a factor of 30: J<sub>1</sub>=27.8 μeV and J<sub>2</sub>=1μeV. Ba<sub>2</sub>MnGe<sub>2</sub>O<sub>7</sub> orders antiferromagnetically at 4.2K, antiferromagnetic phase was identified as a collinear antiferromagnet with easy-plane anisotropy [1].

Electron spin resonance spectroscopy is a powerful tool to study antiferromagnetically ordered phases. Its routine energy resolution of 1 GHz (5 μeV) allows to identify magnon gaps and to find anisotropy parameters with high accuracy. We have performed series of measurements at different microwave frequencies from 9 to 30 GHz at the external magnetic field applied along the main anisotropy axis and orthogonal to it. The sample was mounted on the bottom of the microwave resonator and immersed in a helium-4 or helium-3 cryostat equipped with a cryomagnet. The microwave radiation from the generator along enters the resonator with the sample via one waveguide, leaves the resonator via second waveguide and

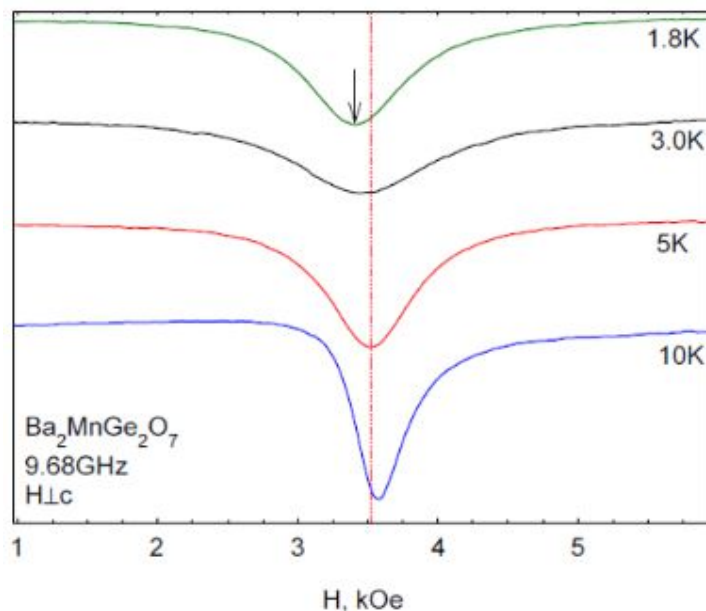


**Figure 1.** An example of ESR absorption data recorded at a frequency of 9.5 GHz for a field applied perpendicular to the anisotropy axis at

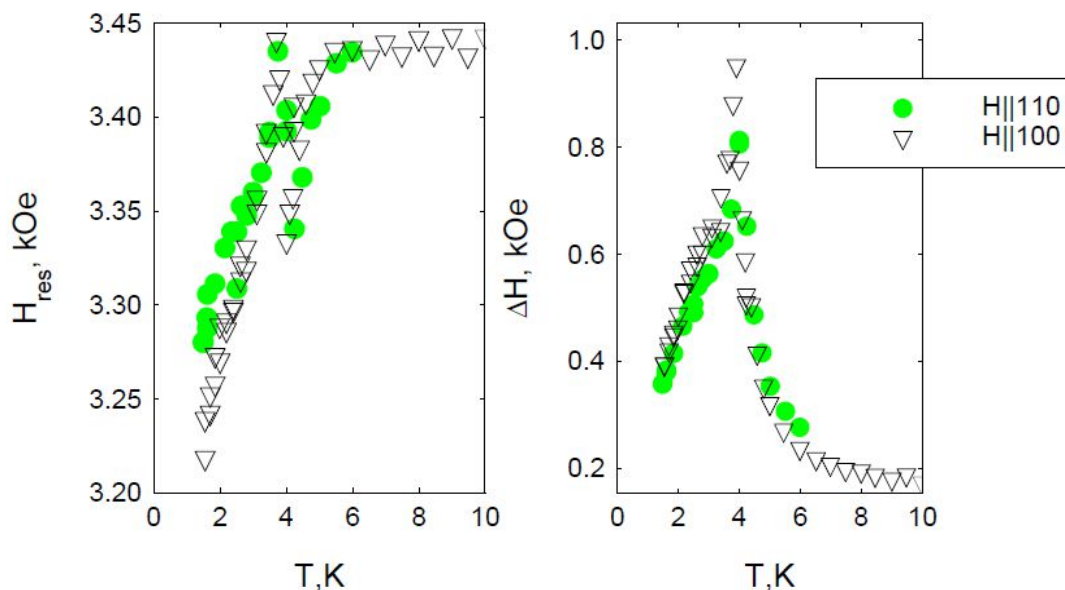


**Figure 2.** Temperature dependence of resonance field and linewidth for the field applied perpendicular the main anisotropy axis at 9.67GHz. Triangles: hits the detector. If absorption occurs in the sample, the power that falls on the detector falls off. This power is recorded as a function of the magnetic field produced by the solenoid, which yields a line of magnetic resonance at a certain frequency.

Crystallographic structure of  $Ba_2MnGe_2O_7$  is tetragonal, fourth order symmetry axis (c-axis) is the main anisotropy axis of the antiferromagnetic phase. We will denote this axis as Z in further calculations and we denote second order axes orthogonal to Z as X and Y.

For the magnetic field applied along the anisotropy axis  $H \parallel [001]$  observed evolution of ESR absorption is in agreement with the model of collinear easy-plane antiferromagnet.

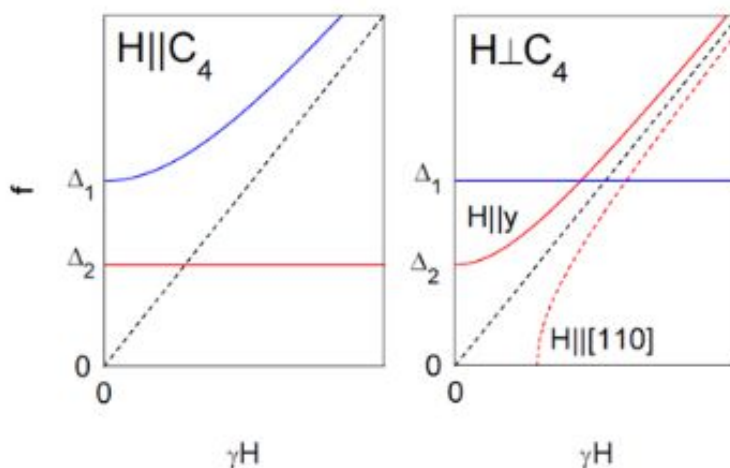


**Figure 3.** Modeled frequency-field diagrams for the tetragonal easy-plane antiferromagnet with in-plane anisotropy. Amplitude of in-plane anisotropy is strongly exaggerated for better presentation. Left panel: field parallel to the main anisotropy axis, right panel: field applied along  $[010]$  and  $[110]$

We have determined frequency-field dependence of antiferromagnetic resonance and derived the gap value, which is approximately 24 GHz (0.1 meV).

The Figure 1 shows an example of recorded magnetic resonance lines in a sample at a frequency of 9.5 GHz at different temperatures for a field applied perpendicular to the anisotropy axis. An absorption line is visible, which slightly shifts at the temperature below 4.2 K. This line can be fitted with a Lorentz resonance line. The results of fitting are shown in the Figure 2. The transition temperature is marked by the sharp change of the resonance field and by the maximum of the linewidth. Such a displacement at a field applied perpendicular to the axis of anisotropy is atypical for an antiferromagnet of the "easy plane" type: it is known that the magnetic resonance line for a field applied perpendicular to the axis of anisotropy should not be displaced if only axial anisotropy is present (which is expected for tetragonal case). Observed shift of the resonance absorption can be interpreted as a small zero-field gap of approx. 3 GHz.

The origin of this small gap is unclear, the likely candidates are fourth order anisotropy in the plane perpendicular to the main anisotropy axis and hyperfine interaction with Mn nuclear subsystem.

We analyzed effect of fourth order anisotropy on the AFMR spectra using the theory, developed by Andreev and Marchenko [2]. It can be included to the anisotropy energy as  $U_A = bl_x^2 + \alpha l_x^2 l_y^2$ , here  $\vec{l}$  is an antiferromagnetic order parameter ( $|\vec{l}| = 1$ ),  $b > 0$  corresponds to main easy-plane anisotropy and  $\alpha > 0$  describes in-plane anisotropy, which favors  $\vec{l} \parallel X$  or  $\vec{l} \parallel Y$ . The modeled frequency-field diagrams are shown on the Figure 3. For the case when the field is directed along the main anisotropy axis, one of the frequencies is independent of the field and equals zero if there is no anisotropy in the plane. The second frequency grows with the applied field. For a field lying in a plane, two variants are considered for the field applied along [100] and [110]. We have found that accounting for the 4-order anisotropy does result in the opening of small gap  $\Delta_2$  in the magnon spectrum. However, modeling predicts that resonance frequencies should deviate from the position of paramagnetic resonance in different directions for  $H \parallel [100]$  and  $H \parallel [110]$  (right panel of Figure 3). This prediction contradicts to experimental observations (see Figure 2).

To check whether the hyperfine coupling is responsible for the observed effect we have performed AFMR measurements using helium-3 cryostat down to 450 mK. We have observed that resonance line continue to shift even below 1K, which is well below Neel temperature. This behavior is in qualitative agreement with the model of hyperfine coupling between electron and nuclear subsystems since magnetization of nuclear subsystem continues to increase on cooling.

Thus, we have studied antiferromagnetic resonance in quasy-2D antiferromagnet Ba<sub>2</sub>MnGe<sub>2</sub>O<sub>7</sub>. We have determined value of the gap in the magnon spectrum (approx. 24 GHz) and we have observed another smaller gap (approx. 3 GHz), which is supposedly due to hyperfine coupling between nuclear and electronic subsystems.

## References

- [1] T. Masuda et al, Physical Review B 81, 100402R (2010)
- [2] A.F. Andreev, V.I. Marchenko Sov. Phys. Uspekhi 130, 39 (1980)

**Spin-lattice relaxation of  $\text{NO}_3^{2-}$ -complex in synthetic hydroxyapatite.  
Calculation of the relaxation rate using the phonon spectrum**

D.V. Shurtakova<sup>1</sup>, G.V. Mamin<sup>1</sup>, M.R. Gafurov<sup>1</sup>, S.B. Orlinskii<sup>1</sup>, E.S. Klimanshina<sup>2</sup>, V.I. Putlyayev<sup>2</sup>

<sup>1</sup>Kazan Federal University, Institute of Physics, 420008, Kremlevskaya st., Kazan, Russian Federation

<sup>2</sup>Moscow State University, Moscow, 119992 Russia

e-mail: darja-shurtakva@mail.ru

Hydroxyapatite (HAP)  $\text{Ca}_{10}(\text{PO}_4)_6(\text{OH})_2$  used for medicine application: restoration of bone tissue, as implants, for orthopedic and so on. The development of synthesis method of hydroxyapatite with preset properties is an actual task.

Purpose of the work is description of temperature dependence of spin-lattice relaxation of  $\text{NO}_3^{2-}$ -complex in synthetic hydroxyapatite powders with particles size 30 and 1000 nm. These samples were synthesized on the Faculty of Science of New Materials at Moscow State University.

Temperature dependence of spin-lattice relaxation rate  $\text{NO}_3^{2-}$ -complex is shown in Figure 1. In the temperature range from 10 to 100 K the dependence is proportional to  $T^4$ . This value deviates from the usually dependencies  $T^9$  for Kramers ions [1, 2].

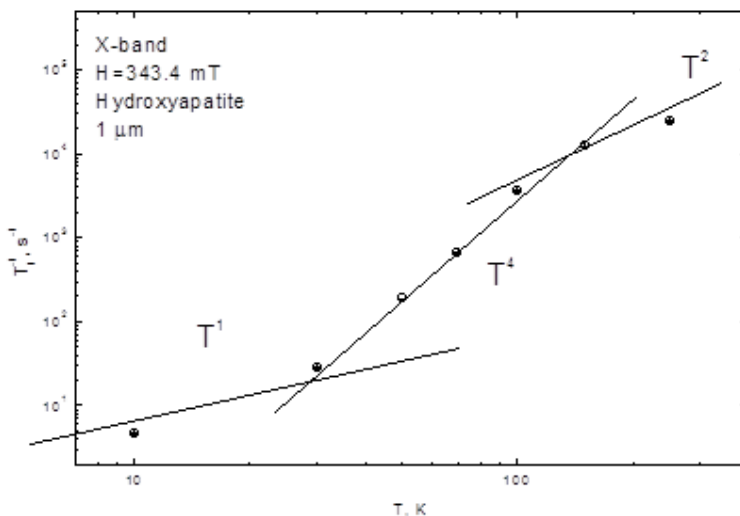


**Figure 1.** Temperature dependence of spin-lattice relaxation rate in magnetic field  $H=343.4\text{mT}$

According to Orbach's theory, the spin-lattice relaxation rate is the sum of the rates of direct single-phonon and two-phonon processes.

To describe the spin-lattice relaxation rate of a one-phonon direct process, we use the calculations from [1]:

$$\frac{1}{T_1} = K_1 T, \tag{1}$$

$$K_1 = \frac{3\delta_{ab}k}{\pi\hbar^4\rho_{cryst}v_s^3} \left| \langle a | \sum_{n,m} V_n^m | b \rangle \right|^2,$$

where  $\delta_{ab}$ - energy difference between levels  $|b\rangle$  and  $|a\rangle$ ,  $k$  – Boltzmann coefficient,  $T$  – lattice temperature,  $\rho_{cryst}$  – crystal density,  $v_s$  – sound's speed in a crystal,  $|\langle a | \sum_{n,m} V_n^m | b \rangle|$  – matrix element.

In the case when the spin  $S=1/2$  it is required to use the second order perturbation theory [3] for calculating the matrix element in (1), as for two-phonon relaxation process.

For two-phonon relaxation process use results from [3]:

$$\frac{1}{T_1} = \frac{4\pi\hbar^2}{\rho_{cryst}^2 v_s^4} \frac{\langle b | V^{(1)} | a \rangle^4}{\Delta_{cryst}^4} \int_0^{\omega_{max}} \bar{n}(\bar{n} + 1) \omega^4 \rho^2 d\omega, \quad (2)$$

$$\text{where } \bar{n}(\bar{n} + 1) = \frac{e^x}{(e^x - 1)^2}, \quad x = \frac{\hbar\omega}{kT}$$

$\Delta_{cryst}$  – energy up to an excited level,  $\langle b | V^{(1)} | a \rangle$  – matrix element (spin-phonon interaction parameter).

We introduce the coefficient  $K_2$ :

$$K_2 = \frac{4\pi\hbar^2}{\rho_{cryst}^2 v_s^4} \frac{\langle b | V^{(1)} | a \rangle^4}{\Delta_{cryst}^4}. \quad (3)$$

The rate of spin-lattice relaxation observed in experiments can be described by the sum of direct and two-phonon processes:

$$\frac{1}{T_1} = K_1 T + K_2 \int_0^{\omega_{max}} \frac{e^{\frac{\hbar\omega}{kT}}}{(e^{\frac{\hbar\omega}{kT}} - 1)^2} \omega^4 \rho^2 d\omega \quad (4)$$

Consider the case of describing the rate of the spin-lattice relaxation using the Debye model [2], wherein the density of phonon spectra has the form  $\rho(\omega) = 3\omega^2/(2\pi^2v^3)$ . Substitute  $\omega^2$  into (5) and make a change of variables we obtain a relaxation rate for the two-phonon process proportional to [3]:

$$\frac{1}{T_1} \propto \left(\frac{kT}{\hbar}\right)^9 \int_0^{T_D/T} \frac{e^x x^8}{(e^x - 1)^2} dx \quad (6)$$

The result of the description of the experimental temperature dependence of the spin-lattice relaxation rate using the Debye model is shown in Figure 2, the Debye temperature is determined. The spin-lattice relaxation rate curve describes well the experimental points, but

the Debye temperature determined from the approximation lower by about 60 degrees compared with the Debye temperature, defined in [4] by the heat capacity ( $T_D = 389\text{K}$ ).

We calculate the relaxation rate using the phonon spectrum obtained in [5] to check the cause of temperature differences.

The results of the calculation are shown in Figure 2. The calculated curve also describes well the experimental points, and the temperature of Debye ( $T_D = 378\text{K} \pm 30\text{K}$ ) corresponds to the Debye temperature ( $T_D = 389\text{K}$ ), obtained from the heat capacity [4].

An analogous approximation using the calculated phonon spectrum was made for a nanopowder. The curve also describes well the experimental points with the Debye temperature  $T_D=378\text{K}$ . Figure 3 shows a comparison of the descriptions of the spin-lattice relaxation rates using the phonon spectrum at the Debye temperature  $T_D = 378\text{ K}$ .

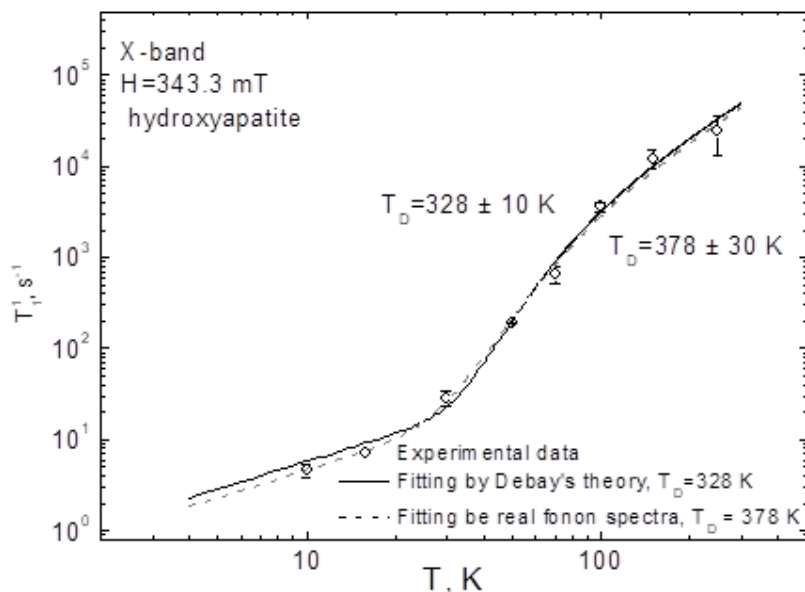


**Figure 2.** Temperature dependence of the spin-lattice relaxation rate of nitrogen complexes in hydroxyapatite, with an average particle size of 1  $\mu\text{m}$ . The solid line shows the approximation in the Orbach model ( $T_D = 328\text{ K}$ ), dash line - using the real phonon spectrum ( $T_D = 378\text{ K}$ )

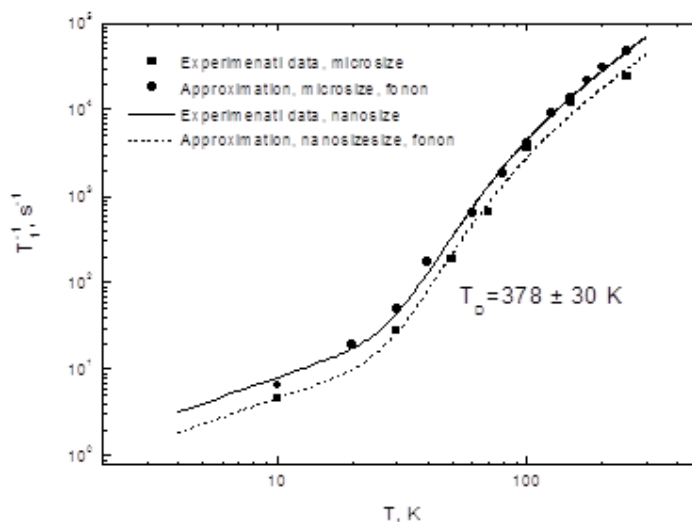


**Figure 3.** Approximation of the temperature dependence  $T_1^{-1}$  for microsize and nanosized powders with a calculated phonon spectrum and the Debye temperature  $T_D = 378$  K. The dash line is a microsize powder, the solid line is a nanosized powder.

It is obvious that the changes in the rate of spin-lattice relaxation in nanoparticles are mainly due to the coefficients  $K_1$  and  $K_2$  in (1) and (4). These coefficients are given in Table 1.

**Table 1.** The values of the approximation coefficients at the Debye temperature  $T_D = 378$  K.

Size	$K_1$ (a.u)	$K_2$ (a.u)
<i>micro</i>	0.4645	6.1282
<i>nano</i>	0.8052	9.6794
<i>nano/micro</i>	1.73	1.58
	$\sqrt[3]{1.73} = 1.12$	$\sqrt[3]{1.58} = 1.12$

It is seen that the coefficient before the integral  $K_2$  is 1.58 times and the coefficient for the direct process  $K_1$  is 1.73 times larger for the micro sample.

It can be assumed from (1) and (4) that the change in the coefficients for samples of different sizes is associated with a change in the speed of sound  $v_s$ , taking into account the  $\sqrt[3]{1.73} = 1.12$  and  $\sqrt[3]{1.58} = 1.12$ , we can conclude that the speed of sound in nanoparticles slows down by 12%.

### Conclusion

The spin-lattice relaxation rate curve, which has an inclination proportional to  $T^4$  in the range of average temperatures (below 100K) is well described using the Debye model, where  $\rho(\omega) = 3\omega^2/(2\pi^2v^3)$ . Since in the experiment obtained the temperature dependence of the spin-lattice relaxation rate deviates from the theoretical  $T^9$  for Kramers ions, and the resulting value of the Debye temperature deviates from the value  $T_D=389$ K, determined from the heat capacity in[4], then to describe this dependence it is necessary to take the integral directly, using the calculated phonon spectrum, close to reality.

The rate of spin-lattice relaxation in nanosamples increases in comparison with micro samples. Given the changes in the coefficients  $K_1$  before the temperature  $T$  and  $K_2$  before the integral for the direct and two-phonon processes, we supposed in the nanopowder, the speed of sound decreases by 12%.

### References:

- [1] Orbach, R. Spin-Lattice Relaxation in Rare-Earth Salts / R. Orbach // The proceedings of the Royal Society A. – 1961. – V. 264. – P. 458-484.
- [2] Аминов Л. К., Малкин Б. З. Динамика и кинетика электронных и спиновых возбуждений в парамагнитных кристаллах //Казань: Изд. Казанского университета. – 2008. – Т. 216.
- [3] Hoffmann, S. K. Raman electron spin–lattice relaxation with the Debye-type and with real phonon spectra in crystals / S. K. Hoffmann, S. Lijewski // Journal of Magnetic Resonance. – 2013. – V. 227. – P. 51-56.
- [4] Slepko, A., & Demkov, A. A. (2015). Hydroxyapatite: Vibrational spectra and monoclinic to hexagonal phase transition. Journal of Applied Physics, 117(7), 074701.
- [5] T. Biktagirov, M. Gafurov, K. Iskhakova, G. Mamin, S. Orlinskii (2016). [Phonon spectrum in hydroxyapatite: calculations and EPR study at low temperatures](#). Journal of Low Temperature Physics 185: 627-632.

## Self-diffusion of gaseous $^3\text{He}$ in oriented aerogels

V. Kuzmin<sup>1</sup>, K. Safiullin<sup>1</sup>, A. Stanislavovas<sup>1</sup>

<sup>1</sup>Kazan Federal University, 420008, Kremlevskaya 18, Kazan, Russian Federation.

Aerogels are subjects of many recent scientific studies. Due to their high porosity and low thermal conductivity they are widely used in space technology, for example as a thermal insulator and a Cherenkov radiation detectors [1]. Aerogels are materials with very low diamagnetic constant which allows to use them in microelectronic for reducing the stray wiring capacitance. It is known, that diamagnetic constant of aerogels depends on porosity [1].  $^3\text{He}$  is a one of the best probe for studies of the magnetic properties of nanosized porous samples at low temperatures due to sufficiently long relaxation times and the absence of a nuclear quadrupole moment. It is known that the aerogels has effect on certain properties of  $^3\text{He}$  nuclei at very low temperatures. Nowadays, interest in the study of the  $^3\text{He}$  superfluidity in aerogels has recently increased due to discovery of polar superfluid phases in fibers aerogels. [2, 3]. The ballistic mean-free path (*mfp*) in an aerogel  $\lambda_{\text{aero}}$  is an important parameter for theoretical models of  $^3\text{He}$  superfluidity and can be determined by diffusion experiments, for instance, *via* magnetic resonance experiments with gradients.

In this article, the results of  $^3\text{He}$  gas diffusion experiments in four types of ordered  $\text{Al}_2\text{O}_3$  aerogel with different density (82, 125, 180, 597 and 920  $\text{mg}/\text{cm}^3$ ) are represented. The samples with higher 597 and 920  $\text{mg}/\text{cm}^3$  densities were fabricated from 82 and 125  $\text{mg}/\text{cm}^3$  samples, respectively, by procedure described in [4]. It included the soaking of aerogel in the water for 20 minutes and drying at the room temperature during 48 hours.

A series of gas pressure dependencies *versus* amount of  $^3\text{He}$  in the samples with different types of surfaces (raw and modified by  $\text{N}_2$  or  $^4\text{He}$ ) are measured at 4.2 K. It is known that  $^3\text{He}$  atoms build a monolayer on substrate surface at a temperature of 4.2 K and changes negligibly at pressures higher than 50 mbar amount of adsorbed  $^3\text{He}$  not depends on gas pressure. The gas density obtained from experimental data is higher than density expected for ideal gas and magnification factor depends on *surface-to-volume* ratio of the samples.

The  $^3\text{He}$  gas diffusion study was carried out using gradient pulsed NMR methods at temperature of  $T = 4.2$  K with constant magnetic field gradient of  $G = 2.2$  mT/cm and at frequency of  $f_0 = 16$  MHz ( $H_0 = 490$  mT).

The samples were placed into the probe cell created from “Pyrex 7740” (82, 125, 180 and 597  $\text{mg}/\text{cm}^3$ ) and “Stycast 1266” (920  $\text{mg}/\text{cm}^3$ ) with horizontal orientation of fibers. The study was carried out with different directions of application of gradient  $G$  and constant external magnetic field  $B_0$  relatively to the samples fibers.

The values of diffusion coefficient were obtained from analysis of transverse magnetization decay curves, which were fit using a following function:

$$Y(2\tau) = Y_0 \exp\left(-\frac{2\tau}{T_2}\right) \exp\left(-\frac{\gamma^2 D G^2}{12} (2\tau)^3\right), \quad (1)$$

where  $Y(2\tau)$  is the spin-echo amplitude at moment  $t = 2\tau$ ,  $Y_0$  is the signal amplitude that corresponds to initial magnetization,  $T_2$  is the spin-spin relaxation time of  $^3\text{He}$  nuclei,  $D$  is the diffusion coefficient and  $\gamma = 2\pi \times 32.43$  MHzT<sup>-1</sup> is the gyromagnetic ratio of  $^3\text{He}$  atom.

The measured diffusion coefficient of  $^3\text{He}$  atoms in aerogels are significantly suppressed by the immobile adsorbed layer of  $^3\text{He}$  (the estimated diffusion coefficient in the

adsorbed layer lies between  $10^{-9}$  and  $10^{-8}$   $\text{cm}^2\text{s}^{-1}$  depending on the layer coverage [5, 6]. This is confirmed by two facts: 1) the diffusion coefficient anomalously drops at low pressures in opposition to that expected for free gas diffusion; 2) the covering of the aerogel surface with an approximate monolayer of  $^4\text{He}$  significantly increases the measured gaseous  $^3\text{He}$  diffusion coefficient at low pressures.

In addition, it was found that measured self-diffusion coefficient of  $^3\text{He}$  atoms is vary with different directions of applied constant external magnetic field relatively to the aerogels fibers. The value of this “anisotropy” of self-diffusion increases with the increase of samples density, i. e. depends on *surface-to-volume* ratio.

Following refs. [7] and [8] the apparent diffusion in aerogels is just weighted diffusion between that in the adsorbed layer and that in the gas phase. As diffusion in the gas phase is much faster than in the adsorbed layer the apparent diffusion in the aerogel is assumed to be governed by a “fast exchange” process [9]:

$$D = D_{\text{gas}}^{\text{aero}} \frac{N_{\text{gas}}}{N_0} + D_{\text{ads}} \frac{N_{\text{ads}}}{N_0}, \quad (2)$$

where  $D_{\text{gas}}^{\text{aero}}$  and  $D_{\text{ads}}$  are self-diffusion coefficients in gas phase and adsorbed layer of  $^3\text{He}$ , respectively, and  $N_{\text{gas}}$ ,  $N_{\text{ads}}$  and  $N_0$  are amounts of  $^3\text{He}$  in gas phase, adsorbed layer and total amount in the cell, respectively. The model of two-phases “fast-exchange” process is correct in case, when the lifetime of  $^3\text{He}$  atom in each phase is much shorter than measured time. This condition is always obeyed in present work, as the estimated typical lifetime of  $^3\text{He}$  atom in adsorbed layer is 1 ns and in gas phase is 10 ns. Both values are much shorter than typical measured time.

Note that self-diffusion in adsorbed layer, which plays an important role in some gases at high pressure, will be ignored further as being totally negligible. This is based on the fact that value of diffusion coefficient of  $^3\text{He}$  atom in filled adsorbed layer varies in range of  $10^{-9}$  -  $10^{-8}$   $\text{cm}^2\text{s}^{-1}$ . Thus, this is possible to estimate of self-diffusion coefficient of  $^3\text{He}$  atoms in gas phase using eq. 2.

It was found that values of diffusion coefficient of  $^3\text{He}$  atoms in gas phase are less than values expected for ideal gas at low pressure range, where the fraction of adsorbed atoms is large. In addition, the computed values of  $D_{\text{gas}}^{\text{aero}}$  not depend on type of sample surface (raw or covered by  $\text{N}_2$  or  $^4\text{He}$ ). Therefore, the observed effect of slow gas diffusion cannot be explained by the influence of surface diffusion.

On the other hand, the observed gas density is higher than expected for ideal gas at all pressure range. Reliability of the estimated gas density by NMR calibration is confirmed by the expected diffusion (for a given density) approaching the experimental diffusion at high pressures. This occurs when the fraction of adsorbed layer becomes negligible. Muller et. al. in [10] have observed such densification of  $\text{CO}_2$  by a factor of 2 in an aerogel and refer this effect to the gas liquation in micropores. In the case of  $^3\text{He}$  at low temperatures it is known that adsorption in micropores is completed at relatively low pressures of a few mbars [11]. Thus, the  $^3\text{He}$  densification can be explained by changing of property of the gas because of far-ranging adsorbtion potential of the fibers.

One of the possible reason of slow gas diffusion are also collisions between  $^3\text{He}$  atoms and aerogels fibers. This is known as the Knudsen diffusion which appears when the *mfp* in the gas phase, due to atom–atom collisions is longer or of the order of the geometrical

ballistic  $mfp$  in an aerogel ( $\lambda_{aero}$ ). In that case, diffusion coefficient in gas phase determined by free-gas  $D_{gas}^{free}$  and Knudsen  $D_{Kn}$  diffusion:

$$\frac{1}{D_{aero}} = \frac{1}{D_{gas}^{free}} + \frac{1}{D_{Kn}} \quad (3)$$

$$D_{Kn} = \frac{1}{3} \lambda_{aero} V_{gas}, \quad (4)$$

where  $\lambda_{aero}$  is  $mfp$  of  $^3\text{He}$  atom in aerogel and  $V_{gas}$  is the atom velocity.

However, Knudsen model cannot explain such strong reducing of apparent diffusion. In addition, after excluding the influence of adsorbed layer of  $^3\text{He}$  on gas diffusion the variation of diffusion coefficient with different directions of application of external magnetic field relatively to aerogels fibers also appears.

More details will be presented in oral report.

### References

- [1] Yu. K. Akimov, Instrum. Exp. Tech., 2003, 46, 287.
- [2] N. Zhelev. et. al., Nat. Commun., 2016, 7, 12975.
- [3] V. V. Dmitriev et. al., Phys. Rev. Lett., 2015, 115, 165304.
- [4] V. V. Volkov et. al., Instrum. Exp. Tech., 2017, 60, 737.
- [5] B. P. Cowan et. al., Phys. Rev. Lett., 1977, 38, 165.
- [6] B. Cowan et. al., Phys. B, 1990, 165, 707.
- [7] R. Valiullin et. al., J. Phys. Chem. B, 2005, 109, 5746.
- [8] J. A. Lee et. al., Phys. Rev. B: Condens. Matter Mater. Phys., 2014, 90, 174501.
- [9] E. Collin et. al., Phys. Rev. B: Condens. Matter Mater. Phys., 2009, 80, 094422.
- [10] R. Mueller et. al, Phys. Chem. Chem. Phys., 2015, 17, 27481.
- [11] N. Setoyama et. al., J. Phys. Chem., 1996, 100, 10331.

## The influence of the dipolar coupling strength on the spin dynamics of quasi-one-dimensional spin chains in fluorapatite

G.A.Bochkin<sup>1</sup>, E.B.Fel'dman<sup>1</sup>, I.D.Lazarev<sup>1,2</sup>, A.A. Samoilenko, S.G.Vasil'ev<sup>1</sup>

<sup>1</sup>Institute of Problems of Chemical Physics of Russian Academy of Sciences, Chernogolovka, Moscow Region, Russia 142432

<sup>2</sup>Faculty of Fundamental Physical-Chemical Engineering, Lomonosov Moscow State University, GSP-1, Moscow, Russia 119991

e-mail: viesssw@mail.ru

### Introduction

The opportunities of exploitation of the quantum mechanical systems for the information processing have been studied extensively over the recent years. Nuclear spins have long been considered as instructive illustration of qubits[1]. In particular spin-1/2 nuclei possesses the qubit's simple two-state structure and are well isolated from the environment. The latter feature is expected to ensure the long coherence lifetimes and hence allow for the large number of logic operation in a quantum device to be performed. Solid crystal devices hold promise for the scalable implementations. Some proposals using spin 1/2 nuclei as the qubits which are located in relatively isolated atomic chains are known from the literature [2, 3]. The interaction between spins is provided by the magnetic dipole-dipole coupling. The regularity of the lattice creates identical nuclear dipole coupling throughout the crystal and allows addressing of the nuclei within each chain by a large magnetic field gradient.

Large scale quantum information processing systems will require the preparation and control of multi-qubit states. Multiple quantum (MQ) NMR [4] is of special interest in the investigation of multi-qubit coherent states since it allow creation of these states and observation of the relaxation due to the action of a correlated spin reservoir [5-8].

The strength of the dipolar coupling is responsible for the number of spins in correlated cluster created in MQ experiment [5-8] and affects the rate of their relaxation [6-9]. The specific arrangement of spins in linear chain allow to "tune" the dipolar coupling between spins at will by the adjustment of the angle between the external magnetic field and the chain. Physical example of a one-dimensional chain of <sup>19</sup>F nuclear spins is a crystal of fluorapatite Ca<sub>5</sub>(PO<sub>4</sub>)<sub>3</sub>F (FAp). In the present study we investigate the influence of the strength of the dipolar coupling in quasi-one-dimensional spin chain of <sup>19</sup>F in a single crystal FAp on the NMR spectra and MQ NMR dynamics.

### Experimental

The experiments were performed on a Bruker Avance III spectrometer with the static magnetic field of 9.4 T (the corresponding frequency on <sup>19</sup>F nuclei is 376.6 MHz). A probe with a solenoid coil for 2.5 mm o.d. NMR sample tubes was used. The dimensions of the sample (FAp crystal) were approximately 3.8×1.5×1.5 mm. The orientation of c-axis was perpendicular to the larger faces of the sample. The orientation of the sample with respect to external magnetic field was achieved by the rotation of the sample tube around the solenoid axis at an angle  $\theta$ . The duration of  $\pi/2$  pulses was 0.8  $\mu$ s. The accuracy of rotation was estimated to be 2°. Chemical shift values are reported relative to CFCl<sub>3</sub>. Hexafluorobenzene (C<sub>6</sub>F<sub>6</sub>) at -160 ppm was used as an external reference. A phase incremented even-order selective pulse sequence [10] was used for MQ NMR experiments.

### Results

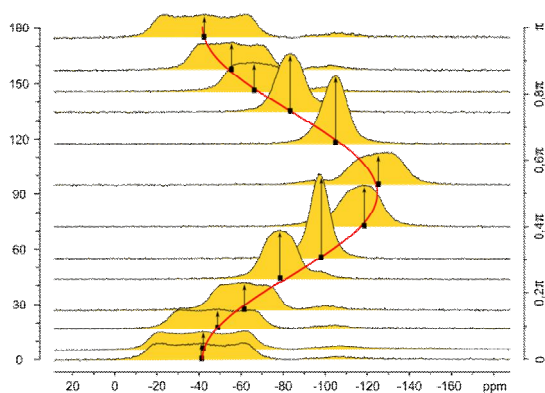


**Figure 1.** The changes of the  $^{19}\text{F}$  NMR spectra of FAp due to the rotation of the crystal c-axis about an axis perpendicular to the external magnetic field.

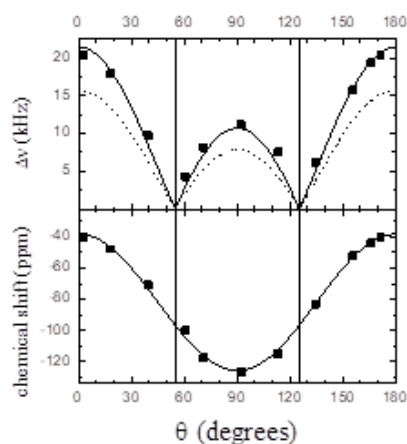


**Figure 2.** The dependence of the linewidth (top) and chemical shift (bottom) on the angle  $\theta$  for the single-crystal FAp.

The one-dimensional linear structure of FAp has been recognized since early NMR experiments [11, 12]. FAp is hexagonal crystal with space group  $P6_3/m$  and lattice parameters  $a = 9.367(1)$  Å and  $c$  (the hexagonal axis) =  $6.884(1)$  Å with one formula unit of  $\text{Ca}_{10}(\text{PO}_4)_6\text{F}_2$  per unit cell. The structure contains parallel chains of F ions along the  $c$ -axis of the crystal. The distance between neighboring chains is about three times larger than the distance between the nearest ions in a chain. Such an arrangement of the  $^{19}\text{F}$  spins results in the 40 times larger dipolar coupling between the nearest spins in the chain than the largest interaction with the spins of the neighboring chains (when the  $c$ -axis is aligned along the field direction). The  $^{19}\text{F}$  NMR absorption line of the FAp is known to be strongly anisotropic [13]. For the case of an axially symmetric chemical shift tensor one expect the following dependence on angle  $\theta$

$$\delta = \delta_{\perp} \sin^2 \theta + \delta_{\parallel} \cos^2 \theta = \delta_{\perp} + \Delta\delta \cos^2 \theta \quad (1)$$

where  $\delta$  is an effective chemical shift,  $\delta_{\perp} = \delta_{11} = \delta_{22}$  and  $\delta_{\parallel} = \delta_{33}$  are components of the tensor, and  $\Delta\delta$  is the chemical shift anisotropy. The  $^{19}\text{F}$  chemical shift of the fluoride anion is very sensitive to the cations to which it is bound. The orientation of the Ca triangles surrounding  $\text{F}^-$  ions with respect to external magnetic field strongly affects the  $^{19}\text{F}$  chemical shift. The parallel orientation of the  $^{19}\text{F}$  spin chains results in the most deshielded position of the line while the perpendicular orientation shows the biggest upfield shift (fig. 1.). The chemical shift anisotropy parameters were determined using eq. 2 (solid lines in fig. 1 and lower part of fig. 2). The obtained parameters  $\delta_{\text{iso}} = -97 \pm 1$  ppm and  $\Delta\delta = 87 \pm 1.5$  ppm are in agreement with the data reported for mineral FAp's in literature [13].

The linewidth of the  $^{19}\text{F}$  resonance also undergo strong changes during rotation. The dipolar coupling constant between spins  $i$  and  $j$  can be written as

$$D_{ij} = \frac{\gamma^2 \hbar}{2r_{ij}^3} (1 - 3 \cos^2 \theta) = b_{ij} (1 - 3 \cos^2 \theta) \quad (2)$$

where  $\gamma$  is the gyromagnetic ratio and  $r$  is the distance between spins. The experimentally observed variation of the linewidth in the FAp crystal follows the dependence

$$\Delta\nu \sim |D_{ij}| \sim A|1-3\cos^2\theta| \quad (3)$$

where  $A$  is the constant and  $\theta$  is the angle between chain and the external magnetic field. The approximation of the experimental data with eq. 3 is shown in fig. 2 with the solid line. This result indicates the dominating influence of the intrachain dipolar interactions on the lineshape.

When the orientation of the chains is parallel to the orientation of external magnetic field the linewidth is maximal and the resonance is symmetrically split up into three lines. The lineshape could be roughly interpreted as the splitting of the resonance due to the two nearest neighboring spins. The splitting due to a single nearby spin amounts to  $6b$ . This value is equal to the highest possible splitting for the dipolar pair. Taking into account the identical interaction with another neighboring spin we obtain the triplet with the spacing of the outer pair of lines of  $12b$  and the relative intensities of the components 1:2:1. More accurate calculations for the infinite evenly spaced spins arranged in a linear chain which take into account all nearest and the next nearest neighbor interactions lead to the complex multiplet pattern [11]. A detailed fine-structure of the splitting is masked by the other line-broadening interactions such as interactions between spin chains, interactions with far neighbors along a spin chain and heteronuclear interactions, but the distinctive triplet structure is conserved. The experimentally observed splitting of the outer lines of the triplet ( $15.7 \pm 0.4$  kHz) is in excellent agreement with value calculated from the structural data ( $12b = 15.72$  kHz). The inclination of the chain from the direction of the magnetic field results in a gradual disappearance of the fine structure (fig. 1). The dashed line in fig. 2 shows the dependence of the expected splitting ( $12b$ ).

Fig. 3 shows the results of the MQ NMR experiments with variable duration of the preparation period for different angles. The experimental data points are presented using the scaled preparation time:

$$\bar{\tau} = \tau(1-3\cos^2\theta) \quad (4)$$

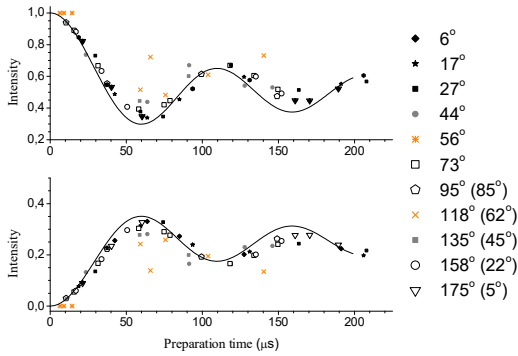


Fig. 3. Intensities of MQ NMR coherences: top - zero-quantum, bottom - double quantum

In such coordinates the matching of the experimental MQ coherence intensities with the theoretical predictions for a linear chain [14] (solid line in fig. 3) indicate that the spin dynamics is determined by the nearest neighbor dipolar coupling between spins in the same chain.

Obvious discrepancies are observed for the orientations close to the magic angles ( $56^\circ$  and  $118^\circ$ ) where the dipolar coupling between spins in chain is small and limits of validity of the theory are violated. The most of the data point coincide with the theoretical predictions. Small deviations are observed for the angles  $44^\circ$  and  $135^\circ$  which are still close to the magic angle. These could be ascribed to the larger influence of the angle setting error hence the changes of the dipolar constant in this range is the biggest. Orientation of the chain close to the perpendicular to the external magnetic field does not show significant deviations of MQ intensities despite the fact that the intrachain dipolar coupling is reduced twice while the interchain coupling is maximal.

### Conclusions

We experimentally investigated the chemical shift anisotropy, line shape and dynamics of the MQ NMR coherences for different sample orientations relative to the external magnetic field on quasi-one-dimensional system of  $^{19}\text{F}$  spins in a single crystal of FAp. The results show that the dynamics is governed predominantly by the dipole-dipole interactions of the spins belonging to the same chain regardless of the orientation excepting the small vicinity of the magic angle. Specifically MQ NMR experiments show that the interactions between nearest neighbors in the chain are most important in multi-spin dynamics.

### Acknowledgements

This work is supported by the Russian Foundation for Basic Research project no 16-03-00056.

### References

- [1] Nielsen, M.A. and I.L. Chuang, Quantum Computation and Quantum Information: 10th Anniversary Edition. 2011: Cambridge University Press.
- [2] Goldman, J.R., T.D. Ladd, F. Yamaguchi, and Y. Yamamoto, Appl Phys A, 2000. 71(1): p. 11-17.
- [3] Itoh, K.M., Solid State Communications, 2005. 133(11): p. 747-752.
- [4] Baum, J. et al., J Chem Phys, 1985. 83(5): p. 2015 -2025.
- [5] Kaur, G., A. Ajoy, and P. Cappellaro, New Journal of Physics, 2013. 15(9): p. 093035.
- [6] Krojanski, H.G. and D. Suter, Physical Review A, 2006. 74(6): p. 062319.
- [7] Bochkin, G.A., E.B. Fel'dman, S.G. Vasil'ev, and V.I. Volkov, Chem Phys Lett, 2017. 680: p. 56-60.
- [8] Bochkin, G.A., E.B. Fel'dman, S.G. Vasil'ev, and V.I. Volkov, Appl Magn Reson, 2018. 49(1): p. 25-34.
- [9] Bochkin, G. A., E.B. Fel'dman and S.G. Vasil'ev, Z Phys Chem, 2017. p. 513.
- [10] Shykind, D.N., J. Baum, S.B. Liu, A. Pines, and A.N. Garroway, J Magn Reson (1969), 1988. 76(1): p. 149-154.
- [11] Engelsberg, M., I.J. Lowe, and J.L. Carolan, Phys Rev B, 1973. 7(3): p. 924-929.
- [12] Van der Lugt, W. and W.J. Caspers, Physica, 1964. 30(8): p. 1658-1666.
- [13] Carolan, J.L., Chem Phys Lett, 1971. 12(2): p. 389-391.
- [14] Fel'dman, E.B. and S. Lacelle, Chemical Physics Letters, 1996. 253(1): p. 27-31.

## Elastic interactions of spherical particles in anisotropic cubic media

K.V. Vasin<sup>1</sup>, M.V. Eremin<sup>1</sup>

<sup>1</sup>Kazan Federal University, 420008, Kremlevskaya 18, Kazan, Russia

e-mail: [KVVasin@stud.kpfu.ru](mailto:KVVasin@stud.kpfu.ru)

The method to solve equation of elasticity for cubic media developed by I. M. Lifshitz and L. N. Rozentsveig [1] was used to obtain an expression for elastic interaction energy of two particles with spherical symmetry including impact of small anisotropy of elastic cubic field (up to quadratic terms). The works [2], [3], [4] proved applicability of classical elastic theory to describe interaction between impurity centers via acoustic (long wavelength) phonon field.

The problem of elastic interaction in cubic media is of a very general interest. A long story begins with significant contributions were made in such monographs as Landau L.D., Lifshitz E.M. Course of Theoretical Physics [5], Stoneham [6], Eshelby [7] and continues in recent works. It can be applied naturally to pair interactions of different sort of particles like point defects [6] or impurity centers [4].

Several solutions of this problem have been proposed on the assumption that the medium is isotropic, however, the impact of anisotropy can be very important, for instance in a case of two spherical particles. Elastic interaction for the latter one does not occur in neglect of anisotropic media. The anisotropy parameter is  $d = c_{11} - c_{12} - 2c_{44}$ , where  $c_{ij}$  is elastic stiffness constants. The latest solutions proposed by [8], [9] assume  $d$  as a small quantity, but obtained expressions could not be reduced to each other's.

While the theory of interaction via phonon field had been developed the interest to classical theory raised. Two different approaches to study interaction between two impurity centers through lattice: considering of exchange by phonons and interaction via deformation field based on theory of elasticity provide exactly same results [2], [3], [4] in a case of a long wavelength of phonons and neglecting retardation. The classical elastic theory provides more compact analytical expressions.

The general expression of interaction via elastic field of two particles (placed on  $\mathbf{r}_i$  and  $\mathbf{r}_j$  respectively) is written as [4]

$$H_{ij} = \sigma_{\alpha\beta}^i \sigma_{\gamma\delta}^j \nabla_{\beta}^i \nabla_{\delta}^j G_{\alpha\gamma}(\mathbf{r}_i - \mathbf{r}_j), \quad (1)$$

where  $\sigma_{\alpha\beta}$  – operators describe character of interaction between particle and lattice;  $G_{\alpha\gamma}$  – Green's tensor which is the solution of general elastic equation [1].

We used the method had been proposed by Lifshitz and L. N. Rozentsveig [1] to obtain an expression of  $G_{\alpha\gamma}$  assuming small anisotropy, our results agree with [9]. We have calculated also the energy interaction in a case, when both particles have spherical symmetry i.e. when tensor  $\sigma_{ij} = \delta_{ij} \sigma_a$ .

Derived by us expression is written as

$$H_{ij}^{(1)} = \frac{15d \left( n_1^4 + n_2^4 + n_3^4 - \frac{3}{5} \right) \sigma^i \sigma^j}{8\pi(\alpha + 2b)^2 r^3} \quad \#(2)$$

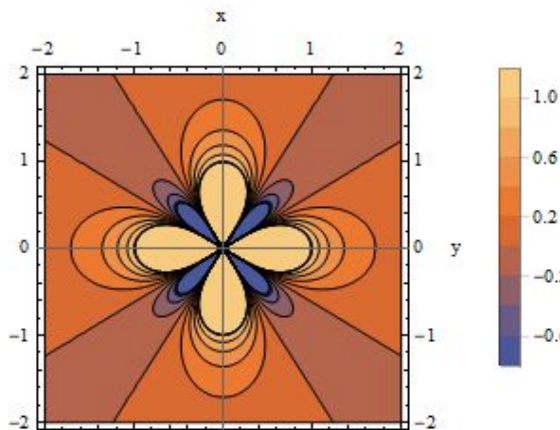


**Figure 1.** Areas of attraction and repulsion in XY plane for the case  $d > 0$ .

It has opposite sign in front with respect given in [7], but in agreement with obtained in recent work [9]. In addition we have derived correction to the energy interaction which are proportional to square with respect anisotropy parameter  $d^2$ .

Areas of attraction and repulsion in cubic media are shown in fig's below. Fig 1 shows results in linear approximation, then in fig 2 nonlinear corrections are taken into account for the case of  $d > 0$  and  $d < 0$ .

It shows the areas of attraction and repulsion in XY plane. One of particle is placed at the origin of coordinate system, while other can be in all possible positions. Yellow regions correspond to attraction

blue colors mean negative value of interaction energy – particles attract to each other corresponding to directions  $[1\ 1\ 0]$ ,  $[1\ \bar{1}\ 0]$ . These could be  $Mn^{2+}$  ions in  $CaF_2$  for instance.

However, the sign of  $d$  significantly changes the situation when nonlinear correction considered. Fig 2, 3 show two different cases: if  $d$  is positive quadratic term will split and reduce attraction region, otherwise it will conversely amplify the latter without splitting.

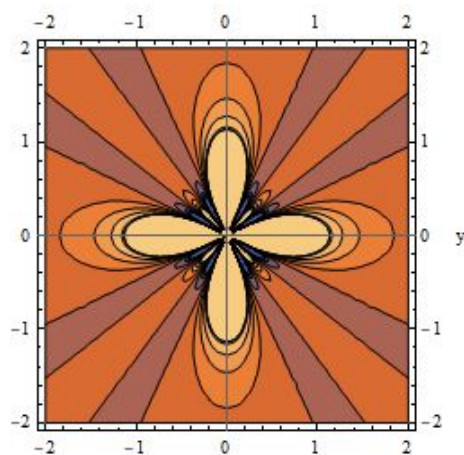


**Figure 2.** Areas of attraction and repulsion in XY plane for the case for  $d > 0$  with quadratic term.

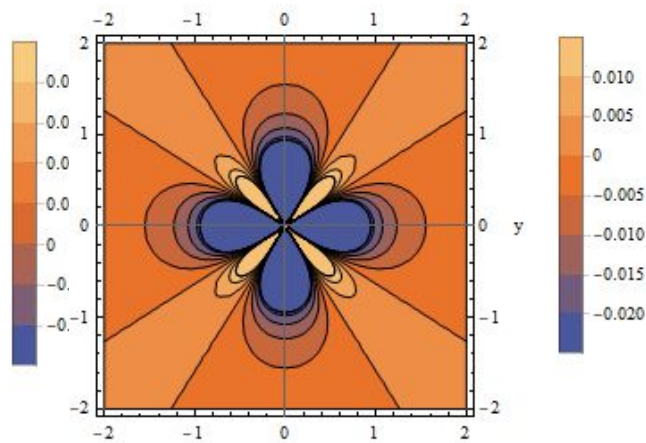


**Figure 3.** Areas of attraction and repulsion in XY plane for the case for  $d < 0$  with quadratic term.

## PROCEEDINGS

### References

- [1] Lifshitz and L. N. Rozentsveig, JETP, Vol. 9, 183 (1947).
- [2] Aminov L.K.. Kochelaev B.I., Soviet Physics JETP, Vol. 5, 15 (1962).
- [3] Orbach R.. Tachiki M., Phys. Rev, Vol. 158, 2 (1967).
- [4] Eremin M.V.. Zavidonov A.Y.. Kochelaev B.I., Zh. Eksp. Teor. Fiz.,Vol. 90 (1986).
- [5] Landau L.D., Lifshitz E.M., Course of Theoretical Physics.
- [6] Stoneham A.M., Theory of defects in solids, Oxford: Clarendon Press. (1975)
- [7] J.D. Eshelby, The Continuum Theory of Lattice Defects (1956).
- [8] Dederichs P.H.. G. L., Phys. Rev., Vol. 188, 1177 (1969).
- [9] Ostapchuk P.N., Solid State Phys., Vol. 54, 92 (2012).
- [10] K.I. Kugel D.I.Khomski., UFN, Vol. 136, 621 (1982).

**<sup>1</sup>H NMR spectroscopy investigation of thermally expanded graphite sorption capacity**

A.A. Voitash, Yu.V. Berestneva, E.V. Raksha, A.B. Eresko

L.M. Litvinenko Institute of Physical Organic and Coal Chemistry, 283114,  
70 R. Luxemburg Street, Donetsk, Ukraine

e-mail: anna.voytash@gmail.com

**Introduction**

The existing methods of sorption purification of industrial wastewater do not reach a satisfactory level of water quality at minimal cost. Therefore, the actual task is to improve such processes. Search and investigation of sorbents that based on available materials with low cost is of considerable interest. Thermally expanded graphite (TEG) can be used as such material [1].

In this paper, TEG was obtained by the thermal shock mode of heating of graphite nitrate cointercalation compound. The sorption properties of TEG in relation to dissolved in water organic pollutants were investigated. Concentrations of solvents were analyzed by <sup>1</sup>H NMR spectroscopy method.

**Experimental part**

In the study as a sorbent was used the thermally expanded graphite. As a starting material for TEG was used graphite nitrate cointercalation compound (GNCC). GNCC was obtained by treatment of the sample of natural flake graphite GT-1 (Zavaliye Graphite Works, Kirovograd region, Ukraine) with nitric acid with a density of 1.502 g/cm<sup>3</sup> (98%) for 10 min at 25°C. Then graphite nitrate was modified with two co-intercalants in equal amounts – ethylformate and acetic acid. The mixture was stirred again for 10 min. The consumptions of nitric acid and the co-intercalants were 0.6 and 6 cm<sup>3</sup> per 1 g of graphite, respectively. Further product was separated by filtration and dried at 25°C until the sample mass became constant.

TEG was obtained by the thermal shock mode of heating. A stainless cuvette of 150 cm<sup>3</sup> was placed into a muffle furnace preheated up to 900 °C. About 0.2 g of the GNCC was inserted into the heated cuvette and has been kept in the furnace for 120 s. Then the cuvette with TEG was removed from the furnace.

The TEG was used as a sorbent for investigation of water purification from organic pollutants (acetone, acetonitrile, 1,4-dioxane). The studied pollutants solutions of various concentrations were prepared for the adsorption process investigation. About 0.05 g of TEG was added to 100 cm<sup>3</sup> of each solution, the mixture was stirred and conditioned for 24 hours. After, the sorbent saturated with pollutant was filtered and the pollutants concentration in the filtrate was established by <sup>1</sup>H NMR spectroscopy method at 25 °C.

The <sup>1</sup>H NMR spectra of pollutants solutions were recorded on a Bruker Avance II 400 spectrometer (400 MHz), external standard – acetone-d<sub>6</sub>. The change of protons chemical shift of the investigated pollutant was used ( $\Delta\delta$ , ppm) for the experimental data processing.

$$\Delta\delta = \delta_0 - \delta_i, \quad (1)$$

where  $\delta_0$  – proton chemical shift of the original pollutant, ppm;

$\delta_i$  – proton chemical shift of the pollutant in solution, ppm.

Acetone,  $(\text{CH}_3)_2\text{CO}$ .  $^1\text{H NMR}$  (400 MHz,  $(\text{CD}_3)_2\text{CO}$ ):  $\delta = 2,97$  ppm (s, 6 H,  $(\text{CH}_3)_2$ ).

Acetonitrile,  $\text{CH}_3\text{CN}$ .  $^1\text{H NMR}$  (400 MHz,  $(\text{CD}_3)_2\text{CO}$ ):  $\delta = 2,53$  ppm, (s, 3 H,  $\text{CH}_3$ -).

1,4-dioxane,  $\text{O}(\text{CH}_2\text{CH}_2)_2\text{O}$ . (400 MHz,  $(\text{CD}_3)_2\text{CO}$ ):  $\delta = 3,79$  ppm (s, 3 H,  $\text{CH}_3$ -).

The sorption capacity of the TEG was determined from the relation (2):

$$S = \frac{C_0 - C}{m} \cdot V, \quad (2)$$

where S – sorption capacity of the TEG, g/g of the sorbent;

$C_0$  – initial concentration of the pollutant, mol/dm<sup>3</sup>;

C – equilibrium concentration of the pollutant, mol/dm<sup>3</sup>;

m – weight of the TEG, g;

V – volume of the solution, dm<sup>3</sup>.

### Results and Discussions

The obtained TEG is a black material with granules of vermicular porous structure. Bulk density of the TEG is 1.5-2.0 g/dm<sup>3</sup> and thermal expansion coefficient is  $K_V = 380$  cm<sup>3</sup>/g. The detailed description of the thermal expansion coefficient determination of the corresponding GNCC can be found in [2].

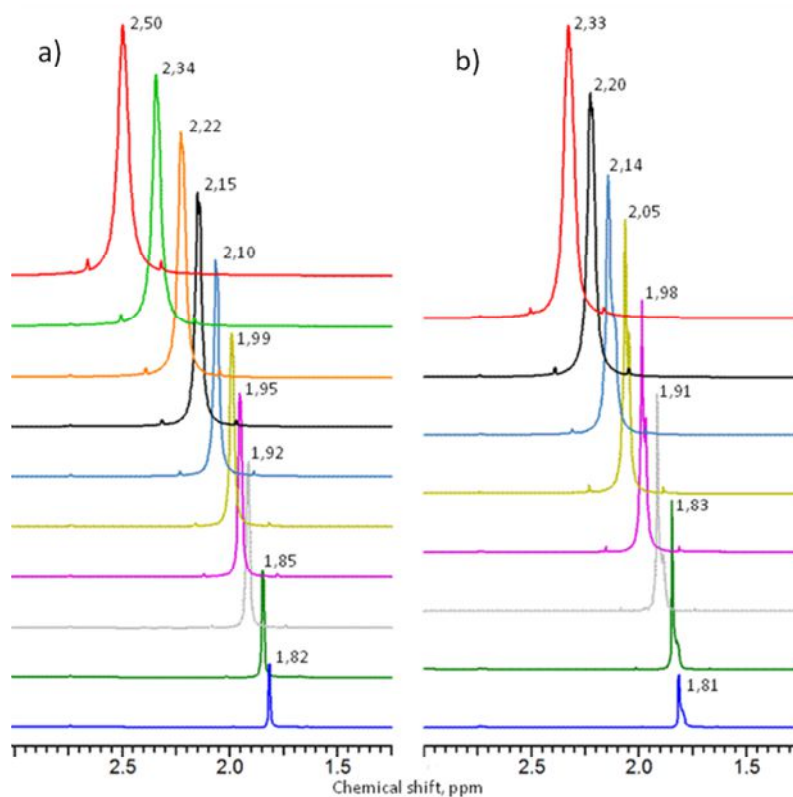


**Figure 1.**  $^1\text{H NMR}$  spectra fragments of acetonitrile aqueous solutions before (a) and after (b) adsorption process

Organic pollutants – acetone, acetonitrile, 1,4-dioxane – were used for the sorption capacity investigation. Initial and equilibrium concentrations were determined by  $^1\text{H}$  NMR spectroscopy method. Fig.1 illustrates the fragments of  $^1\text{H}$  NMR spectra of acetonitrile aqueous solutions before (a) and after (b) its sorption by TEG.

Decrease in acetonitrile concentration in the solutions leads to a monotonic upfield shift of the protons signal. The relationship between concentration of pollutants in solutions and change of protons chemical shift illustrated at fig.2.

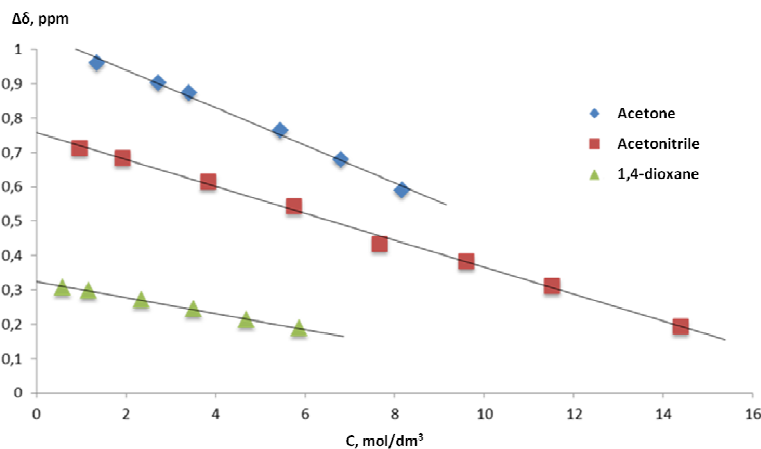


Figure 2. Protons chemical shift change vs pollutants concentration

The value of sorption capacity was determined from the relation (2). The adsorption isotherms, based on obtained values of the sorption capacity, are shown at fig. 3.

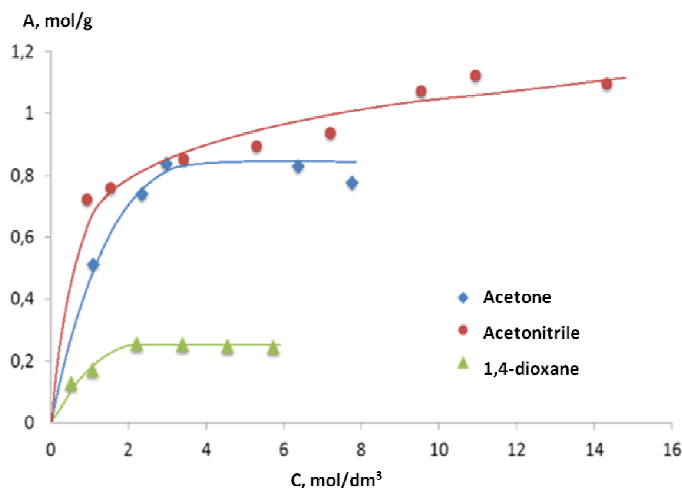


Figure 3. Competitive adsorption isotherms of acetone, acetonitrile and 1,4-dioxane on the thermally expanded graphite at 25 °C

The graphs (fig.3) are Type-1 isotherms that describe monolayer adsorption process. Adsorption isotherms were explained using Langmuir and Freundlich models (table 1). The values of Gibbs free energy were also calculated. The strong correlation ( $0,9 < r < 1$ ) between concentration and adsorption capacity shows that adsorption process can be described using both Langmuir and Freundlich models. The Gibbs free energy is negative, therefore the adsorption process is spontaneous. The values of maximum sorption volume were determined by the Langmuir model (table 2).

**Table 1.** Langmuir and Freundlich equations constants and the values of Gibbs free energy

Pollutant	Equations constants						$\Delta G$ , kJ/mol
	Freundlich equation			Langmuir equation			
	$\alpha$ , mol/g	1/n	r	$A_m$ , mol/g	K	r	
Acetone	0,49	0,49	0,99	0,97	1,08	0,93	-0,20
Acetonitrile	0,71	0,17	0,96	1,06	2,03	0,90	-1,75
1,4-dioxane	0,17	0,39	0,97	0,29	1,49	0,98	-0,99

**Table 2.** Maximum sorption volume of the TEG

Pollutant	Maximum sorption volume of the TEG, g/g
Acetone	56,35
Acetonitrile	43,51
1,4-dioxane	25,55

The sorption volume of the thermally expanded graphite decreases in the order of acetone > acetonitrile > 1,4-dioxane.

### Conclusions

The thermally expanded graphite was prepared from graphite nitrate sequentially cointercalated with ethylformate and acetic acid by the thermal shock mode of heating. The adsorption capacity of the TEG was investigated by  $^1\text{H}$  NMR spectroscopy method. The obtained sorbent demonstrates good sorption capacity in relation to dissolved in water organic pollutants. It was shown, that  $^1\text{H}$  NMR spectroscopy method can be used to obtain pollutants concentrations values in sorption capacity investigations.

### References

- [1] A.A. Voitash. Obtaining of the sorbent based on thermally expanded graphite / A.A. Voitash, Yu.V. Berestneva // Proceedings of the Conference “Problems of social-economy geography and management of environment”, Rostov-on-Don, 2017, P. 134-137.
- [2] E.V. Raksha. Triple graphite nitrate cointercalation compounds / E.V. Raksha, Yu.V. Berestneva, V.Yu. Vishnevsky, A.A. Maydanik, G.K. Volkova, V.V. Burhovetskiy, A.N. Vdovichenko, M.V. Savoskin // Vestnik Lugansk Vladimir Dahl national university, № 5(11) 2018 – P. 191-197.

**Synthesis and NMR cryoporometry of LaF<sub>3</sub> nanosized samples**

E.M. Alakshin<sup>1</sup>, A.V. Bogaychuk<sup>1</sup>, E.I. Kondratyeva<sup>1</sup>, A.V. Klochkov<sup>1</sup>, V.V. Kuzmin<sup>1</sup>,  
D.S. Nuzhina<sup>1</sup>, P.A. Zlishcheva<sup>1</sup>, M.S. Tagirov<sup>1,2</sup>

<sup>1</sup>Kazan Federal University, 420008, Kazan, Russia.

<sup>2</sup>Institute of Applied Research, TAS, 420111, Kazan, Russia.

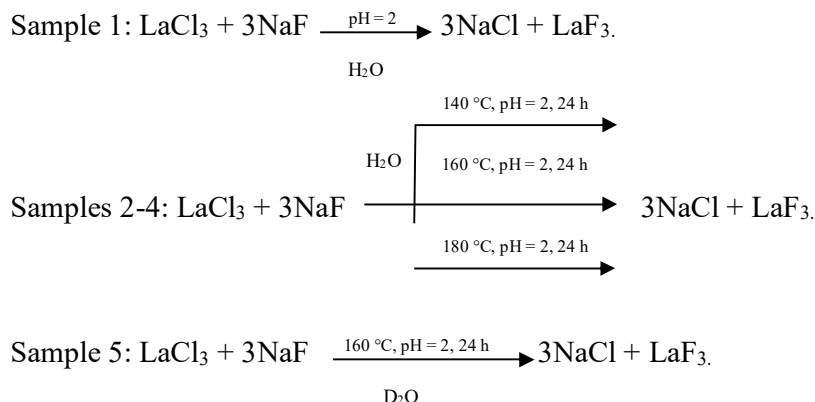
e-mail: pzlishcheva@mail.ru

**Introduction**

Nuclear magnetic resonance cryoporometry can be applied to the measurement of the pore sizes and the construction of the pore distribution from 1 to 100 nm. It is well known that the physical properties of a liquid confined in small pores can strongly differ from the properties of the bulk liquid [1]. A liquid that fills the free space of a porous medium always has a relatively large number of surface atoms. One of the relevant consequences is the decrease in the melting temperature. This effect is the basis of the cryoporometry method for studying the structural parameters of porous media, which uses the relation between the melting temperature of the liquid introduced into the pores and the pore size. It is convenient to determine the fractions of the solid and liquid phases of this substance from pulsed nuclear magnetic resonance data, since the solid phase has the shorter spin–spin relaxation time T<sub>2</sub> than the liquid phase [2].

**Materials and methods**

The LaF<sub>3</sub> nanoparticles samples #1-5 were synthesized using following technology:



The synthesized samples #2-4 contain clusters of water inside. Sample 5 also contains clusters of heavy water inside. Size of samples #1-5 was determined by transmission electron microscopy (TEM).

The average diameters of samples #1-5 respectively are d<sub>1</sub> = 31 nm, d<sub>2</sub> = 37 nm, d<sub>3</sub> = 46 nm, d<sub>4</sub> = 35 nm, d<sub>5</sub> = 40 nm. It follows from the experiment that the average diameter of nanoparticles LaF<sub>3</sub> increases with increasing temperature of hydrothermal treatment.

Pores size (for sample 3) was estimated by NMR cryoporometry. The characteristic size is 6-15 Å.

**References**

- [1] J. Beau and W. Webber, Prog. Nucl. Magn. Reson. Spectrosc. 56(78) (2010).
- [2] Alakshin E. M. et. al. JETP Letters. 96(3). 194 (2012).

## Stand for the analysis of the amplitude-time characteristics of the nuclear precession signal

V.A. Ushakov, A.V. Sergeev, E.D. Narkhov, V.A. Sapunov

Ural Federal University, 620002, Mira St. 21, Yekaterinburg, Russia

e-mail: ushakov.fti@gmail.ru

Larmor precession is the precession of the magnetic moment of an object about an external magnetic field has laid the ground for measuring magnetic field. POS-1 sensor made by QM Laboratory allows to measure magnetic field's module with high accuracy, firmly connected by gyromagnetic proton's ratio with frequency of free precession of nuclear magnetization's total vector [1–2]. Measuring this frequency by a special algorithm [3] magnetometer provides the data about magnetic field to a user, however most of amplitude and time characteristics in the measuring mode stay hidden. The report is about software & hardware solution (stand), adapted for POS-1, and developed for detailed research such characteristics.

Structure of measuring stand is presented on the Fig.1. Hardware part includes ADC E20-10 produced by L-Card (up to 10 MHz), computer и DLPOS (optionally). Software part consists of a LabView's program for analysis of digitized signal and a program for controlling of POS-1 sensor (in case of absence of control unit DLPOS) Depending on the task demands the program will allow to set required frequency of signal's digitization.

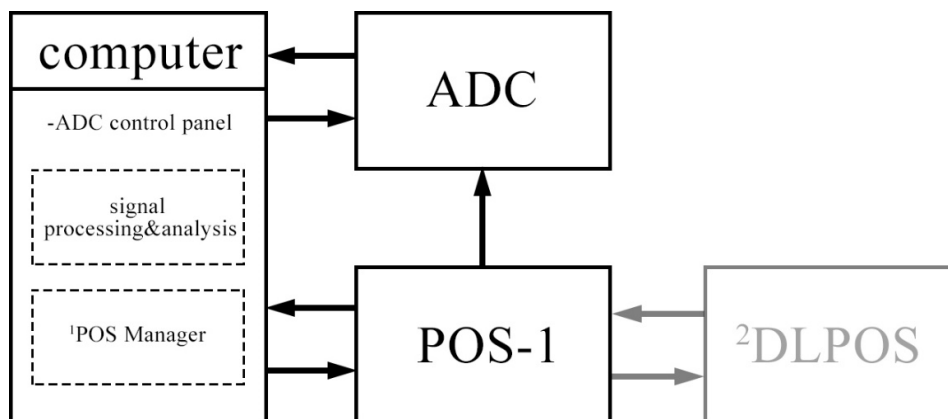
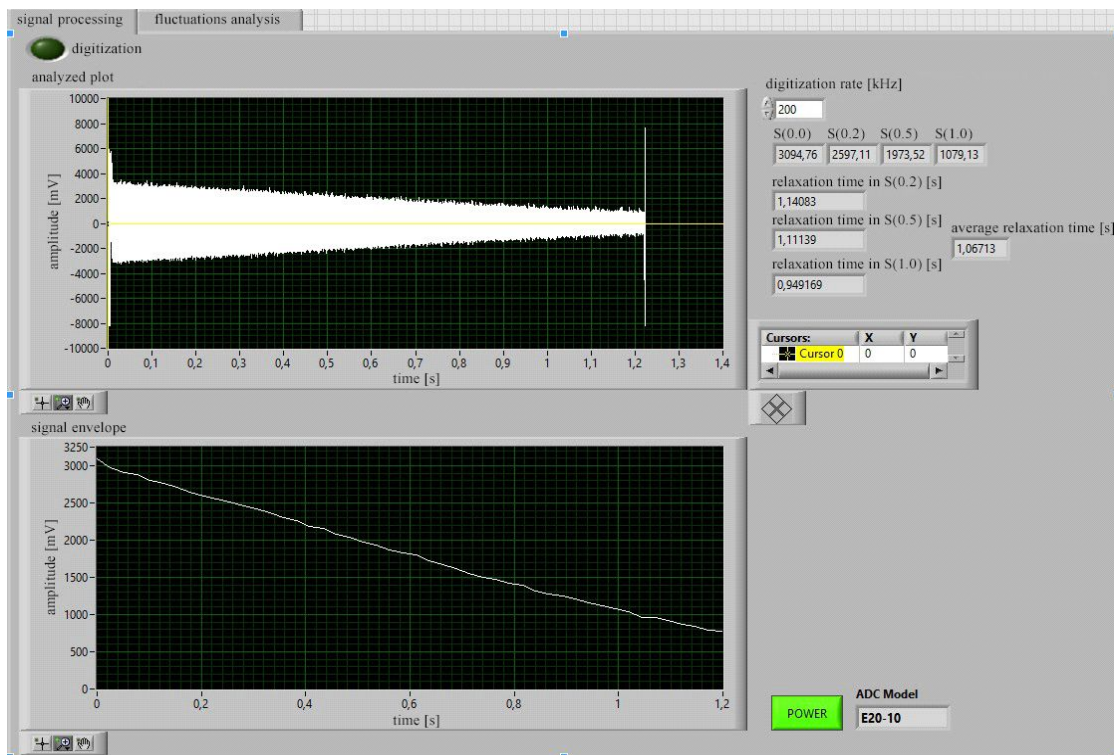


Figure 1. Structural stand's scheme.

Program of analysis will perform following tasks:

- selection of the free precession's signal;
- building curve for a signal (using Hilbert transformation) for further relaxation time evaluation;
- calculation relaxation time through exponential regression;
- collection and display of statistics of signal's transition through zero, with following evaluation of amount of precession periods' standard deviation.

Program's interface (fig.2 and fig.3) shows signal's parameters received in homogeneous field.



**Figure 2.** Panel showing the signal and its main characteristics.

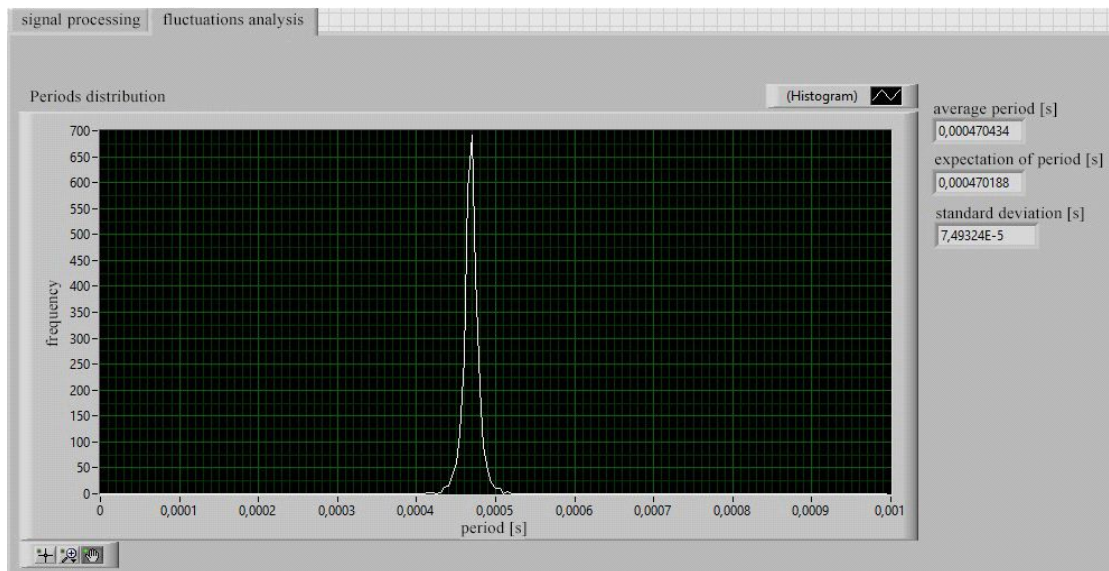


**Figure 3.** Panel of statistics' analysis of signal's transitions through zero level.

Developed stand has many functions:

- help in setting the sensor at the production stage, namely the determination of the initial amplitude of the signal, which should be optimized when tuning the high-frequency generator of the electron pumping of the magnetometer;

- the study of the characteristics of the working substance of the primary converter, namely the determination of the proton relaxation time, which should be in the range 0.3-1.5 seconds, depending on the type of instrument. By the relaxation time and the amplitude of the

## PROCEEDINGS

precession signal, the state of the sensors received for repair after a long period of operation is determined;

- study of the characteristics of the signal of free nuclear precession under conditions of a high-gradient magnetic field in order to determine the gradient-stability parameter, that is, the ability of the magnetometer to operate in the presence of strongly magnetic objects [4];

- As a following - measuring of degree of magnetic field's homogeneity at a point (narrowness of the stripe of the periods allocation tells about homogeneity of the measured field).

It is assumed that the developed stand will be useful for magnetic observatories using the POS-1 magnetometer everywhere, in particular to monitor the presence of impulse noise due to temperature stabilization systems.

In the future, it is planned to develop the presented stand to the level of the spectrometer of nuclei dynamic polarization for studying solutions of stable radicals, which are working substances of Overhauser magnetometers. The stand will be equipped with a special sensor with replaceable ampoules and a control unit for the low-frequency and high-frequency polarization fields.

### References

- [1] Abragam, Nuclear Magnetism, Moscow, 1963, p.24.
- [2] V.A. Sapunov, E.D. Narkhov, A.L. Fedorov, A.V. Sergeev, A.Y. Denisov, Ground Overhauser DNP geophysical devices, 15th international multidisciplinary scientific geoconference SGEM 2015: Science and Technologies in Geology, Exploration and Mining, conference proceedings, Volume I: Geology mineral processing Oil&Gas exploration, SGEM 2015 Conference Proceedings, pp. 215–222.
- [3] A.Yu. Denisov, V.A. Sapunov, O.V. Dikumar, Calculation of the error in the measurements of a digital-processor nuclear-precession magnetometer (1999), Geomagnetism and Aeronomy, 39(6), pp. 737–742.
- [4] Sergeev, A.V., Denisov, A.Y., Narkhov, E.D., Sapunov, V.A. Solution of magnetometry problems related to monitoring remote pipeline systems (2016) AIP Conference Proceedings, 1767, art. no. 020018.

## Towards an alpha-casein translational mobility by NMR

D.L. Melnikova<sup>1</sup>, I.V. Nesmelova<sup>2</sup>, V.D. Skirda<sup>1</sup>

<sup>1</sup> Department of Physics, Kazan Federal University, Kazan 420011, Russia.

<sup>2</sup>Department of Physics and Optical Sciences, and Center for Biomedical Engineering and Science, University of North Carolina, Charlotte, NC 28223, USA.

e-mail:melndaria@gmail.com

In the last decade it became known, that proteins have functional activity not only in globular condition, but in partly or whole disordered form [1]. The intrinsically disordered proteins functional role could be bound to the need of molecular plasticity for more effective identification by the partner-molecules [2, 3].

The degree of compactness of the polypeptide chain depends on the amino acid residue composition of a given protein and on environmental conditions, including the concentration of the protein itself and/or the crowders. Hence, there is a great interest to understand how the intrinsically disordered proteins (IDPs) behave in the wide range of concentrations, from dilute to highly concentrated solutions. In particular, understanding the translational diffusion of IDPs, which is the major mode of macromolecular transport in biological or chemical systems (e.g., the self-diffusion, hereafter denoted simply as diffusion), becomes important.

The purpose of current work was to study structural and dynamical features of translational mobility of the intrinsically disordered protein  $\alpha$  - casein in water solutions in a wide range of concentrations by NMR with pulsed field gradient (PFG).

This work was supported by the Faculty Research Grant from the University of North Carolina to I.V.N. NMR measurement were carried out on the equipment of the Federal Centre of Shared Facilities at Kazan Federal University.

### References

- [1] Uversky, V. N., Gillspie, J. R., Fink. A. L. Why are “natively unfolded” proteins unstructured under physiologic conditions? / V. N. Uversky, J. R. Gillspie, A. L. Fink // Proteins. – 2000. – V.41. – P. 415-427.
- [2] A. K. Dunker, D. J. Lawson. Intrinsically disordered protein. - J. Mol. Graphics and Modelling. 19, 26-59 (2001).
- [3] V. N. Uversky. A protein-chameleon: conformational plasticity of alpha-synuclein, a disordered protein involved in neurodegenerative disorders. - J. Biomol. Struct. Dyn. 21, 211—234 (2003).

## Scalar 3D-gradiometer and its advantages over a scalar magnetometer

A.V. Sergeev, E.D. Narkhov, A.L. Fedorov, A.A. Shirokov, V.A. Sapunov, A.Y. Denisov,  
V.V. Saveliev

Ural Federal University, 620002, Mira St. 21, Yekaterinburg, Russia

e-mail: sergeev.ftf@gmail.com

The achievements of the laboratory of quantum magnetometry in the field of signal processing algorithms, the development of a proton-containing liquid, made it possible to establish the production of quantum magnetometers of various designs [1–3]. These devices are widely used in various scientific and engineering fields:

- geological exploration works (magnetic prospecting);
- aero geophysical work (thanks to the sensor modification for reducing the size, with equal metrological characteristics);
- marine magnetometric studies (towed magnetometers - gradiometers, buoy-mounted monitoring stations, magnetometers for search as part of autonomous underwater vehicles);
- tracking geomagnetic activity in magnetic observatories (vector Overhauser magnetometer);
- support for inclined drilling (monitoring magnetometer) [4].

Modern methods of contactless magnetometric work and interpretation of the obtained data [5], required the design of a multichannel magnetometer, allowing to measure together with the magnetic field module, the components of its gradient. This configuration has been successfully tested [6], as a result of which it is possible to highlight the advantages of using data on components and the gradient module of the magnetic field module with respect to magnetic anomalies created by ferromagnetic objects:

- the transformation of the anomaly into an everywhere positive signal having maxima centered over sources of magnetic field anomalies;
- independence of the result from the configuration of the geomagnetic field;
- insusceptibility of the result to the distortion of anomalies caused by the constant magnetization of the sources;
- in comparison with long-wave geomagnetic ones, the amplitude of high-frequency anomalies characteristic for ferromagnetic objects is large. [7].

Fig. 1 shows an example of magnetic anomalies observed with a magnetic survey by a magnetometer and a gradiometer. In this example, anomalies from magnetic dipoles are considered, since they are one of the trivial sources that are often used to describe real magnetic anomalies. As can be seen from the figure, when using a scalar magnetometer due to the imposition of anomalies of two dipoles, it is difficult to determine their location without preliminary calculations. The gradient modulus does not have this drawback, which makes it useful for magnetometric studies. As a result, the use of a multichannel system greatly simplifies the shape of the anomalies (fig. 1), which allows some work to be done to find ferromagnetic objects in real time.

It is worth noting that, having a priori information about the nature of the source and the external magnetic field (geographic location of the survey), it is possible to apply simple calculations to the coordinates of the maxima of the gradient module to obtain the source coordinates [8].

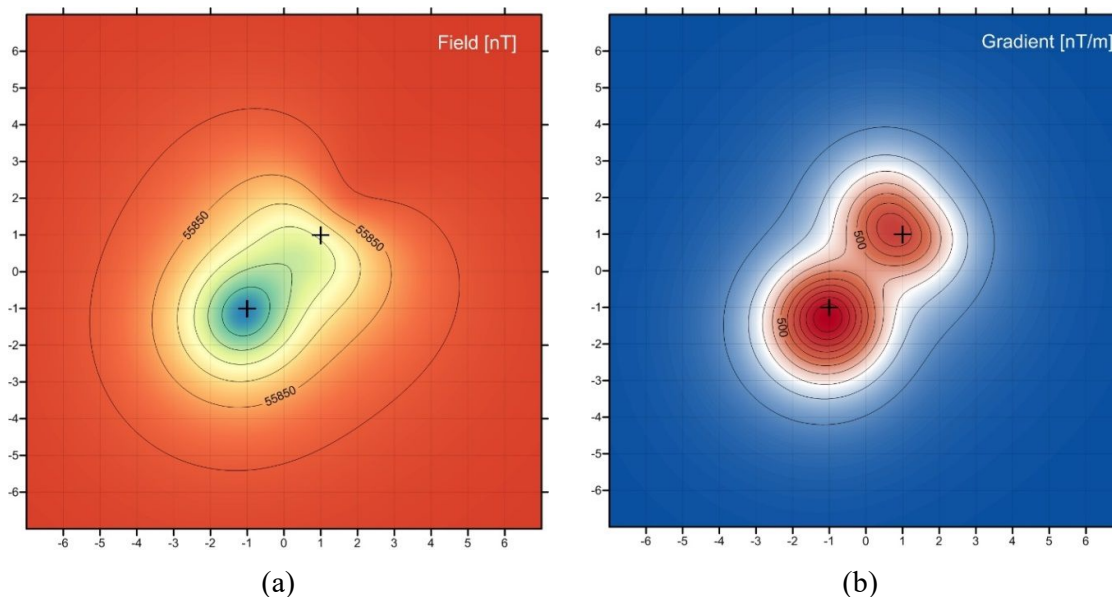


**Figure 1.** Magnetic anomaly from two buried, arbitrarily oriented dipoles, in the external magnetic field of the Ural latitudes. a – the field modulus, b – the modulus of gradient the field modulus (the width of the red region corresponds to the half-width of the anomaly, which is approximately equal to the depth of dipoles  $\sim 2$  m).

Thus, using the modulus of the field modulus gradient becomes even more efficient.

### References

- [1] Denisov A.Yu., Sapunov V.A., Dikumar O.V. Calculation of the error in the measurements of a digital-processor nuclear-precession magnetometer // *Geomagnetism and Aeronomy*. - 1999. - V. 39. - № 6. - pp. 737-742.
- [2] Sapunov V., Denisov A., Denisova O., Saveliev D. Proton and Overhauser magnetometers metrology // *Contributions to Geophysics and Geodesy*. - 2001. - V. 31. - №1. - pp. 119-124.
- [3] Denisov A.Y., Denisova O.V., Sapunov V.A., Khomutov S.Y. Measurement quality estimation of proton-precession magnetometers // *Earth, Planets and Space*. - 2006. - V.58. - №6. - pp. 707-710.
- [4] Mikhail Tchernychev, Ross Johnson, James Kulpa Using a transverse marine gradiometer (TVG) as submarine pipeline location tool // *Oceans - San Diego*. – 2013.
- [5] Sapunov V.A., Denisov A.Y., Saveliev D.V., Soloviev A.A., Khomutov S.Y., Borodin P.B., Narkhov E.D., Sergeev A.V., Shirokov A.N. New vector/scalar overhauser DNP magnetometers POS-4 for magnetic observatories and directional oil drilling support // *Magnetic Resonance in Solids*. - 2016. - V. 18. - № 2. - 16209.
- [6] Sergeev A.V., Narkhov E.D., Ivanenko A.N., Brusilovskiy Yu.V., Milyukov D.N., Denisov A.Yu., Sapunov V.A. High-precision mapping of submerged objects using the full-gradient overhauser magnetometer system // *AIP Conference Proceedings*. - 2017. - V. 1886. - 020076.
- [7] Doug Hrvoic and Matthew R. Pozza Mapping marine ferrous targets using real-time 3D analytic signal data // *The Leading Edge*. – 2006. - V.25. - №1. pp. 54-56.
- [8] Narkhov E.D., Shirokov A.A., Sergeev A.V., Fedorov A.L., Milovidov E.M., Denisov A.Yu., Saveliev D.V., Sapunov V.A. The perspective of full-gradient magnetometry system application in searching for magnetic objects // *AIP Conference Proceedings* 1886, 020103 (2017).

## ESR and electrophysical properties of oil fractions

A.T.Sorokina, M.R.Gafurov

Kazan Federal University, 420008, Kremlevskaya, 18, Kazan, Russia.

E-mail: alexandrasortim@gmail.com

Oil dispersed systems are promising organic material, since they contain substituted naphthenic aromatic, polyconjugated aromatic fragments and unpaired electrons present in organic electrically conductive structures. This allows us to consider them as a perspective object of nanotechnology.

The aim of the work is the research of the EPR spectra and electrophysical properties of high-boiling oil fractions of Kungur oil, that are used for the producing of industrial oils.

Kungur oil was used as objects of the research. This oil was divided into 20-degree oil fractions.

In consequence of the research the oil spectra and its fractions by using the EPR method, it was established:

1. In the initial oil and in fractions > 500, two types of paramagnetic centers of the vanadylporphyrin complexes (VPCs) and free radical (FR) were detected with the following parameters:

FR:  $g = 2.0059 \pm 0.001$ ,

VO<sup>2+</sup>:  $g_{\perp} = 1.987 \pm 0.002$ ,  $g_{\parallel} = 1.966 \pm 0.003$ ,  $A = 58.3 \pm 0.2$  G,  $A_{\parallel} = 165 \pm 2$  G.

2. In the fraction below 500 and up to 400°C only the free radical line is detected. In the lighter fractions below 400 degrees, the signal FR was not observed.
3. Relative intensity of FR signal as the temperature decreases.
4. The overwhelming majority of paramagnetic VPCs are concentrated in heavy oil fractions. Absolute concentrations of paramagnetic VPCs were determined.

FR: initial oil -  $3000 * 10^{13}$  spin / mg, fraction > 500 -  $402 * 10^{13}$  spin / mg

VO<sup>2+</sup>: initial oil -  $1760 * 10^{13}$  spin / mg, fraction > 500 -  $365 * 10^{13}$  spin / mg

5. In oil dispersed systems with a large number of unpaired electrons, the phenomena of spin-spin and spin-lattice relaxation are essential, which explain the features and shapes of the EPR signal. By the reduction the sublimation temperature of the fractions absorption line shape changes from the Lorentzian to the Gaussian.
6. The vanadylporphyrin complex influences on the width of the lines (the relaxation rate) of FR in the oil-dispersed systems, which may indicate the participation of the VPCs in the asphaltene aggregation processes.

In consequence of the research of electrophysical properties, it was established:

1. Electrical conductivity rises with increasing temperature, and the rate of conduction growth in heavy fractions is higher than in light ones.
2. The general trend towards the decline of electrical conductivity with increasing boiling point of the fraction. This is explained by the increasing of the density, and, as a consequence, the viscosity.
3. There is a noticeable deviation from this trend for a fraction with a boiling point of 440-460 °C. A similar deviation in the concentration of free hydrocarbon radicals is noticeable for the same fraction in other measurements within the framework of this

## PROCEEDINGS

paper, which allows us to relate the change in electrical conductivity not only with the change in viscosity, but also with the concentration of free hydrocarbon radicals.

On the basis of experimental data on the electrical conductivity, it can be concluded that the density and viscosity of the distillate structures exert a greater influence on the electrical conductivity than the concentration of free radicals. However, the increase of the temperature gradually increases the contribution of the concentration of radicals to the electrical conductivity of the distillate fractions.





# TABLE OF CONTENTS

## Table of contents

<b>Program</b> .....	3
<b>Lecture notes</b> .....	6
<b>U. Eichhoff</b> , The human brain: development and aging explored by MRI.....	6
<b>V.V. Klochkov</b> , Investigation of the spatial structure of different drugs, proteins & oligopeptides, and their complexes with models of cell membrane in solution by modern NMR spectroscopy.....	7
<b><u>B.I. Khairutdinov</u>, E.A. Ermakova</b> , NMR Spectroscopy to Study the Structure, Dynamics and Molecular Interactions of Biopolymers.....	8
<b><u>M. Gafurov</u>, B. Gabbasov, G. Mamin, I. Ignat'ev, Y. Chelyshev, S. Orlinskii, N. Petrakova, A. Fedotov, V. S. Komlev</b> , Electron paramagnetic resonance of atherosclerotic plaques and synthetic calcium phosphates to follow pathological calcification processes.....	9
<b><u>K.S. Usachev</u>, A.G. Bikmullin, A.A. Golubev, N.S. Garaeva, L.I. Nurullina, I.Sh. Khusainov, N. Trachtmann, Sh.Z. Validov, V.V. Klochkov, A.V. Aganov, B. Kieffer, M.M. Yusupov</b> , NMR spectroscopy applications in structural studies of Staphylococcus aureus ribosome hibernation mediated by intermolecular interactions of HPF.....	11
<b>F.S. Dzheparov</b> , Random walks in disordered lattice, CTRW, memory and dipole transport.....	14
<b>E.B. Fel'dman</b> , Applications of magnetic resonance methods for development of quantum technologies.....	15
<b>Sh.K. Latypov</b> , Modern high-resolution NMR methods for structural analysis: Interplay of experiment and DFT calculations of NMR parameters.....	16
<b>Yu. I. Talanov</b> , Magnetic resonance in topological insulators.....	17
<b>E.L. Vavilova</b> , Introduction to solid-state NMR studies of lithium ion dynamics in potential battery materials.....	19
<b>I. Yatsyk, T. P. Gavrilova, <u>R. M. Eremina</u>, V. V. Parfenov</b> , Investigations of hexagonal manganites by ESR methods.....	20
<b><u>E.M. Alakshin</u>, E.I. Kondratyeva, V.V. Kuzmin, K.R. Safiullin, A.A. Stanislavovas, A.V. Savinkov, A.V. Klochkov, M.S. Tagirov</b> , The study of ReF <sub>3</sub> Nanoparticles by NMR.....	27
<b>S.B. Orlinskii</b> , Investigation of nature of self organization of nanosystems by magnetic resonance.....	28
<b>B.Z. Rameev</b> , Applications of NMR & NQR techniques for detection of energetic and dangerous materials.....	29
<b>S. Vasiliev</b> , Dynamic nuclear polarization in silicon at ultra-low temperatures.....	35
<b>Yu. M. Bunkov</b> , Magnons Bose-Einstein Condensation and Spin Superfluidity.....	36
<b>V. V. Dmitriev</b> , NMR in new superfluid phases of <sup>3</sup> He.....	38
<b>Proceedings</b> .....	39

## TABLE OF CONTENTS

<b><u>A.V. Muratov, Yu.V. Berestneva, E.V. Raksha, A.B. Eresko</u></b> , Experimental vs GIAO calculated NMR spectra for [1,2]diazepino[4,5-b]indole derivatives.....	39
<b><u>G.A. Bochkin, F.B. Fel'dman, I.D. Lazarev, S.G. Vasil'ev, V.I. Volkov</u></b> , Decay of multiple quantum NMR coherences in quasi-one-dimensional chains in calcium fluorapatite.....	43
<b><u>G. Dolgorukov, V. Kuzmin, K. Safiullin, A. Stanislavovas, E. Alakshin, T. Safin, B. Yavkin, S. Orlinskii, A. Klochkov, M. Tagirov</u></b> , Atomic-scale probing of paramagnetic centers in nanodiamonds by $^3\text{He}$ NMR.....	46
<b><u>Yu.M. Bunkov, A.R. Farhutdinov, G.V. Mamin, S.B. Orlinskii, T.R. Safin, P.M. Vetoshko, D.G. Zverev, M.S. Tagirov</u></b> , Conventional magnon BEC in YIG films.....	50
<b><u>A. Fedotov, M. Gafurov, I. Smirnov, B. Yavkin, G. Mamin, S. Orlinskii, V.S. Komlev</u></b> , Investigation of synthetic octacalciumphosphate content and structure with electron paramagnetic resonance.....	52
<b><u>A.Yu. Germov, Z.N. Volkova, A.P. Gerashenko, K.N. Mikhalev, S.V. Verkhovskii</u></b> , NMR study of electron-doped cubic manganites $\text{Sr}_{1-x}\text{La}_x\text{MnO}_3$ .....	55
<b><u>M. Goldberg, V. Smirnov, O. Antonova, A. Konovalov, D. Titov, V.S. Komlev, S. Barinov, A. Rodionov, M. Gafurov, S. Orlinskii</u></b> , Synthesis and sintering of the synthetic hydroxyapatite doped with aluminum.....	57
<b><u>S.K. Gotovko, L.E. Svistov</u></b> , Multiferroicity of $\text{CuCrO}_2$ tested by ESR.....	61
<b><u>D. Ivanov</u></b> , Resinous-asphaltene aggregates by NMR analysis.....	63
<b><u>G.A. Bochkin, E.B. Fel'dman, I.D. Lazarev, S.G. Vasil'ev</u></b> , Contributions of different parts of dipole-dipole interactions to relaxation of multiple quantum NMR coherences in a single crystal of calcium fluorapatite.....	64
<b><u>R. F. Likеров, I. V. Yatsyk, R.M. Eremina, Yu. D. Zavartsev, A. S. Kutovoi</u></b> , Investigation of $\text{YVO}_4$ monocrystals doped by $^{143}\text{Nd}^{3+}$ and $^{145}\text{Nd}^{3+}$ rare earth ions by EPR and crystal-field parameters calculations.....	68
<b><u>K.M. Makushin, G.V. Mamin, M.R. Gafurov, S.B. Orlinskii, I.N. Kurkin, E.I. Baibekov</u></b> , Analysis and interpretation of ENDOR spectra of $\text{LiYF}_4$ crystal activated with rare-earth ions.....	72
<b><u>E.M. Alakshin, A.V. Bogaychuk, V.V. Kuzmin, A.V. Klochkov, E.I. Kondrateva, I.K. Nekrasov, M.S. Tagirov</u></b> , High-field $T_2$ MRI contrast agent based on $\text{TbF}_3$ and $\text{DyF}_3$ nanoparticles.....	76
<b><u>R.A. Novikov, D.D. Borisov, Y.V. Tomilov</u></b> , Application of $^{71}\text{Ga}$ and $^{127}\text{I}$ NMR spectroscopy for the mechanistic studies of Ga(III)-mediated reactions of D–A cyclopropanes with pyrazolines.....	77
<b><u>D.S. Nuzhina, S. Abe, S.L. Korableva, K. Matsumoto, I.V. Romanova, K. Ubukata, M.S. Tagirov</u></b> , Experimental investigation of magnetostriction in $\text{LiRF}_4$ (R=Yb, Tm) in the strong magnetic fields.....	80
<b><u>E.A. Razina, A.S. Ovsyannikov, S. E. Solovieva, I. S. Antipin, A. I. Konovalov, G.V. Mamin, M.R. Gafurov, M.S. Tagirov, S.B. Orlinskii</u></b> , EPR of calixarenes doped by rare-earth metals ions.....	83

## TABLE OF CONTENTS

<b><u>I. Rodygina, V.N. Glazkov, T. Masuda</u></b> , Antiferromagnetic resonance in quasy-2D antiferromagnet Ba <sub>2</sub> MnGe <sub>2</sub> O <sub>7</sub> .....	87
<b><u>D.V. Shurtakova, G.V. Mamin, M.R. Gafurov, S.B. Orlinskii, E.S. Klimanshina, V.I. Putlyaev</u></b> , Spin-lattice relaxation of NO <sub>3</sub> <sup>2-</sup> complex in synthetic hydroxyapatite. Calculation of the relaxation rate using the phonon spectrum.....	90
<b><u>V. Kuzmin, K. Safiullin, A. Stanislavovas</u></b> , Self-diffusion of gaseous <sup>3</sup> He in oriented aerogels.....	94
<b><u>G.A.Bochkin, E.B.Fel'dman, I.D.Lazarev, A.A. Samoilenko, S.G.Vasil'ev</u></b> , The influence of the dipolar coupling strength on the spin dynamics of quasi-one-dimensional spin chains in fluorapatite.....	97
<b><u>K.V. Vasin, M.V. Eremin</u></b> , Elastic interactions of spherical particles in anisotropic cubic media.....	101
<b><u>A.A. Voitash, Yu.V. Berestneva, E.V. Raksha, A.B. Eresko</u></b> , <sup>1</sup> H NMR spectroscopy investigation of thermally expanded graphite sorption capacity.....	104
<b><u>E.M. Alakshin, A.V. Bogaychuk, E.I. Kondratyeva, A.V. Klochkov, V.V. Kuzmin, D.S. Nuzhina, P.A. Zlishcheva, M.S. Tagirov</u></b> , Synthesis and NMR cryoporometry of LaF <sub>3</sub> nanosized samples.....	108
<b><u>V.A. Ushakov, A.V. Sergeev, E.D. Narkhov, V.A. Sapunov</u></b> , Stand for the analysis of the amplitude-time characteristics of the nuclear precession signal.....	109
<b><u>D.L. Melnikova, I.V. Nesmelova, V.D. Skirda</u></b> , Towards an alpha-casein translational mobility by NMR.....	112
<b><u>A.V. Sergeev, E.D. Narkhov, A.L. Fedorov, A.A. Shirokov, V.A. Sapunov, A.Y. Denisov, V.V. Saveliev</u></b> , Scalar 3D-gradiometer and its advantages over a scalar magnetometer.....	113
<b><u>A.T. Sorokina, M.R. Gafurov</u></b> , ESR and electrophysical properties of oil fractions.....	115
<b>List of authors</b> .....	117
<b>Table of contents</b> .....	119

*Scientific edition*

**ACTUAL PROBLEMS OF MAGNETIC RESONANCE  
AND ITS APPLICATION**

**XX International Youth Scientific School**

**Program  
Lecture Notes  
Proceedings**

**Kazan  
24 – 29 September 2018**

Signed for printing 19.09.2018.  
Offset paper. Digital printing.  
Format 60x84 1/8. Гарнитура «Times New Roman».  
Conventional printing plates: 7,21  
Print run: 80 copies. Order: 208/9

Printing from camera-ready copy  
at Kazan University Press printing house

420008, Kazan, Professor Nuzhin str., 1/37  
Tel.: (843) 233-73-59, 233-73-28